# NOTICE

The quality of this microform is heavily dependent upon the quality of the original thesis submitted for microfilming. Every effort has been made to ensure the highest quality of reproduction possible.

If pages are missing, contact the university which granted the degree.

Some pages may have indistinct print especially if the original pages were typed with a poor typewriter ribbon or if the university sent us an inferior photocopy.

Reproduction in full or in part of this microform is governed by the Canadian Copyright Act, R.S.C. 1970, c. C-30, and subsequent amendments.

# AVIS

La qualité de cette microforme dépend grandement de la qualité de la thèse soumise au microfilmage. Nous avons tout fait pour assurer une qualité supérieure de reproduction.

S'il manque des pages, veuillez communiquer avec l'université qui a conféré le grade.

La qualité d'impression de certaines pages peut laisser à désirer, surtout si les pages originales ont été dactylographiées à l'aide d'un ruban usé ou si l'université nous a fait parvenir une photocopie de qualité inférieure.

La reproduction, même partielle, de cette microforme est soumise à la Loi canadienne sur le droit d'auteur, SRC 1970, c. C-30, et ses amendements subséquents.

Canada

University of Alberta

# The Application of Finite Element Models to the Analysis and System Identification of Flexible Rotors

by

## William F. Eckert

A thesis submitted to the Faculty of Graduate Studies and Research in partial fulfillment of the requirements for the degree of **Doctor of Philosophy**.

Department of Mechanical Engineering

Edmonton, Alberta

Spring 1992

Canadä

University of Alberta

Release Form

ame of Author: **William F. Eckert**

itle of Thesis: **The Application of Finite Element Models to the Analysis and System Identification of Flexible Rotors**

Degree: **Doctor of Philosophy**

Year this degree granted: **1992**

Permission is hereby granted to the **University of Alberta Library** to reproduce single copies of this thesis and to lend or sell such copies for private, scholarly, or scientific research purposes only.

The author reserves all other publication and other rights in association with the copyright in the thesis, and except as hereinbefore provided neither the thesis nor any substantial portion thereof may be printed or otherwise reproduced in any material form whatever without the author's prior written permission.
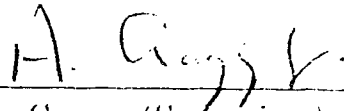
William F. Eckert
Apt. 406, 9717-111 Street
Edmonton, Alberta
Canada
T5K 2M6

Date : _____

University of Alberta

Faculty of Graduate Studies and Research

The undersigned certify that they have read, and recommend to the Faculty of Graduate Studies and Research for acceptance, a thesis entitled **The Application of Finite Element Models to the Analysis and System Identification of Flexible Rotors** submitted by **William F. Eckert, P. Eng.** in partial fulfillment of the requirements for the degree of **Doctorate of Philosophy**.
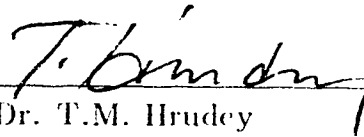
_____
Dr. A. Craggs (Supervisor)

_____
Dr. A.W. Lipsett

_____
Dr. A. Mioduchowski

_____
Dr. T.M. Hrudey

_____
Dr. B. Tabarrok

Date : 21 April 1992.

To Jan,

A special friend whose smile always brightens my day.

And whose encouragement and support helped motivate

me to finish this thesis!

# Abstract

At present, finite element models of turbomachine shafts use elements based on beam theory, which are limited in accuracy when modelling discontinuities in shaft sections such as abrupt changes in diameter. A new axisymmetric shaft element has been formulated based on three-dimensional elasticity principles. Three dimensional elements are better at representi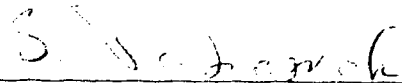ng these changes in shaft section, but with the added expense of complexity and matrix size. Comparisons of the modelling of rotating machine shafts with traditional beam-shaft and axisymmetric shaft elements are presented.

Also, assembling the finite element model using the normal stiffness approach may result in large global matrices requiring special solution techniques. A continuous matrix condensation technique has been presented, resulting in smaller matrices during and after the assembly process. Results comparing the forced response solution of the full global matrix system and the condensed matrix system are given.

Refinement of finite element models is done using methods that compare experimental spectral data or frequency response functions with calculated data. The methods presently available require testing of a shaft under a variety of support conditions or the measurement of accurate mode shapes. This thesis presents a new method that performs moderate adjustments to a finite element model based only on the comparison of selected calculated and measured natural frequencies.

# Acknowledgements

# Contents

## CHAPTER 4

## On the Application of Bearings      70

## CHAPTER 5

## Continuous Coordinate Condensation      86

## CHAPTER 6

## System Identification      121

**CHAPTER 7**

## Conclusions

**REFERENCES**

**APPENDIX A**

## Derivations

# List of Tables

# List of Figures

# Nomenclature

| | |
|---|---|
| $A_x$ | cross-sectional area |
| $C$ | diametral clearance |
| $E$ | modulus of elasticity |
| $F$ | force |
| $G$ | modulus of rigidity |
| $I$ | second moment of area |
| $I_p$ | polar moment of inertia |
| $K$ | shear correction coefficient |
| $\mathcal{L}$ | Lagrangian, $T - U$ |
| $M$ | bending moment |
| $N$ | shaft speed, rev. per second |
| $S$ | Sommerfeld number |
| $T$ | kinetic energy |
| $U$ | potential (strain) energy |
| $W_{ext}$ | external work done |
| $W, V$ | translational displacements |
| $X, Y, Z$ | inertial coordinate system |
| $[C]$ | damping matrix |
| $[D]$ | elasticity matrix or dynamic matrix |
| $[G]$ | gyroscopic matrix |
| $[I]$ | identity matrix |
| $[J]$ | Jacobian matrix |
| $[K]$ | stiffness matrix |
| $[M]$ | mass matrix |
| $[T]$ | transformation matrix |

| | |
|---|---|
| $\{B_o\}$ | bending deflection shape function |
| $\{C\}$ | shear angle deflection shape function |
| $\{D\}$ | bending angle deflection shape function |
| $\{N\}$ | serendipity functions |
| $\{X\}$ | mode shape |
| $a_j$ | element correction factors |
| $\ell$ | element length |
| $n$ | number of eigenvalues to correct |
| $p$ | number of element stiffnesses to correct |
| $q$ | distributed external load |
| $r, z, \theta$ | cylindrical coordinates system |
| $u, v, w$ | displacements |
| $w$ | total transverse deflection |
| $w_b$ | transverse deflection due to bending |
| $x, y, z$ | rotating coordinate system |

## Superscripts

| | |
|---|---|
| $[\ ]^T$ | matrix transpose |
| $[\ ]^{-1}$ | matrix inverse |
| $0$ | in-plane bending component |
| $1$ | out-of-plane bending component |

## Subscripts

| | |
|---|---|
| $\Im$ | imaginary components |
| $\Re$ | real components |
| $e$ | element nodal unknowns |
| $r, z, \theta$ | cylindrical coordinate components, or derivatives |

# Greek

| | |
|---|---|
| $\Gamma, B$ | angular displacements |
| $\Omega$ | shaft speed |
| $\alpha_i$ | polynomial coefficients |
| $\beta$ | shear coefficient, $EI/KGA_x$ |
| $\delta$ | small variation |
| $\epsilon$ | strain |
| $\phi$ | $12\beta/\ell^2$ |
| $\lambda^2$ | measured eigenvalue |
| $\mu$ | dynamic viscosity |
| $\nu$ | Poisson's ratio |
| $\theta$ | bending slope |
| $\sigma$ | stress |
| $\omega^2$ | calculated eigenvalue or forcing frequency squared |
| $\vec{\omega}$ | angular velocity |
| $\psi$ | shear angle |

# CHAPTER 1

# Introduction

*A Midsummer Night's Dream – Shakespeare [1]*

In the last twenty years, increased costs and greater demands on performance have forced a change in machine design. Modern machines are being built with lighter shafts and support systems, and as a result, it is becoming more common for turbomachines to be run at speeds near or above the first critical speed of the machine shaft. In fact, some machines operate above several of their lower critical speeds, requiring that the machine pass through those speeds on startup and rundown. For safe operation, the damped response of the machine at the critical must be known. As well, the advent of less expensive variable speed drive systems has increased the number of machines operating over a wide range of speeds, requiring that the critical speeds of the machine be well known to prevent sustained operation at those speeds. The need, therefore, for more accurate tools for predicting the critical speeds or natural frequencies of vibration and for analyzing the forced response of a turbomachine shaft has increased. Many machines are designed using long-standing engineering procedures, such as the transfer matrix method, which can also be used to predict forced response. Although these may give estimates of the natural frequencies, often the estimates are not accurate enough to ensure the safe reliable operation of the machine because the intended operating speed may

1

be too close to a critical speed. Finite element methods for rotor dynamic analysis exist, but for many of the complex geometries encountered the required accuracy cannot be achieved.

The presence of shrunk-on wheels or disks, and step changes in shaft diameter reduce the accuracy of beam finite element modelling of rotor dynamics. In particular, abrupt changes in shaft section cause localized changes to the stiffness of the shaft. In 1977, Sanderson and Kitching [2] examined the flexibility effects of an abrupt change in shaft diameter for the case of a beam statically loaded in pure bending. Their experimental beam with a four point loading system is shown in Fig. 1.1. The stepped section was centered in the span, and the load was also symmetrical about the mid-span of the beam. By measuring the actual deflection or radius of curvature of the neutral axis at various longitudinal positions, and knowing the local bending moment at the corresponding points, they were able to calculate the local effective stiffness. Simple bending theory predicts that the stiffness is proportional to the second moment of area, $I$. Therefore, the theoretical stiffness of the shaft in static bending should have a step change in value proportional to the second moment of area at the point the cross-section increases. The theoretical $I$ is indicated by the dashed lines in Fig. 1.1; the short dashes represent the values based on the small diameter, $d$, and the long dashes represent those based on the large diameter, $D$. A typical experimentally determined second moment of area curve, $I(x)$, is shown as a solid line in the figure. Their experimental results show that the actual effective second moment of area or stiffness is highly dependent on the ratio of large to small diameter, as well as the ratio of the length of the step increase to the small diameter. It can be seen that as a step increase in section height is approached in the longitudinal direction, the effective stiffness goes through a minimum and then peaks to a maximum value just after the increase in section. The maximum and minimum values, and curve shape are influenced by the ratios as well. In fact, the peak may become quite narrow and approach infinity for large
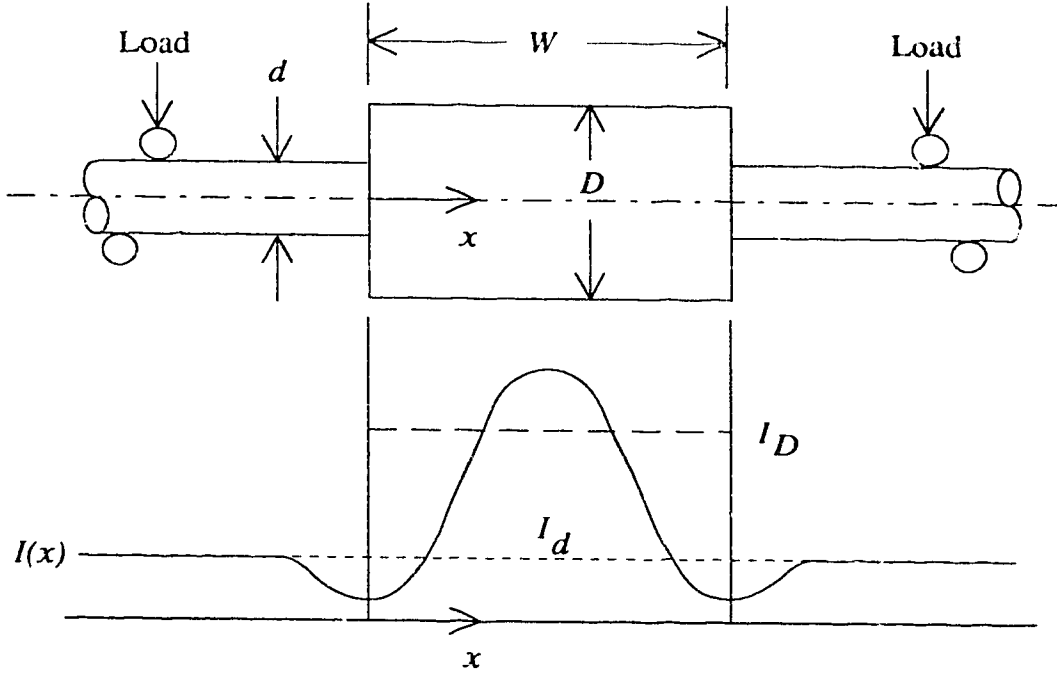
**FIGURE 1.1**: Stiffness Effects of a Step Change in Cross-Section

diameter ratios with short step lengths. However, for most cases the local effect of the discontinuity on stiffness takes place within $x/d = \pm 1.0$, where $x$ is the longitudinal position from the discontinuity.

Beyond the design and manufacture stage of a machine, the need exists for a reliable method or tool that will help the engineer in industry analyze the rotor dynamics of a machine throughout its operating life. The tool may be used in the diagnosis of vibration problems that may be encountered, as well as being used to perform the balancing calculations necessary after routine maintenance, or even to predict or check the possible dynamic consequences of altering the machine shaft or support systems. Not only should the method be reliable, it must be accessible to the industrial engineer. That is, the tool must not require an extremely complicated, large degree of freedom mathematical model that would exceed the storage or computational power of the desktop computer.

Having established the need for a reliable cost-effective means of analyzing the rotor dynamics, it is hoped that the improvements and extensions to the finite element method developed in this thesis will help in this endeavour. This thesis presents some improvement of the finite element method for rotor dynamic analysis in three areas. First, a new shaft element formulated on the basis of three dimensional elasticity is presented. Second, a condensation procedure for doing the forced analysis and calculating the natural frequencies of a system, while using only a small amount of computer memory, is presented. And finally, a method is given for improving or refining an existing finite element model to render any subsequent forced response analysis more accurate.

These methods are independent and may be used individually or as a whole to improve the finite element method for rotor dynamics problems. However, the condensation procedure and the refinement method in particular will lend themselves to elasto-dynamics problems of any kind. It is hoped that the work will lead to complete accurate finite element models of new turbomachines being presented to users by the manufacturers as an integral part of the maintenance manuals, and performance curves.

The remainder of this chapter gives brief descriptions of each of the following chapters of this thesis.

Chapter 2 discusses the Timoshenko one-dimensional beam element that is in widespread use today, and gives an introduction of its use to model shaft vibrations. A non-rotating shaft or beam may be modelled as two uncoupled beams vibrating in perpendicular transverse planes (i.e., in the horizontal and vertical planes). When the shaft is rotating the gyroscopic effect couples the motion of the two planes, and introduces the possibility of shaft whirl. That is, forces may cause the shaft to whirl about its elastic center. When the frequency of whirl is the same as the shaft rotation speed, any out of balance forces may excite or increase the whirl amplitude to an excessive or damaging level. Also included is a discussion of the

practical numerical difficulties encountered when using the Meirovitch method for finding eigenvalues of an undamped gyroscopic system.

In Chapter 3, the quasi-axisymmetric shaft element is developed. This element is more accurate in that its formulation is based on three-dimensional elasticity principles rather than the one-dimensional simple bending theory. The element is developed first for the case of in-plane bending, and then the element is given its full two plane bending shaft implementation, and results are shown. One possible method for joining a simple beam-shaft element to the axisymmetric element is included.

The boundary conditions of a rotating shaft can have a profound effect on the dynamic response of the machine and can be most difficult to model. Chapter 4 is a brief discussion of the state of the art of modelling of journal bearings, and how the journal bearings affect the dynamic characteristics of a rotating shaft. Also included is a short description of the method for including the bearing support and foundation system into a finite element model.

A model with complex geometry can take large amounts of storage space and computational time when calculating the free vibration characteristics or the forced vibration responses. Chapter 5 presents a method that is much like the transfer matrix method; at each frequency step over the range of interest, the dynamic matrix for each element is formed and then assembled or condensed into the global dynamic matrix. At each stage of assembly the global dynamic matrix only retains the desired nodes. That is, the interconnecting degrees of freedom between elements are condensed out as the assembly takes place. In this manner the global dynamic matrix for a particular vibration frequency can be formed having only the same number of degrees of freedom as a single element, while providing the accuracy of the full degree of freedom global model. The response of the dynamic matrix to various frequencies may be examined to find the forced response of the system or may be examined to find the free vibration characteristics of the system (natural

frequencies). Results for a variety of undamped and damped cases are presented and comparisons of the accuracy of the condensed method to that of the full global model are given.

A completed finite element model of a rotor may make predictions which are different from those actually measured on a real system, and therefore a need to modify the model further exists. This modification is known as system identification or model refinement, and is a vital part of the modelling process. In Chapter 6 a refinement method is presented that is based on Rayleigh's Quotient. Using only the first few measured eigenvalues of the shaft in the free-free or simply supported state, the method calculates the correction factors for the individual element stiffnesses, so that the analytical model will provide the same natural frequencies as measured. After the model has been refined in this manner, it is then possible to use it for further vibration analysis or long term machinery health monitoring. Results based on numerical experiments, as well as the correction of a beam element model of a real shaft are presented.

# CHAPTER 2

# Beam Elements

*Once more unto the breach, dear friends, once more — Shakespeare*

## 2.1 Introduction

At present, beam elements or shaft elements based on beams vibrating in two perpendicular planes through the longitudinal axis are the primary finite elements used to model turbomachine shafts. This chapter presents an overview of the modelling beams and shafts with Timoshenko beam finite elements.

Beams were first modelled using stiffness element matrices formulated on simple Euler-Bernoulli bending theory, and with lumped mass matrices. Archer [3] first presented the consistent mass matrix for uniform Euler-Bernoulli beam elements. However, for higher vibration mode for beams which are short in relation to their depth, the predicted natural frequencies using simple bending theory are inaccurate. In these cases, the shear deformation and rotatory inertia of the beams cross-section have considerable effect on the dynamic characteristics, with the shear deformation having the greater effect. Rayleigh [4] included the effect of rotatory inertia into the vibration of beams. But Timoshenko [5], presented the differential equation of motion for beams including both effects, and hence elements based on this formulation are known as Timoshenko elements.

The Timoshenko differential equation was solved for a variety of boundary conditions using series solution techniques by Anderson [6] and Huang [7]. An important addition to the accuracy of the solutions was given by Cowper [8], who integrated the three-dimensional elasticity equations to get the Timoshenko beam theory, and derived a new equation for the shear correction coefficient. The Cowper shear correction coefficients are used throughout this thesis. A finite element using the Timoshenko formulation was again presented by Archer [9], albeit with mistakes in the consistent mass matrix as noted by Thomas, et al. [10]. Davis, Henshell and Warburton [11] formulated an element using static equilibrium and assuming constant shear force and angle for the element, which gave the same corrected matrices as Archer. The Archer or Davis elements are simple elements with two nodes, and the unknowns being the total transverse displacement and bending angle at each node. Numerous other researchers have presented enhanced versions of the Timoshenko beam element with additional nodes, and/or unknowns for shear displacement and shear angle (for example, Kapur [12]). However, the Archer/Davis element is still most widely used for the dynamic modelling of beams.

Section 2.2 of this chapter presents the Timoshenko beam element as formulated by Davis et al. [11], however, the matrix equations are derived from Hamilton's Principle.

Section 2.3 expands the beam representation to that modelling a shaft. The shaft is considered to be two Timoshenko beam elements vibrating in perpendicular transverse planes. Coupling between the planes is due to the gyroscopic effects of angular displacements of the spinning shaft sections, and the skew-symmetric gyroscopic matrix is developed using Lagrange's Equation. Although the notation here is unique, the shaft matrices presented are well known (Nelson [13]). In addition, a discussion of the solution of the eigenvalue problem when using the Meirovitch method [14] for gyroscopic systems, and its inherent numerical difficulties is presented.

## 2.2 Beam Models

First, the Timoshenko governing differential equation for a beam undergoing transverse vibration is derived. Details are given in Appendix A.1. Consider the infinitesimal element undergoing flexural vibration, as shown in Fig. 2.1, where the bending moment, shear force, and distributed load are designated by $M$, $F$, and $q$. The total transverse deflection is $w$, and the total angle is given by the bending angle less the shear angle, i.e. $w' = \theta - \psi$. The bending transverse deflection is denoted as $w_b$, and the bending angle is $\theta$. The strain energy, $U$, the kinetic energy, $T$, and the external work done by applied applied forces, $W_{ext}$, of a beam of length $\ell$ may be written as:

$$U = \tfrac{1}{2} \int_0^\ell EI\, w_b''(x,t)^2 \, dx + \tfrac{1}{2} \int_0^\ell KGA_x\, \psi(x,t)^2 \, dx$$

$$T = \tfrac{1}{2} \int_0^\ell \rho A_x\, \dot{w}^2(x,t) \, dx + \tfrac{1}{2} \int_0^\ell \rho I\, \dot{\theta}^2(x,t) \, dx \qquad (2.1)$$

$$W_{ext} = \int_0^\ell q(x,t)\, w(x,t) \, dx,$$

where $E$ is the modulus of elasticity, $I$ is the second moment of area, $K$ is the shear correction coefficient, $G$ is the modulus of rigidity, and $A_x$ is the cross-sectional area of the shaft.

The total strain energy, $U$, as given, is the sum of the strain energy due to bending deformation, and shear deformation of the beam. The kinetic energy consists of the energy due to total transverse translation of the beam plus the energy due to rotation of the beam cross-section caused by bending. The external work is simply the product of the applied external forces and total transverse displacements of the beam. The applied forces are considered to be conservative. That is, the work done is dependent on the end points of the displacement rather than the path the displacement takes.
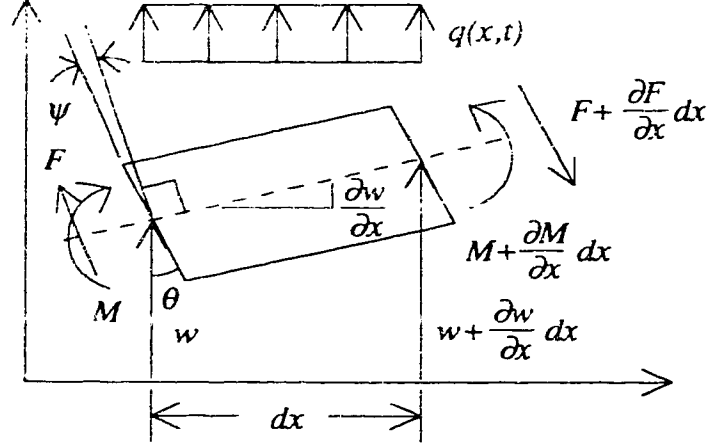
**FIGURE 2.1**: Infinitesimal Element

Hamilton's Principle is written as:

$$\delta \int_{t_1}^{t_2} (W_{ext} + T - U)\, dt = 0.$$

(2.2)

Hamilton's Principle states that the first variation of the Lagrangian has a stationary value for the correct motion. Taking the first variation, $\delta$, of Eq. (2.2) inside the time integral, and substituting in the relationships given by Eq. (2.1) results in:

$$\int_{t_1}^{t_2} \int_0^\ell (q\,\delta w + \rho A_\bot \ddot{w}\,\delta w + \rho I\,\ddot{\theta}\,\delta\theta - EI\,w_b''\,\delta w_b'' - KGA_\bot \psi'\,\delta\psi)\, dx\, dt = 0.$$

(2.3)

Using $\psi = \theta - w' = w_b' - w'$. Eq. (2.3) may be rewritten in terms of the total transverse deflection and the bending angle, and their time and spatial derivatives. Then, integrating Eq. (2.3) by parts and following the rules of variational calculus, the variation of the two deflections leads to the following:

$$\rho I \frac{\partial^3 w_b}{\partial x \partial t^2} + KGA_r \left( \frac{\partial w_b}{\partial x} - \frac{\partial w}{\partial x} \right) - EI \frac{\partial^3 w_b}{\partial x^3} = 0$$

$$q - \rho A_r \frac{\partial^2 w}{\partial t^2} - KGA_r \left( \frac{\partial^2 w_b}{\partial x^2} - \frac{\partial^2 w}{\partial x^2} \right) = 0.$$

$$(2.4)$$

Manipulating Eq. (2.4) to eliminate the bending angle results in the Timoshenko governing partial differential equation of transverse vibration of a beam, Eq. (2.5), which includes the effects of rotatory inertia and shear deformation.

$$\rho A_r \frac{\partial^2 w}{\partial t^2} + EI \frac{\partial^4 w}{\partial x^4} - \rho I \frac{\partial^4 w}{\partial x^2 \partial t^2} - \frac{\rho EI}{KG} \frac{\partial^4 w}{\partial x^2 \partial t^2} + \frac{\rho^2 I}{KG} \frac{\partial^4 w}{\partial t^4} = 0 \qquad (2.5)$$

The first term of the Timoshenko equation on the left hand side represents the translational inertia, the second the restoring force, the third the rotatory inertia due to the bending of the element, the fourth the rotatory inertia due to the shear deformation of the element, and the fifth is a mixed term which is normally considered negligible. However, this equation does not lead to the numerical solution required by the finite element method directly. But, Eq. (2.3) can be used to get the matrix equation of motion if the appropriate approximate equations for displacement are included. If shear deformation and rotatory inertia are ignored, then only the first two terms on the right hand side remain, giving the Euler-Bernoulli equation for a prismatic beam in transverse vibration.

For a Timoshenko element, shown in Fig. 2.2, Davis, et al. [11] proposed that static equilibrium be used to define a constant shear force and shear angle $\psi$ along an element. The static equilibrium implies that the inertia of the element does not change the value of the shear force from one node of the element to the other. This approximation allows the use of only the total transverse displacement and bending angle at each node as the element unknowns. Approximations other than static equilibrium could also be used. Therefore, a third order polynomial is sufficient to
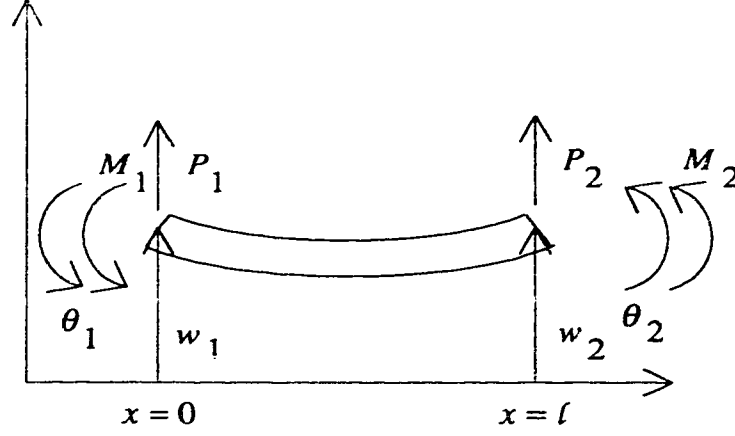
**FIGURE 2.2**: Element in Bending

describe the displacements, and the resulting equations are given by Eq. (2.6).

$$
\begin{aligned}
w(x) &= \frac{1}{EI}(\alpha_1 \frac{x^3}{6} + \alpha_2 \frac{x^2}{2} + \alpha_3 x + \alpha_4) \\
\theta(x) &= \frac{dw}{dx} + \psi = \frac{1}{EI}(\alpha_1 \frac{x^2}{2} + \alpha_2 x + \alpha_3) + \psi
\end{aligned}
\tag{2.6}
$$

The coefficients $(\alpha_i)$ are found by solving Eq. (2.6) in terms of the four nodal displacements and axial positions as shown in Fig. 2.2 (see Appendix A.2 for details). The nodal displacements (element unknowns) are the translational and angular displacements at each end of the element. Note that the angular displacements are the bending angles, $\theta_i$, only. The displacements are then given by:

$$
\begin{aligned}
w(x,t) &= \{B_o\}^T [T] \{w_e(t)\} \\
\psi(x,t) &= \{C\}^T [T] \{w_e(t)\} \\
\theta(x,t) &= \{D\}^T [T] \{w_e(t)\}.
\end{aligned}
\tag{2.7}
$$

The vectors, $\{B_o\}^T$, $\{C\}^T$, and $\{D\}^T$, multiplied by the transformation matrix,

$[T]$, are the hermitian polynomials for approximating the displacements throughout the element length. The vectors are

$$\{B_o\}^T = \frac{1}{EI} \lfloor \quad \frac{x^3}{6} \quad \frac{x^2}{2} \quad x \quad 1 \quad \rfloor$$

$$\{C\}^T = \frac{1}{EI} \lfloor \quad \beta \quad 0 \quad 0 \quad 0 \quad \rfloor \tag{2.8}$$

$$\{D\}^T = \frac{1}{EI} \lfloor \quad \frac{x^2}{2} + \beta \quad x \quad 1 \quad 0 \quad \rfloor,$$

where $\beta = EI/KGA_x$. The transformation matrix is:

$$[T] = \frac{EI}{\ell(\ell^2 + 12\beta)} \begin{bmatrix} 12 & 6\ell & -12 & 6\ell \\ -6\ell & (-4\ell^2 - 12\beta) & 6\ell & (-2\ell^2 + 12\beta) \\ -12\beta & (\ell^3 + 6\beta\ell) & 12\beta & -6\beta\ell \\ \ell(\ell^2 + 12\beta) & 0 & 0 & 0 \end{bmatrix}. \tag{2.9}$$

The nodal unknown vector for one beam element is:

$$\{w_e(t)\} = \lfloor \quad w_1(t) \quad \theta_1(t) \quad w_2(t) \quad \theta_2(t) \quad \rfloor^T. \tag{2.10}$$

Substituting the relationships for displacements given by Eq. (2.7) into the variational integral, Eq. (2.3), and assuming the forcing function, $q = 0$, results in Eq. (2.11) the matrix form of Hamilton's Principle. Details of the procedure are given in Appendix A.3.

$$\int_{t_1}^{t_2} (-\{\delta\ddot{w}_e\}^T[M_e]\{\ddot{w}_e\} + \{\delta w_e\}^T[K_e]\{w_e\}) \, dt = 0 \tag{2.11}$$

Integrating Eq. (2.11) by parts, setting the resulting integrand to zero, letting $\{w_e\} = \{0\}$ at $t = t_1$ and $t = t_2$, and remembering that $\{\delta w_e\}^T$ is arbitrary results in the matrix equation of motion:

$$[M_e]\{\ddot{w}_e\} + [K_e]\{w_e\} = 0. \tag{2.12}$$

The stiffness matrix is represented by the following integral:

$$[K_e] = \int_0^\ell (EI[T]^T\{B_o''\}\{B_o''\}^T[T] + KGA_x[T]^T\{C\}\{C\}^T[T])\,dx. \tag{2.13}$$

Completing the integration results in the explicit stiffness matrix:

$$[K_e] = \frac{EI}{\ell(\ell^2 + 12\beta)}\begin{bmatrix} 12 & 6\ell & -12 & 6\ell \\ 6\ell & 4\ell^2 + 12\beta & -6\ell & 2\ell^2 - 12\beta \\ -12 & -6\ell & 12 & -6\ell \\ 6\ell & 2\ell^2 - 12\beta & -6\ell & 4\ell^2 + 12\beta \end{bmatrix}. \tag{2.14}$$

Similarly, the mass matrix integral of the beam element is given by:

$$[M_e] = \int_0^\ell (\rho A_x[T]^T\{B_o\}\{B_o\}^T[T] + \rho I[T]^T\{D\}\{D\}^T[T])\,dx. \tag{2.15}$$

Again, completing the integration results in the following consistent mass matrix:

$$[M_e] = \frac{\rho A_x \ell}{(1 + \phi)^2}\begin{bmatrix} m_1 & m_2 & m_3 & m_4 \\ & m_5 & -m_4 & m_6 \\ \text{sym.} & & m_1 & -m_2 \\ & & & m_5 \end{bmatrix} + \frac{\rho I}{\ell(1 + \phi)^2}\begin{bmatrix} m_7 & m_8 & -m_7 & m_8 \\ & m_9 & -m_8 & m_{10} \\ \text{sym.} & & m_7 & -m_8 \\ & & & m_9 \end{bmatrix},$$

where,

$$m_1 = \tfrac{13}{35} + \tfrac{7}{10}\phi + \tfrac{1}{3}\phi^2 \qquad m_6 = -\tfrac{1}{140}\ell^2 - \tfrac{1}{60}\phi\ell^2 - \tfrac{1}{120}\phi^2\ell^2$$

$$m_2 = \tfrac{11}{210}\ell + \tfrac{11}{120}\phi\ell + \tfrac{1}{24}\phi^2\ell \qquad m_7 = \tfrac{6}{5}$$

$$m_3 = \tfrac{9}{70} + \tfrac{3}{10}\phi + \tfrac{1}{6}\phi^2 \qquad m_8 = \tfrac{1}{10}\ell - \tfrac{1}{2}\phi\ell$$

$$m_4 = -\tfrac{13}{420}\ell - \tfrac{3}{40}\phi\ell - \tfrac{1}{24}\phi^2\ell \qquad m_9 = \tfrac{2}{15}\ell^2 + \tfrac{1}{6}\phi\ell^2 + \tfrac{1}{3}\phi^2\ell^2$$

$$m_5 = \tfrac{1}{105}\ell^2 + \tfrac{1}{60}\phi\ell^2 + \tfrac{1}{120}\phi^2\ell^2 \qquad m_{10} = -\tfrac{1}{30}\ell^2 - \tfrac{1}{6}\phi\ell^2 + \tfrac{1}{6}\phi^2\ell^2,$$

and $\phi = 12EI/KGA_x\ell^2$.

The above formulation is based on bending theory, with the inclusion of rotatory inertia, and the effects of shear deformation. But, because the shear force and shear angle are considered constant along the length of an element, this beam element does not represent the higher modes of deep section beams as accurately as more refined elements. This formulation of the Timoshenko beam element is, however, much more accurate than a Euler-Bernoulli element at predicting the natural frequencies of higher modes, without an increase in matrix element size. Therefore, the Archer/Davis element represents a good compromise between mathematical and computational complexity, and accuracy.

The angular displacement chosen was the rotation of the cross-section due to pure bending of the beam. At a fixed end, the kinematic boundary conditions are met. That is, the bending angle at the end may be constrained to zero, and the angle due to shear deformation is then $\psi = F/KGA_x$.

Typical boundary conditions can be modelled quite easily with this element. For a pinned position, extra stiffness is added to the translational degree of freedom at that point, or that unknown is rigidly constrained from the system. For a clamped end, both the translational and rotational degrees of freedom are rigidly constrained.

To model a complete beam, a number of discrete elements are connected to each other end to end, as shown in Fig. 2.3. The matrices for each finite element are
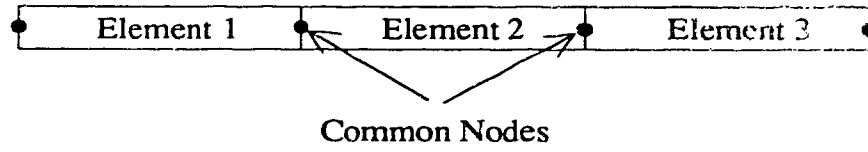
**FIGURE 2.3**: Chain Assembled Finite Element Beam Model

assembled into global matrices, while maintaining continuity of displacement and force equilibrium at the end nodes, to form an overall system of equations:

$$[M]\{\ddot{x}\} + [K]\{x\} = \{f\}. \tag{2.17}$$

The matrices, $[M]$ and $[K]$, are now the global mass and stiffness matrices, and $\{x\}$ and $\{f\}$, are the global displacement unknown and force vectors, respectively. The homogeneous form of the equations, Eq. (2.17), is solved to find the natural frequencies of the beam in transverse vibration by assuming a harmonic solution $\{x\} = \{X\}\sin(\omega t)$, to give the following eigenvalue problem.

$$([K] - \omega^2[M])\{X\} = \{0\} \tag{2.18}$$

In this eigenvalue problem, the matrices, $[K]$ and $[M]$, are symmetric, with $[M]$ positive definite, and $[K]$ semi-positive or positive definite depending on the system constraints. This type of eigenvalue problem can easily be solved using methods such as Jacobi's, or the power method.

## 2.3 Shaft Models

Non-rotating shafts can be modelled as two uncoupled beams vibrating in perpendicular transverse planes as shown in Figure 2.4. The translational and
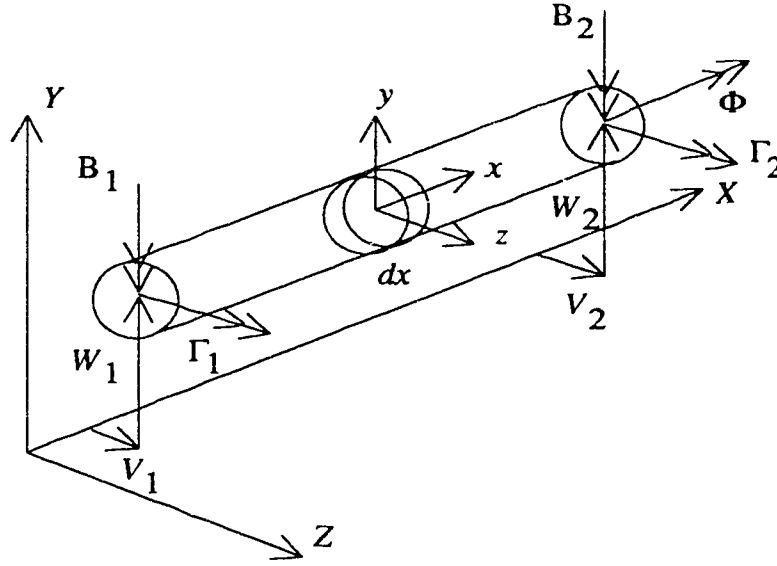
**FIGURE 2.4**: Shaft Finite Element

angular displacement unknowns in the $YX$ plane are given by $W$ and $\Gamma$, while the displacements in the $ZX$ plane are $V$ and B.

When the shaft is spinning with constant angular velocity $\dot{\Phi}$ along its axis, then any angular displacement of the shaft section will introduce gyroscopic effects, which couples the motion in both planes. This can be quantified by examining the transformation from an inertial system of axes $XYZ$ to body fixed (rotating) axes $xyz$ as shown in Figure 2.5. The axis of the shaft is $X$. Note that the rotation vector, $\vec{B}$, points in the opposite direction to the $Y$ axis. This allows the transverse and angular nodal displacements in the two lateral planes to have the same relative orientation, and hence the portions of the stiffness matrix relating to each plane will be the same, resulting in reduced computational time. The shaft element mass and stiffness matrices are uncoupled, with the only coupling of the motions in the two planes being provided by the gyroscopic matrix which will be developed. The stiffness and mass matrices are of the form:
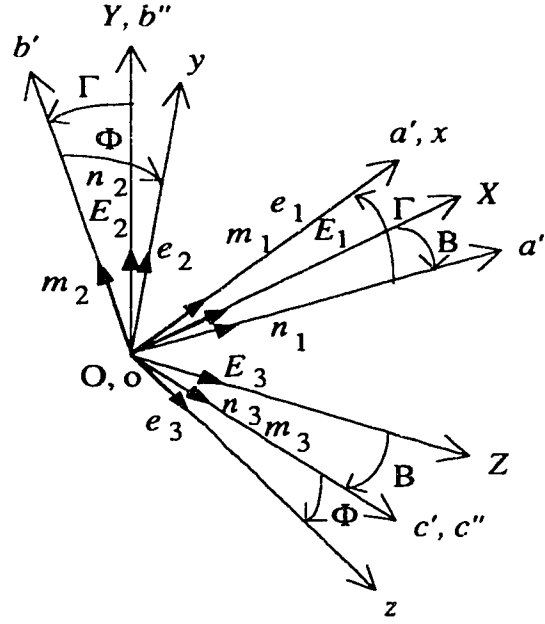
**FIGURE 2.5**: Transformation of Inertial to Rotating Axes

$$[K_e]_{\text{shaft}} = \begin{bmatrix} [K_e] & [0] \\ [0] & [K_e] \end{bmatrix} \quad [M_e]_{\text{shaft}} = \begin{bmatrix} [M_e] & [0] \\ [0] & [M_e] \end{bmatrix}, \qquad (2.19)$$

where $[K_e]$ and $[M_e]$ are given by Eq. (2.14) and Eq. (2.16), the beam element matrices.

The angular velocity in the inertial frame will be expressed in terms of a rotating coordinate (body fixed) unit vectors using Cardan angles of the second kind.

First rotate $-B$ about $Y$ ($-B$ in the right-handed sense of the $Y$-axis):

$$\left\{ \begin{array}{c} \vec{E}_1 \\ \vec{E}_2 \\ \vec{E}_3 \end{array} \right\}_{XYZ} = \begin{bmatrix} \cos(B) & 0 & -\sin(B) \\ 0 & 1 & 0 \\ \sin(B) & 0 & \cos(B) \end{bmatrix} \left\{ \begin{array}{c} \vec{n_1} \\ \vec{n_2} \\ \vec{n_3} \end{array} \right\}_{a''b''c''} , \qquad (2.20)$$

where $\vec{E}_i$ are the inertial system unit vectors, and $\vec{n}_i$ are the unit vectors of the $a''b''c''$ coordinate system.

Second rotate $\Gamma$ about $c''$:

$$\left\{ \begin{array}{c} \vec{n}_1 \\ \vec{n}_2 \\ \vec{n}_3 \end{array} \right\}_{a''b''c''} = \left[ \begin{array}{ccc} \cos(\Gamma) & -\sin(\Gamma) & 0 \\ \sin(\Gamma) & \cos(\Gamma) & 0 \\ 0 & 0 & 1 \end{array} \right] \left\{ \begin{array}{c} \vec{m}_1 \\ \vec{m}_2 \\ \vec{m}_3 \end{array} \right\}_{a'b'c'} , \qquad (2.21)$$

where $\vec{m}_i$ are the unit vectors in the $a'b'c'$ coordinate system.

Lastly rotate $\Phi$ about $a'$:

$$\left\{ \begin{array}{c} \vec{m}_1 \\ \vec{m}_2 \\ \vec{m}_3 \end{array} \right\}_{a'b'c'} = \left[ \begin{array}{ccc} 1 & 0 & 0 \\ 0 & \cos(\Phi) & -\sin(\Phi) \\ 0 & \sin(\Phi) & \cos(\Phi) \end{array} \right] \left\{ \begin{array}{c} \vec{e}_1 \\ \vec{e}_2 \\ \vec{e}_3 \end{array} \right\}_{xyz} , \qquad (2.22)$$

where $\vec{e}_i$ are the unit vectors for the body fixed (rotating) coordinate system $xyz$.

The total angular velocity for the infinitesimal element is given by:

$$\vec{\omega} = -\dot{B}\vec{E}_2 + \dot{\Gamma}\vec{n}_3 + \dot{\Phi}\vec{m}_1. \qquad (2.23)$$

Transforming the angular velocity by converting the unit vectors to the rotating frame vectors using the given rotation matrices, and assuming small angular displacements for $\Gamma$ and $B$, ($\sin(\Gamma) \approx \Gamma$, $\cos(\Gamma) \approx 1$, $\sin(B) \approx B$, and $\cos(B) \approx 1$), the angular velocity of the shaft element of length $dx$ can be written as:

$$\vec{\omega} = (\dot{\Phi} - \dot{B}\Gamma)\vec{e}_1 + (\dot{\Gamma}\sin\Phi - \dot{B}\cos\Phi)\vec{e}_2 + (\dot{\Gamma}\cos\Phi + \dot{B}\sin\Phi)\vec{e}_3. \qquad (2.24)$$

The kinetic energy of the infinitesimal shaft element due to the angular velocities can be written as:

$$dT_{\text{rot}} = \frac{1}{2}\vec{w}^T[dI]\vec{w},$$ (2.25)

where $[dI] = \begin{bmatrix} dI_x & 0 & 0 \\ 0 & dI_y & 0 \\ 0 & 0 & dI_z \end{bmatrix}$, $dI_x = dI_p$, and $dI_y = dI_z = dI_d$.

Substituting in the angular velocity, the kinetic energy can be rewritten as:

$$dT_{\text{rot}} = \frac{1}{2}\left[(\dot{\Phi}^2 - 2\dot{\Phi}\dot{B}\Gamma)dI_p + (\dot{\Gamma}^2 + \dot{B}^2)dI_d\right].$$ (2.26)

The first term of Eq. (2.26) is the kinetic energy due to the spinning of the shaft. Since the rotation of the shaft element is prescribed in that direction, this component of the expression makes no contribution to the element matrices. The gyroscopic kinetic energy for the infinitesimal element is given by the second term of Eq. (2.26), and will be used to calculate the gyroscopic matrix for the element. The final two terms of the equation represent the energy due to the angular velocity of the shaft cross section. But these terms are already incorporated into the mass matrix of the shaft element by the rotatory inertia terms. Taking only the gyroscopic portion of the kinetic energy of an infinitesimal length of shaft, and integrating over the element length, the total gyroscopic kinetic energy is given by:

$$T_{\text{gyro}} = -\int_0^\ell \dot{\Phi}\dot{B}\Gamma\, dI_p.$$ (2.27)

The angular displacements are given by:

$$\Gamma(X) = \frac{\partial W}{\partial X} + \psi$$

$$B(X) = \frac{\partial V}{\partial X} + \mu.$$

(2.28)

where, $\psi$ and $\mu$ are the shear angles in their respective planes. The angular displacements may be written in terms of the element nodal unknowns as:

$$\Gamma(X) = \lfloor \{D\}^T \{0\}^T \rfloor [T_1]\{\delta_e\}$$

$$B(X) = \{\delta_e\}^T [T_1]^T \lfloor \{0\}^T \{D\}^T \rfloor^T,$$

(2.29)

and, where:

$$[T_1] = \begin{bmatrix} [T] & [0] \\ [0] & [T] \end{bmatrix}.$$

(2.30)

Also, $\{D\}$ and $[T]$ are defined by the single plane equations Eq. (2.8) and Eq. (2.9). The nodal unknown vector for the shaft element is:

$$\{\delta_e\} = \lfloor W_1 \quad \Gamma_1 \quad W_2 \quad \Gamma_2 \quad V_1 \quad B_1 \quad V_2 \quad B_2 \rfloor^T.$$

(2.31)

Substituting in the angular displacement functions and expressing the gyroscopic kinetic energy in matrix form gives:

$$T_{\text{gyro}} = -\dot{\Phi}\{\dot{\delta}_e\}^T [A] \{\delta_e\},$$

(2.32)

where:

$$[A] = \int_0^\ell \begin{bmatrix} [0] & [0] \\ [T]^T \{D\}\{D\}^T[T] & [0] \end{bmatrix} dI_p. \tag{2.33}$$

Adding this gyroscopic kinetic energy term to the Lagrangian and working through Lagrange's equation results in the additional term:

$$\frac{d}{dt}(-\dot{\Phi}[A]\{\delta_e\}) - (-\dot{\Phi}[A]^T\{\dot{\delta_e}\}) = \dot{\Phi}([A]^T - [A])\{\dot{\delta_e}\} = 0. \tag{2.34}$$

Adding Eq. (2.34) to the equation of motion gives the new equation of motion with the gyroscopic matrix:

$$[M]\{\ddot{x}\} + [G]\{\dot{x}\} + [K]\{x\} = \{F\}, \tag{2.35}$$

where the gyroscopic matrix for the shaft element is:

$$[G_e]_{\text{shaft}} = \dot{\Phi}([A]^T - [A]) = \dot{\Phi} \begin{bmatrix} [0] & [A'] \\ -[A'] & [0] \end{bmatrix}. \tag{2.36}$$

The $[A']$ matrix is explicitly:

$$[A'] = \frac{\rho A_x d^2}{240(1 + \phi)^2 \ell} \begin{bmatrix} 36 & (3 - 15\phi)\ell & -36 & (3 - 15\phi)\ell \\ (3 - 15\phi)\ell & (4 + 5\phi + 10\phi^2)\ell^2 & -(3 - 15\phi)\ell & (-1 - 5\phi + 5\phi^2)\ell^2 \\ -36 & -(3 - 15\phi)\ell & 36 & -(3 - 15\phi)\ell \\ (3 - 15\phi)\ell & (-1 - 5\phi + 5\phi^2)\ell^2 & -(3 - 15\phi)\ell & (4 + 5\phi + 10\phi^2)\ell^2 \end{bmatrix}, \tag{2.37}$$

where $A_x$ = cross sectional area, $d$ = diameter, and $\phi = \frac{12EI}{KGA_x\ell^2}$.

The gyroscopic element matrix is skew-symmetric and couples the motion of the two perpendicular transverse planes of vibration. The three element matrices, mass,

stiffness, and gyroscopic, now fully describe a shaft element for undamped motion. These shaft elements are again chain assembled, as the beam elements were, and any additional effects of disks are added in to the global mass and gyroscopic matrices.

Solving the eigenvalue problem involves assuming a solution of the form $\{x\} = \{X\} e^{i\omega t}$, and results in the equation:

$$(([K] - \omega^2[M]) + i\omega[G])\{X\} = \{0\}. \tag{2.38}$$

As with the beam formulation, the mass and stiffness matrices are symmetric, positive definite and semi-definite respectively. However, the skew-symmetric gyroscopic matrix creates a complex eigenvalue problem. For conservative gyroscopic systems, Meirovitch [14] recommends introducing a new state vector, $\{q\} = \lfloor\{\dot{x}\}^T \ \{x\}^T\rfloor^T$, which adds the following identity to the homogeneous version of Eq. (2.35):

$$[K]\{\dot{x}\} - [K]\{\dot{x}\} = \{0\}. \tag{2.39}$$

Combining Eq. (2.35) and Eq. (2.39) results in a new equation of motion, Eq. (2.40), which has twice the number of global degrees of freedom as the original problem. That is, if the original shaft model had $n$ degrees of freedom, the new equation has $2n$.

$$[M^*]\{\dot{q}\} + [G^*]\{q\} = \{0\} \tag{2.40}$$

where:

$$[M^*] = \begin{bmatrix} [M] & [0] \\ [0] & [K] \end{bmatrix} \quad [G^*] = \begin{bmatrix} [G] & [K] \\ -[K] & [0] \end{bmatrix}. \tag{2.41}$$

stiffness, and gyroscopic, now fully describe a shaft element for undamped motion. These shaft elements are again chain assembled, as the beam elements were, and any additional effects of disks are added in to the global mass and gyroscopic matrices.

Solving the eigenvalue problem involves assuming a solution of the form $\{x\} = \{X\} e^{i\omega t}$, and results in the equation:

$$(([K] - \omega^2[M]) + i\omega[G])\{X\} = \{0\}. \tag{2.38}$$

As with the beam formulation, the mass and stiffness matrices are symmetric, positive definite and semi-definite respectively. However, the skew-symmetric gyroscopic matrix creates a complex eigenvalue problem. For conservative gyroscopic systems, Meirovitch [14] recommends introducing a new state vector, $\{q\} = \lfloor \{\dot{x}\}^T \ \{x\}^T \rfloor^T$, which adds the following identity to the homogeneous version of Eq. (2.35):

$$[K]\{\dot{x}\} - [K]\{\dot{x}\} = \{0\}. \tag{2.39}$$

Combining Eq. (2.35) and Eq. (2.39) results in a new equation of motion, Eq. (2.40), which has twice the number of global degrees of freedom as the original problem. That is, if the original shaft model had $n$ degrees of freedom, the new equation has $2n$.

$$[M^*]\{\dot{q}\} + [G^*]\{q\} = \{0\} \tag{2.40}$$

where:

$$[M^*] = \begin{bmatrix} [M] & [0] \\ [0] & [K] \end{bmatrix} \quad [G^*] = \begin{bmatrix} [G] & [K] \\ -[K] & [0] \end{bmatrix}. \tag{2.41}$$

The new augmented mass matrix. $[M^*]$, is symmetric and the augmented gyroscopic matrix, $[G^*]$, is skew-symmetric. The equation of motion, Eq. (2.40), is converted to an eigenvalue problem by substituting, $\{q\} = \{Q\}\, e^{st}$. This eigenvalue problem results in pairs of purely imaginary complex conjugate pairs of eigenvalues of the form $s_n = \pm \omega_n$. The corresponding eigenvectors are also complex conjugate pairs of vectors of the form $\{Q_n\} = \{R_n\} + i\,\{S_n\}$. Complex conjugate pairs of eigenvalues are expected. Consider a non-rotating cantilevered shaft with disk or mass at the free end vibrating in its fundamental mode. The free end would follow a conical (circular) orbit, with the precession occurring in either direction. The angular speed or frequency of precession would be identical in either direction. If the shaft were rotating, the gyroscopic moment of the disk would split the frequency of precession into two. The lower frequency pair would equal backward precession. That is, the disk would precess in a direction opposite to the shaft rotation. The higher value frequency pair is the forward precession whirl speed, where the precession is in the same direction as the shaft rotation. In practice, backward precession is only excited when the stiffnesses in the two planes are not equal.

Further, Meirovitch recommends that the problem be converted to a real and symmetric set of matrices by, $[K^*] = [G^*]^T [M^*]^{-1} [G^*]$. A symmetric eigensolver such as the Jacobi method could now be used with the new augmented stiffness and mass matrices, giving repeated pairs of real eigenvalues. However, if the augmented matrices are examined, it can be seen that they have the form:

$$[K^*] = \begin{bmatrix} [G]^T [M]^{-1} [G] + [K] & [G]^T [M]^{-1} [K] \\ [K]^T [M]^{-1} [G] & [K]^T [M]^{-1} [K] \end{bmatrix}$$

$$(2.42)$$

$$[M^*] = \begin{bmatrix} [M] & 0 \\ 0 & [K] \end{bmatrix}.$$

Unfortunately, the numerical order of the individual elements in the mass and stiffness matrices in the augmented mass matrix are significantly different. Also the terms in the lower right corner of the augmented stiffness matrix are much larger than the gyroscopic terms in the upper left of the matrix. Therefore, if the shaft is short and heavy, the stiffness terms overwhelm the problem numerically, producing incorrect eigenvalues and vectors. For example, a stiff steel simply supported shaft with a disk at the mid-span was modelled. The model was comprised of four elements, each twelve inches long and six inches in diameter, and with a disk 24 inches in diameter and two inches thick. The stiffnesses in both planes were equal and the shaft was not rotating. Hence, the problem was the same as two uncoupled beams vibrating in their own planes. The expected eigenvalues in this case should have been equal in both directions, and should have been the same as those of a simply supported beam with a disk in the middle. Using Timoshenko beam elements, and treating the model as a single plane beam, the predicted fundamental natural frequency was 8120 CPM in bending. Using the above Meirovitch method on the same configuration modelled with full Timoshenko shaft elements and double precision, the natural frequencies for each plane were calculated, and are given in Table 2.1. The natural frequencies calculated by the method described below (Gen. Dyn. Sys.) are also given in Table 2.1. As shown, the Meirovitch gyroscopic system method can lead to significant numerical errors even when no gyroscopic effects exist. With larger models (more degrees of freedom), the numerical problem is exaggerated, making it difficult to calculate natural frequencies of a non-rotating or low-speed shaft.

A more satisfactory method of solving the eigenvalue problem is to treat the system as a general dynamic system. The equation of motion:

$$[M]\{\ddot{x}\} + [G]\{\dot{x}\} + [K]\{x\} = \{0\}, \tag{2.43}$$

**TABLE 2.1**: Natural Frequencies (CPM) of Simply Supported Shaft with Disk

| Mode | Meirovitch Method | | Gen. Dyn. Sys. | |
|------|---------|---------|---------|---------|
|      | Plane 1 | Plane 2 | Plane 1 | Plane 2 |
| 1    | 8121    | 8635    | 8120    | 8120    |
| 2    | 33447   | 35244   | 33447   | 33447   |
| 3    | 78642   | 80978   | 78642   | 78642   |

$E = 30 \times 10^6$ psi., $\nu = 0.30$, $\rho = 0.283$ lb./cu. in., $K = 0.886$

is again transformed by introducing the state vector $\{q\} = \lfloor \{\dot{x}\}^T \ \{x\}^T \rfloor^T$. In this case the equation of motion is now rewritten as:

$$[\hat{M}]\{\dot{q}\} + [\hat{K}]\{q\} = \{0\}, \tag{2.44}$$

where:

$$[\hat{M}] = \begin{bmatrix} [M] & [0] \\ [0] & [I] \end{bmatrix} \quad [\hat{K}] = \begin{bmatrix} [G] & [K] \\ -[I] & [0] \end{bmatrix}. \tag{2.45}$$

The problem is further reduced to a single matrix problem:

$$[A]\{x\} = \lambda\{x\}, \tag{2.46}$$

where:

$$[A] = -[\hat{M}]^{-1}[\hat{K}] = \begin{bmatrix} -[M]^{-1}[G] & -[M]^{-1}[K] \\ [I] & [0] \end{bmatrix}. \tag{2.47}$$

The $[A]$ matrix is a non-symmetric real matrix of order $2n$, which in general has complex eigenvalues. The problem can be solved by transforming the matrix to Hessenberg form, and solving for the complex eigenvalues using the $QR$ method. The resulting eigenvalues occur in complex conjugate pairs and are of the form $\lambda = \alpha \pm i\beta$. Using this method, one can predict the natural frequencies of a shaft as it spins about its axis. The forward and backward whirl speeds will come out of the solution directly as the complex term $\beta$. For a conservative gyroscopic system, the eigenvalues are purely imaginary. When damping is included, the velocity term becomes $[G]+[C]$, and the eigenvalues are complex. The damping matrix is normally symmetric, and in this case, $\alpha$ is the damping factor times the undamped natural frequency and $\beta$ is the damped natural frequency for that critical speed.

Boundary conditions are applied to a shaft model in a similar manner as to the beam model, however the constraints are applied in both planes of vibration. Also, if bearings are modelled, then cross-coupling stiffness and damping terms between planes must be added at the bearing location.

To demonstrate the method, a mathematical model of a simply supported multi-disk turbine was generated, as shown in Figure 2.6. The model consisted of seven equal dimension circular Timoshenko shaft elements with six equal dimension disks. The first three backward and forward whirl speeds are shown in Figure 2.7 for shaft speeds of 0 to 11000 RPM. For the first mode, the shaft speed did not have significant effect on the whirl speed of the shaft. However, for the second and third modes, the shaft speed changed the whirl speed by up to 10 percent. That is, at a shaft speed of 11000 RPM, the non-rotating third natural frequency of 21715 RPM split into a backward whirl speed of 20442 RPM and a forward whirl speed of 22988 RPM. In general, the gyroscopic effect is negligible unless the shaft has many disks on a fairly flexible shaft, or a large disk is overhung on a flexible shaft.

$$E = 30 \times 10^6 \text{ psi}, \quad \rho = 0.283 \text{ lbs./in.}^3, \quad v = 0.30,$$
$$K = 0.886$$
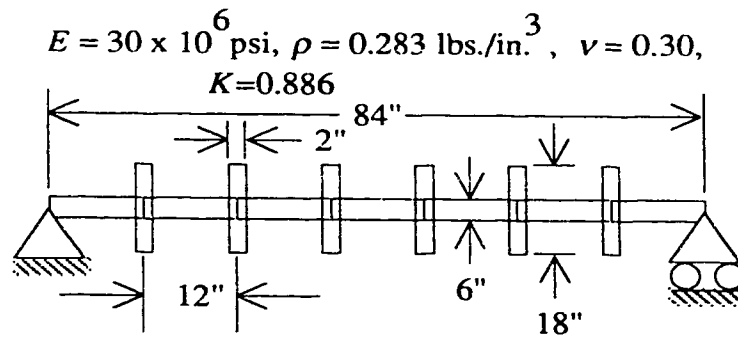


FIGURE 2.6: Turbine Model
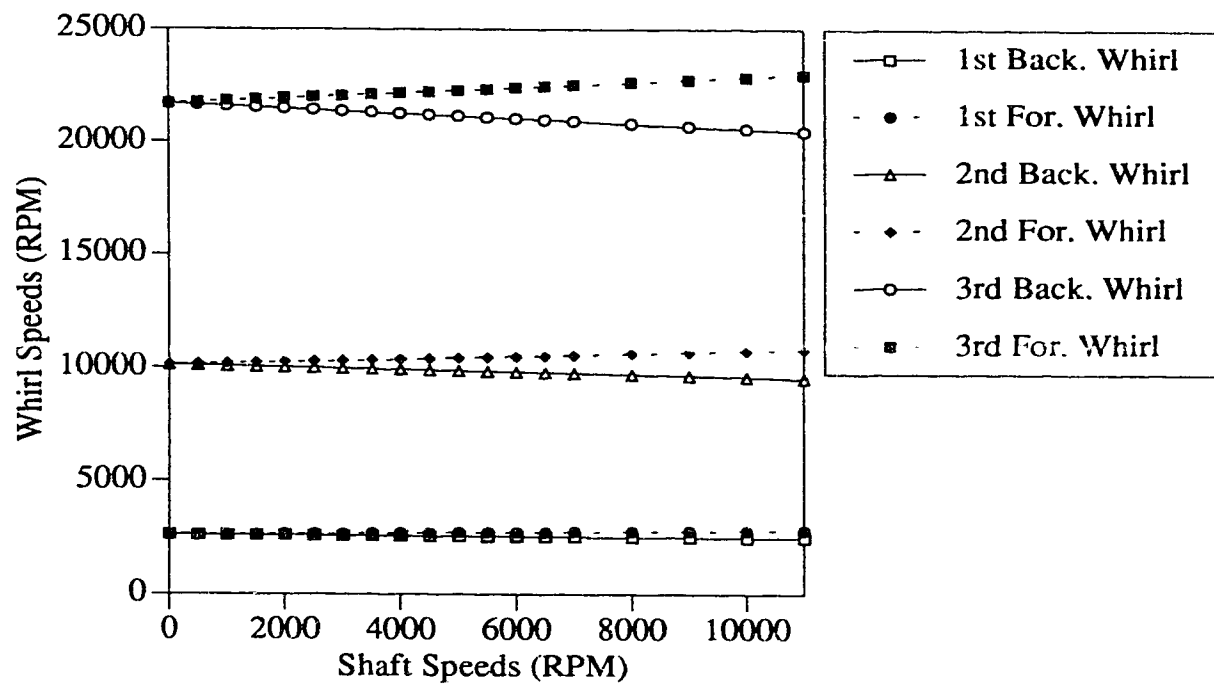


FIGURE 2.7: Turbine Whirl Speeds

# CHAPTER 3

# Axisymmetric Elements

*Much Ado About Nothing — Shakespeare*

## 3.1 Introduction

Traditionally, Euler-Bernoulli or Timoshenko beam theories have been used to formulate finite element models of rotor-bearing systems as discussed in Chap. 2. However, the elements so formed are restricted in accuracy: the primary assumption made in the theory of simple bending is that planes perpendicular to the neutral axis remain plane as the beam is bent. This works well when the structure being modelled is prismatic and of an uniform section over its length. When the structure, is however, tapered or constructed of a number of uniform sections, then the planar assumption is no longer valid. Consider the abrupt change of diameter illustrated in Fig. 3.1. As shown, it is modelled with a beam or shaft element that results in one node at the intersection of the two elements. The beam element unknowns only allow lateral translation and change in the slope (rotation of the cross-section) of the neutral axis. These conditions restrict both the small and larger cross-sectional areas to a planar rotation at the junction. However, some warping must occur at the junction. Also, beam finite element theory assumes that the stiffness increases abruptly at the change in section in proportion to $EI$. But, since there is warping

29
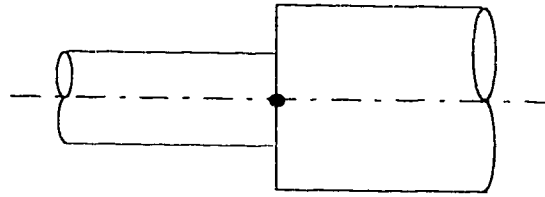
FIGURE 3.1: Abrupt Change of Beam Section
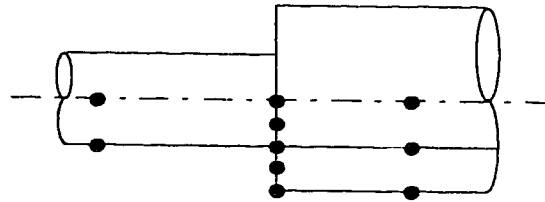


FIGURE 3.2: Abrupt Change in Section Modelled with Axisymmetric Elements

of the section, it can also be seen that material to the right of the section change cannot contribute fully to the bending stiffness of the beam. Indeed, considering the case from the perspective of elasticity, if the plane sections remained plane at a step change in section while undergoing bending, and if the stiffness also increased proportionally, then a surface traction over the annular area must exist. But since there is no distributed force over this surface, the plane assumption violates the boundary condition equations of elasticity. If the change in section is modelled with axisymmetric elements based on three-dimensional displacements, as shown in Fig. 3.2, then the junction has a number of nodes. Each node allows longitudinal, radial and circumferential displacement, and therefore the degrees of freedom at the intersection of the diameters allow the junction face to warp. As well, warping of the larger diameter face, which reduces the ability of the material to resist bending is modelled. In fact, the material at the outer radius of the large diameter face may almost be neglected when calculating actual bending stiffness of the junction.

Most shafts or rotors of real machines have many changes in section, and therefore the use of beam finite elements may be unsatisfactory when trying

to predict natural frequencies, and any further dynamic analysis may also be suspect. The primary modes of vibration in turbomachinery involve translational displacement of the shaft away from the axis of rotation, and include the effects of bending and shear. Therefore, a more satisfactory way of modelling the actual elastic dynamic response of the shaft itself is required. The first improvement over the beam-shaft type finite element was proposed by Geradin and Kill [15], and later tested by Stephenson, Rouch and Arora [16].

The Geradin and Kill element is an axisymmetric dynamic element based on full three-dimensional elasticity principles, and allows non-symmetric loads and displacements by using a Fourier series displacement and loading approximation. Since the element is axisymmetric, the nodes are actually nodal circles as shown in Fig. 3.3, and the element itself forms a symmetric torus about the shaft axis. The element has twelve nodal circles, but uses only the four nodal circles at the corners of the semimeridional plane to evaluate the element geometry, and is therefore a subparametric element. The semimeridional plane is a plane cut through the element in the radial direction, with the other axis of the plane being the shaft axis. An extension of the above element to a full isoparametric form is presented here (see Eckert and Craggs [17]); that is, all twelve nodal circles are used to define the undeformed geometry and subsequent deformation of the element section. This extension allows full continuity of all connected nodes, and also allows the modelling of elements of different sections. The Geradin and Kill axisymmetric element would only allow the semimeridional plane to be a quadrilateral section. The full isoparametric axisymmetric element allows the sides of the semimeridional plane to be curved, and therefore shaft sections that are barrel shaped in the direction of the axis, as well as uniform and tapered, can be modelled.

The element has been named axisymmetric in the published literature. Normally axisymmetric elements only allow axisymmetric displacement and loading. Because this element has an undeformed axisymmetric geometry, and is formulated to allow

non-symmetric loading and displacement, it is more properly referred to as a quasi-axisymmetric element. However, to maintain consistency with the literature, the element will be referred to as an axisymmetric element in this thesis.

## 3.2 Axisymmetric Beam Formulation

The axisymmetric element is pictured in Fig. 3.3. Each of the nodal lines has three displacements $u, v$, and $w$, which are respectively radial, axial and circumferential directions. The displacements can be expanded as a Fourier series in the circumferential direction using (see Eq. (3.1)) two-dimensional shape functions dependent on the radial and axial position (Zienkiewicz [18]). To allow bending, it is only necessary to consider the first harmonic of the Fourier expansion; that is, in Eq. (3.1) $n = 1$ with $m = 0$ for the symmetric plane of bending, and $m = 1$ for the antisymmetric plane. Using these values of $n$ and $m$, the displacements can then be rewritten as Eq. (3.2). The shape functions superscripted with 0 represent the displacements symmetric about the $r$-$z$ plane ($\theta = 0^\circ$), while those superscripted with 1 represent displacements symmetric about the $\theta = 90^\circ$ plane (antisymmetric about $\theta = 0^\circ$). The symmetric and antisymmetric displacements given by Eq. (3.2), are illustrated in Fig. 3.4. The bending that is described allows some warping of the shaft cross-section. Simple bending theory assumes that the cross-section remains plane during bending, and therefore the axisymmetric element is less constrained than beam-shaft elements. However, it must be noted that the allowed displacements result in each individual nodal circle remaining plane during bending. Relaxing the warping constraint further, so that individual nodal circles could also warp, would require the addition of higher order trigonometric terms to the Fourier series (i.e., $n > 1$), and the addition of nodal unknowns. The six nodal displacements used, allow the modelling of bending in two perpendicular transverse planes of a shaft element.
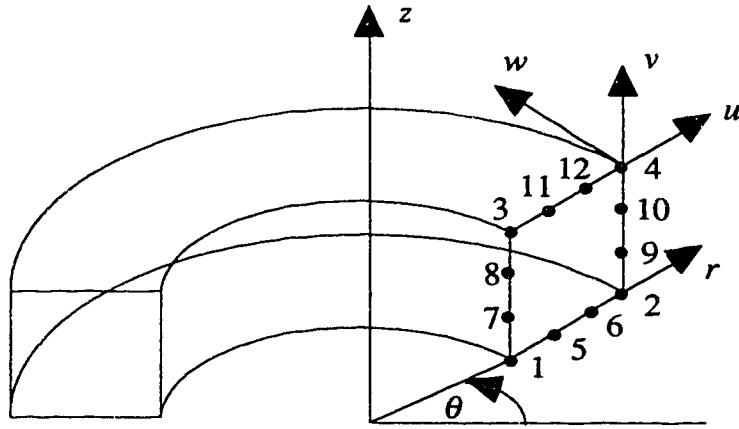
**FIGURE 3.3**: Global Coordinates

$$u = \sum_{n=0}^{\infty} \sum_{m=0}^{1} u^{n,m} \cos(n\theta + m\frac{\pi}{2})$$

$$v = \sum_{n=0}^{\infty} \sum_{m=0}^{1} v^{n,m} \cos(n\theta + m\frac{\pi}{2}) \qquad (3.1)$$

$$w = \sum_{n=0}^{\infty} \sum_{m=0}^{1} w^{n,m} \sin(n\theta + m\frac{\pi}{2})$$

$$u = u^0(r,z)\cos\theta + u^1(r,z)\sin\theta$$

$$v = v^0(r,z)\cos\theta + v^1(r,z)\sin\theta \qquad (3.2)$$

$$w = w^0(r,z)\sin\theta + w^1(r,z)\cos\theta$$

In this section, only bending in one plane will be considered, so that only the first term of each of Eq. (3.2) is needed. The two dimensional shape functions $(u^0(r,z)$ etc.) can be expanded into the sum of serendipity functions times the nodal displacements resulting in Eq. (3.3).

Symmetric
Displacements

Antisymmetric
Displacements

Radial Displacement

$u^0 \cos \theta$

$u^1 \sin \theta$

Tangential Displacement

$w^0 \sin \theta$

$w^1 \cos \theta$

Axial Displacement

$v^0 \cos \theta$

$v^1 \sin \theta$
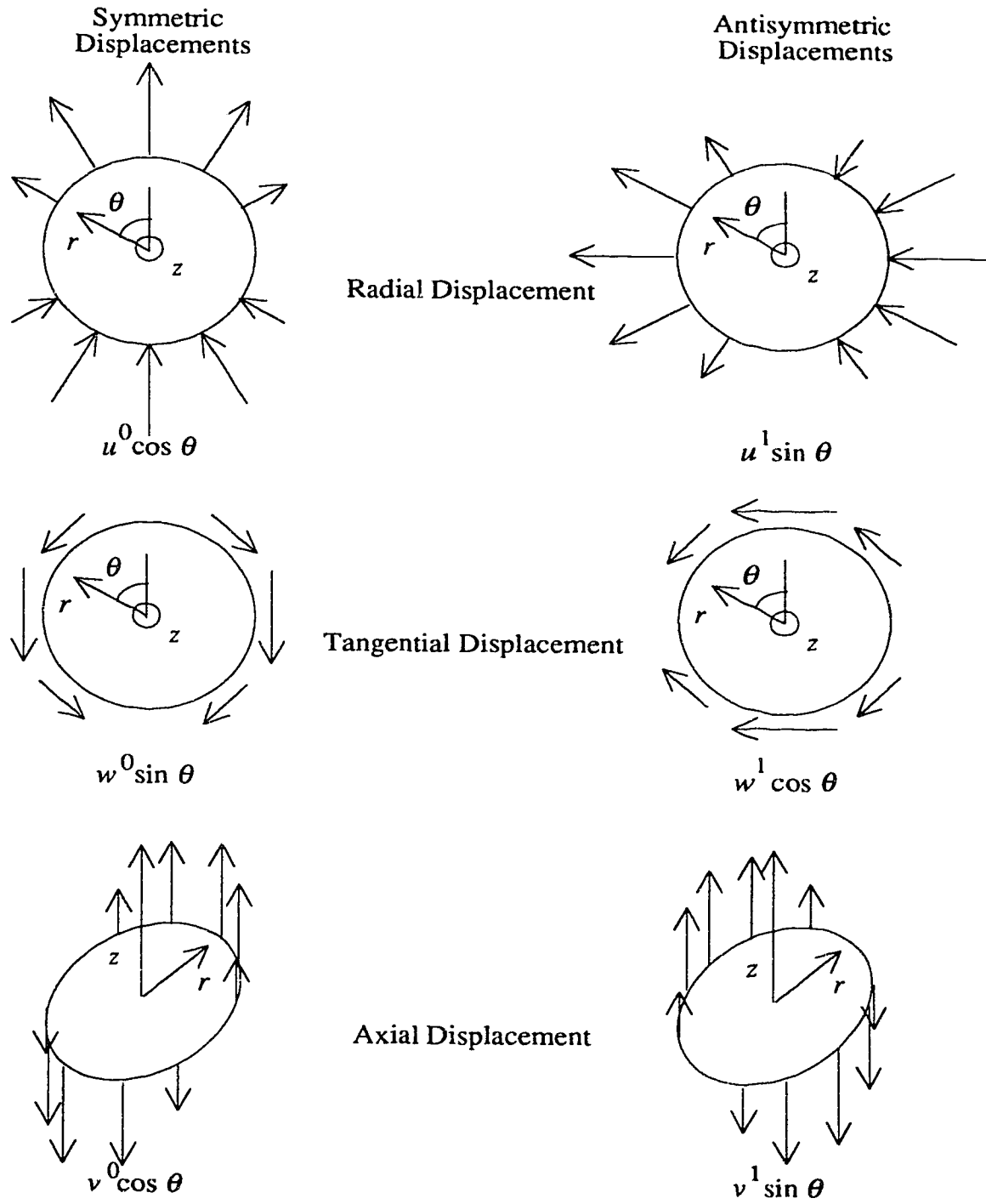
FIGURE 3.4: Nodal Displacements

$$u = \lfloor N \rfloor \{u_e^0\} \cos \theta$$
$$v = \lfloor N \rfloor \{v_e^0\} \cos \theta \qquad (3.3)$$
$$w = \lfloor N \rfloor \{w_e^0\} \sin \theta$$

The serendipity functions, $\lfloor N \rfloor$, are used instead of simple polynomials to eliminate the need for inversion. In actuality, the simple polynomials were evaluated and inverted once to explicitly form the serendipity functions, and with the derivation given in Appendix A.4.

Since the element is isoparametric, the radial and axial positions at any point in the element are defined with the same serendipity functions as the displacements resulting in Eq. (3.4).

$$r = \lfloor N \rfloor \{r_e\}$$
$$z = \lfloor N \rfloor \{z_e\} \qquad (3.4)$$

Forming the mass, stiffness and gyroscopic matrices for the axisymmetric element requires a numerical integration to be performed over the element volume. To facilitate the integration, the nodal coordinates are transformed from the global coordinate system shown in Fig. 3.3 to the local coordinate system shown in Fig. 3.5 (semimeridional plane shown only). This ensures that the semimeridional plane of any approximately quadrilateral shape can be easily integrated as a square shape.

The equation of motion of a single axisymmetric element can be found using Lagrange's equation:

$$\frac{d}{dt}[\frac{\partial \mathcal{L}}{\partial \dot{q}_i}] - \frac{\partial \mathcal{L}}{\partial q_i} = 0, \qquad (3.5)$$

where $\mathcal{L}$ is the Lagrangian, and is defined as the difference between kinetic and potential energy (i.e.: $\mathcal{L} = T - U$). The variable $q_i$ represents a general
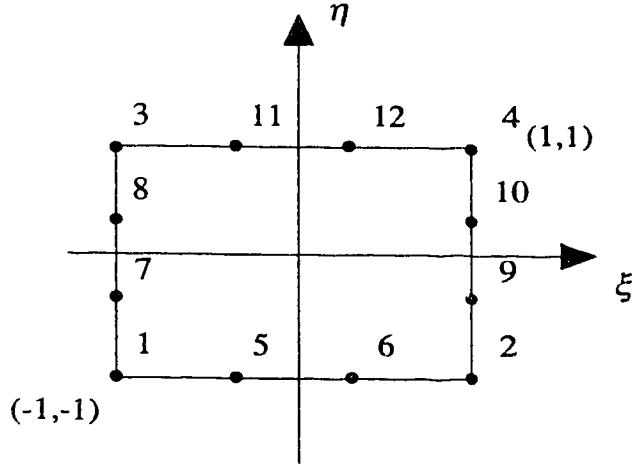
**FIGURE 3.5**: Local Coordinates

coordinate, and for this element the general coordinate vector is the vector of nodal displacements, $\{\delta_e\}$. The Lagrangian for the element can be expressed as:

$$\mathcal{L} = \frac{1}{2}\{\dot{\delta}_e\}^T[M_e]\{\dot{\delta}_e\} + \Omega\{\delta_e\}^T[G'_e]\{\dot{\delta}_e\} - \frac{1}{2}\{\delta_e\}^T[K_e]\{\delta_e\}, \tag{3.6}$$

where the first term is the kinetic energy due to translational velocities, the second term is the gyroscopic effect, and the last term is the potential energy due to the stored strain in the element. Substituting Eq. (3.6) into Lagrange's equation, Eq. (3.5), and completing the differentiation for all the coordinates results in:

$$\frac{d}{dt}([M_e]\{\dot{\delta}_e\} + \Omega[G'_e]^T\{\delta_e\}) - (\Omega[G'_e]\{\dot{\delta}_e\} - [K_e]\{\delta_e\}) = \{0\}, \tag{3.7}$$

or:

$$[M_e]\{\ddot{\delta}_e\} + \Omega([G'_e]^T - [G'_e])\{\dot{\delta}_e\} + [K_e]\{\delta_e\} = \{0\}. \tag{3.8}$$

The above equation of motion includes the gyroscopic effect, which is examined in detail in section 3.3. The following subsections give the derivation of the stiffness and mass matrices, and then compare the results of the non-rotating axisymmetric element to a beam element.

### 3.2.1 Stiffness Matrix

To find the stiffness matrix, the potential or strain energy must be expressed in the same form as in the Lagrangian, Eq. (3.6). The strain energy for a volume of material, where $dvol = r\,dr\,dz\,d\theta$ in the cylindrical coordinate system, may be written as:

$$\text{Strain Energy} = \frac{1}{2} \int \int \int \{\epsilon\}^T \{\sigma\} \, dvol. \qquad (3.9)$$

The strain vector for the cylindrical coordinate system is:

$$\{\epsilon\} = \left\{ \begin{array}{c} \frac{\partial u}{\partial r} \\ \frac{\partial v}{\partial z} \\ (\frac{u}{r} + \frac{1}{r}\frac{\partial w}{\partial \theta}) \\ (\frac{\partial u}{\partial z} + \frac{\partial v}{\partial r}) \\ (\frac{1}{r}\frac{\partial u}{\partial \theta} + \frac{\partial w}{\partial r} - \frac{w}{r}) \\ (\frac{1}{r}\frac{\partial v}{\partial \theta} + \frac{\partial w}{\partial z}) \end{array} \right\}, \qquad (3.10)$$

and, the stress vector is given by:

$$\{\sigma\} = [D]\{\epsilon\} = \begin{Bmatrix} \sigma_{rr} \\ \sigma_{zz} \\ \sigma_{\theta\theta} \\ \sigma_{rz} \\ \sigma_{r\theta} \\ \sigma_{z\theta} \end{Bmatrix} . \tag{3.11}$$

The matrix, $[D]$, is the elasticity or Hooke matrix and is defined as:

$$[D] = \frac{E(1 - \nu)}{(1 + \nu)(1 - 2\nu)} \begin{bmatrix} 1 & \frac{\nu}{(1-\nu)} & \frac{\nu}{(1-\nu)} & 0 & 0 & 0 \\ \frac{\nu}{(1-\nu)} & 1 & \frac{\nu}{(1-\nu)} & 0 & 0 & 0 \\ \frac{\nu}{(1-\nu)} & \frac{\nu}{(1-\nu)} & 1 & 0 & 0 & 0 \\ 0 & 0 & 0 & \frac{1-2\nu}{2(1-\nu)} & 0 & 0 \\ 0 & 0 & 0 & 0 & \frac{1-2\nu}{2(1-\nu)} & 0 \\ 0 & 0 & 0 & 0 & 0 & \frac{1-2\nu}{2(1-\nu)} \end{bmatrix} . \tag{3.12}$$

Using equations (3.10), (3.11), and (3.12) the strain energy can now be written in the matrix form:

$$\text{Strain Energy} = \frac{1}{2} \int \int \int \{\epsilon\}^T [D] \{\epsilon\} r \, dr \, dz \, d\theta. \tag{3.13}$$

However, to derive the stiffness matrix, the strain energy must be expressed in terms of the nodal unknowns. Using the general expressions for the displacements, Eq. (3.3), the strain vector can be rewritten as:

$$\{\epsilon\} = [B] \begin{Bmatrix} \{u_e^0\} \\ \{v_e^0\} \\ \{w_e^0\} \end{Bmatrix} = [B]\{\delta_e^0\}, \tag{3.14}$$

where $\{\delta_e^0\}$ represents the symmetric nodal displacement vector, and $[B]$ is the matrix given below:

$$[B] = \begin{bmatrix} \lfloor N_r \rfloor \cos\theta & 0 & 0 \\ 0 & \lfloor N_z \rfloor \cos\theta & 0 \\ \frac{1}{r}\lfloor N \rfloor \cos\theta & 0 & \frac{1}{r}\lfloor N \rfloor \cos\theta \\ \lfloor N_z \rfloor \cos\theta & \lfloor N_r \rfloor \cos\theta & 0 \\ -\frac{1}{r}\lfloor N \rfloor \sin\theta & 0 & (\lfloor N_r \rfloor - \frac{1}{r}\lfloor N \rfloor)\sin\theta \\ 0 & -\frac{1}{r}\lfloor N \rfloor \sin\theta & \lfloor N_z \rfloor \sin\theta \end{bmatrix} . \qquad (3.15)$$

The subscripts $r$ and $z$ represent the partial differentiation of the variable with respect to the radial and axial coordinates as required by the strain vector.

Using the Jacobian matrix, $[J]$ given by Eq. (3.16), the coordinates are transformed from the $r, z, \theta$ coordinates of the global system to the $\xi, \eta, \theta$ coordinates of the local system. This also transforms the semimeridional area of arbitrary shape to the square area centered on the origin. After transformation, the strain energy is given by Eq. (3.18), where the limits of integration due to the transformation are $-1$ and $1$ for both the $\xi$ and $\eta$ ($r$ and $z$) directions.

$$[J] = \begin{bmatrix} \frac{\partial r}{\partial \xi} & \frac{\partial z}{\partial \xi} \\ \frac{\partial r}{\partial \eta} & \frac{\partial z}{\partial \eta} \end{bmatrix} \qquad (3.16)$$

$$\left\{ \begin{array}{c} \frac{\partial}{\partial r} \\ \frac{\partial}{\partial z} \end{array} \right\} = [J]^{-1} \left\{ \begin{array}{c} \frac{\partial}{\partial \xi} \\ \frac{\partial}{\partial \eta} \end{array} \right\} \qquad (3.17)$$

$$\text{Strain Energy} = \frac{1}{2}\{\delta_e^0\}^T \left( \int_0^{2\pi} \int_{-1}^{1} \int_{-1}^{1} r\,[B']^T\,[D]\,[B']\,\|J\|\,d\xi\,d\eta\,d\theta \right) \{\delta_e^0\} \qquad (3.18)$$

The strain energy equation is now in terms of the nodal displacements of the element, as was done in the Lagrangian (Eq. (3.6)). Therefore, the portion of the expression inside the brackets is the stiffness matrix. It should be noted, that $[B']$ is matrix $[B]$ of Eq. (3.15) transformed by Eq. (3.17) to the local coordinate ... tem, and is dependent on $\theta$. However, when the matrix multiplication in Eq. (3.18) is carried out, all non-zero terms contain either a $\cos^2 \theta$ or $\sin^2 \theta$, and since $\int_0^{2\pi} \cos^2 \theta \, d\theta = \int_0^{2\pi} \sin^2 \theta \, d\theta = \pi$, the integration in the circumferential direction may be completed by merely multiplying by $\pi$. The stiffness matrix as extracted from Eq. (3.18) is:

$$[K_e] = \pi \int_{-1}^{1} \int_{-1}^{1} r(\xi, \eta) \, [B''(\xi, \eta)]^T \, [D] \, [B''(\xi, \eta)] \, \|J(\xi, \eta)\| \, d\xi \, d\eta, \qquad (3.19)$$

where $[B'']$ is now the matrix $[B']$ from Eq. (3.18) with the trigonometric terms explicitly integrated out of the matrix.

Evaluating Eq. (3.19) using Gauss quadrature results in:

$$[K_e] = \pi \sum_{i=1}^{n_\xi} \sum_{j=1}^{n_\eta} w_i \, w_j \, r(\xi_i, \eta_j) \, [B''(\xi_i, \eta_j)]^T \, [D] \, [B''(\xi_i, \eta_j)] \, \|J(\xi_i, \eta_j)\|, \qquad (3.20)$$

where $n_\xi$, $n_\eta$, and $w_i$, $w_j$ are the number of points, and weighting factors for Gauss quadrature in the $\xi$ and $\eta$ directions respectively. The Gauss quadrature used four integration points in each of the $\xi$ and $\eta$ directions.

## 3.2.2 Mass Matrix

The translational kinetic energy of an infinitesimal element of material is given by:

The strain energy equation is now in terms of the nodal displacements of the element, as was done in the Lagrangian (Eq. (3.6)). Therefore, the portion of the expression inside the brackets is the stiffness matrix. It should be noted, that $[B']$ is matrix $[B]$ of Eq. (3.15) transformed by Eq. (3.17) to the local coordinate system, and is dependent on $\theta$. However, when the matrix multiplication in Eq. (3.18) is carried out, all non-zero terms contain either a $\cos^2 \theta$ or $\sin^2 \theta$, and since $\int_0^{2\pi} \cos^2 \theta \, d\theta = \int_0^{2\pi} \sin^2 \theta \, d\theta = \pi$, the integration in the circumferential direction may be completed by merely multiplying by $\pi$. The stiffness matrix as extracted from Eq. (3.18) is:

$$[K_e] = \pi \int_{-1}^{1} \int_{-1}^{1} r(\xi, \eta) \, [B''(\xi, \eta)]^T \, [D] \, [B''(\xi, \eta)] \, \|J(\xi, \eta)\| \, d\xi \, d\eta, \qquad (3.19)$$

where $[B'']$ is now the matrix $[B']$ from Eq. (3.18) with the trigonometric terms explicitly integrated out of the matrix.

Evaluating Eq. (3.19) using Gauss quadrature results in:

$$[K_e] = \pi \sum_{i=1}^{n_\xi} \sum_{j=1}^{n_\eta} w_i \, w_j \, r(\xi_i, \eta_j) \, [B''(\xi_i, \eta_j)]^T \, [D] \, [B''(\xi_i, \eta_j)] \, \|J(\xi_i, \eta_j)\|, \qquad (3.20)$$

where $n_\xi$, $n_\eta$, and $w_i$, $w_j$ are the number of points, and weighting factors for Gauss quadrature in the $\xi$ and $\eta$ directions respectively. The Gauss quadrature used four integration points in each of the $\xi$ and $\eta$ directions.

### 3.2.2 Mass Matrix

The translational kinetic energy of an infinitesimal element of material is given by:

$$dT_{\text{trans}} = \frac{1}{2}\rho \left\{ \begin{array}{c} \dot{u} \\ \dot{v} \\ \dot{w} \end{array} \right\}^T \left\{ \begin{array}{c} \dot{u} \\ \dot{v} \\ \dot{w} \end{array} \right\} dvol. \tag{3.21}$$

But the translational velocities may be written in terms of nodal displacements using Eq. (3.3). Note again, that only the symmetric components are being used here. I.e.:

$$\left\{ \begin{array}{c} \dot{u} \\ \dot{v} \\ \dot{w} \end{array} \right\} = [A]\{\dot{\delta}_e^0\}, \tag{3.22}$$

where:

$$[A] = \begin{bmatrix} \lfloor N \rfloor \cos\theta & 0 & 0 \\ 0 & \lfloor N \rfloor \cos\theta & 0 \\ 0 & 0 & \lfloor N \rfloor \sin\theta \end{bmatrix}. \tag{3.23}$$

Therefore, the total kinetic energy stored in an axisymmetric element of material undergoing translation of the nodal circles may be written as:

$$T_{\text{trans}} = \frac{1}{2}\{\dot{\delta}_e^0\}^T \left( \int_0^{2\pi} \int_z \int_r r\rho[A]^T[A]\, dr\, dz\, d\theta \right) \{\dot{\delta}_e^0\}. \tag{3.24}$$

Since the translational kinetic energy is now expressed in the same form as the Lagrangian, the portion of the triple integral that is in the brackets is the mass matrix for the element. Again, the only non-zero terms in the resultant of the matrix multiplication contains squared trigonometric terms that can be integrated

separately. After transforming the coordinate system to the local system using (3.16) and (3.17), the mass matrix may be expressed as:

$$[M_e] = \pi\rho \int_{-1}^{1} \int_{-1}^{1} r(\xi,\eta)\,[A'(\xi,\eta)]^T\,[A'(\xi,\eta)]\,\|J(\xi,\eta)\|\,d\xi\,d\eta. \qquad (3.25)$$

Evaluating Eq. (3.25) using Gauss quadrature gives:

$$[M_e] = \pi\rho \sum_{i=1}^{n_\xi} \sum_{j=1}^{n_\eta} w_i\,w_j\,r(\xi_i,\eta_j)\,[A'(\xi_i,\eta_j)]^T\,[A'(\xi_i,\eta_j)]\,\|J(\xi_i,\eta_j)\|, \qquad (3.26)$$

where $n_\xi$, $n_\eta$, and $w_i$, $w_j$ are the number of points, and the weighting factors for Gauss quadrature in the $\xi$ and $\eta$ directions respectively. The mass matrix was also evaluated using four integration points for each of the $\xi$ and $\eta$ directions. The matrix, $[A']$, is given by Eq. (3.23) where the trigonometric terms have been integrated out, and the coordinate system transformed.

## 3.2.3 Beam Type Results

Before the element can be used to model beam behaviour two further steps must be performed. First, at nodes that are on the axis of symmetry and therefore have a radius of zero, the strain components containing $1/r$ terms will have an infinite magnitude. The treatment for this condition is given later under the full shaft formulation in Section 3.3.3. The same treatment can be applied to a bending behaviour in one plane by applying it to only the in-plane degrees of freedom. Second, the typical beam boundary conditions of clamped and pinned ends can be applied by introducing large stiffnesses at the appropriate in-plane degrees of freedom as also discussed under the full shaft formulation in Section 3.3.2. At a clamped end all the nodal degrees of freedom can be constrained, and at a pinned end the radial displacement of the innermost node is constrained. When bending in

one plane is considered, any cross-coupling stiffnesses between planes, as presented in Section 3.3.2 can also be ignored.

The first test of the axisymmetric element is how well it models beam type behaviour. The uniform simply supported beam as shown in Fig. 3.6, was modelled with both the axisymmetric isoparametric element derived in this chapter and with the Timoshenko beam element discussed in Chap. 2. The natural frequencies for both models and those calculated using the series solution to the Timoshenko equations by Anderson [6] (exact) are compared in Table 3.1, and it can be seen that the axisymmetric element does indeed model simply beam behaviour correctly. The error was calculated based on the exact Timoshenko (Anderson) values. Both finite element models had approximately 150 degrees of freedom for this test. The Timoshenko beam element model gave natural frequencies that were within 0.05% of the exact solution of the Timoshenko equations. The axisymmetric element gave results that were within 2% of the exact solution, but were all lower than that solution. The exact solution and the Timoshenko beam element are both based on beam theory, while the axisymmetric element allows displacements that are not accounted for in beam theory. The Timoshenko solutions are effectively constrained more in comparison to the axisymmetric model, and it is therefore reasonable for the axisymmetric natural frequencies to be lower than those predicted by Timoshenko beam theory.

The elements were also compared by modelling a simply supported beam with a taper and a step in depth as shown in Fig. 3.7. In this particular case, the Timoshenko element was a tapered element with constant shear angle along the element length. The results of the two are given in Table 3.2. Here, the percentage difference calculated was based on the axisymmetric model being correct. For the Timoshenko beam model, the first and third natural frequencies were slightly higher than those calculated with the axisymmetric element. Considering the mode shapes for these frequencies, it can be seen that the first and third modes had a greater

$E = 30 \times 10^6$ psi., $\rho = 0.283$ lbs./in.$^3$, $v = 0.287$, $K$=0.885
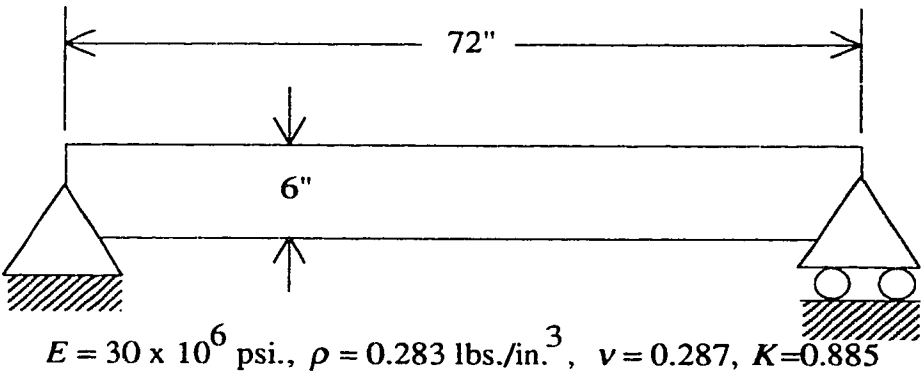
**FIGURE 3.6**: Uniform Simply Supported Beam

**TABLE 3.1**: Natural Frequencies (CPM) of Simply Supported Uniform Beam

| Mode | Exact | Timo. | Error (%) | Axisym. | Error (%) |
|------|-------|-------|-----------|---------|-----------|
| 1 | 5473 | 5474 | 0.02 | 5465 | -0.15 |
| 2 | 21375 | 21378 | 0.01 | 21257 | -0.55 |
| 3 | 46356 | 46368 | 0.03 | 45844 | -1.10 |
| 4 | 78692 | 78730 | 0.05 | 77334 | -1.73 |

$E = 30 \times 10^6$ psi., $\rho = 0.283$ lbs./in.$^3$, $\nu = 0.287$, $K = 0.885$
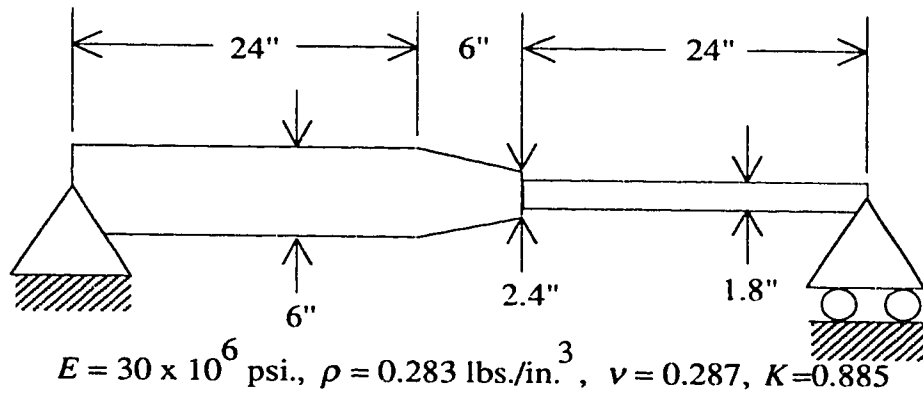
**FIGURE 3.7**: Tapered and Stepped Simply Supported Beam

**TABLE 3.2**: Natural Frequencies (CPM) of Simply Supported Tapered Beam

| Mode | Timoshenko | Axisymmetric | Difference (%) |
|------|------------|--------------|----------------|
| 1 | 2238 | 2230 | 0.4 |
| 2 | 22263 | 22268 | -0.02 |
| 3 | 50800 | 49820 | 2.0 |
| 4 | 74416 | 79497 | -6.4 |

change in bending slope along the middle length of the beam than the second mode. That is, a greater portion of the strain energy was being stored in the beam in the middle section while undergoing bending. Since that length has the taper and step, where the beam theory assumption of perpendicular planes remaining plane does not hold true, the Timoshenko beam model exhibited the greatest percentage difference for those modes. The second and fourth natural frequencies of the Timoshenko model were lower than those of the axisymmetric element. This is because the larger diameter section and taper of the beam were very stiff in bending, and as a result, the shear deformation dominated the bending deformation, giving lower natural frequencies.

A simply supported beam with an abrupt change in section depth at mid-span was also modelled (see Fig. 3.8). The natural frequencies were calculated using the Timoshenko element and the axisymmetric element for values of $D_2/D_1$ ranging from 1 (uniform beam) to 2. Note, that an abrupt change of diameter to twice the diameter implies an abrupt change in section stiffness of 16 times the base stiffness (for circular cross-sections) when using simple beam theory. Figures 3.9 and 3.10 compare the first and second natural frequencies of the models. The first frequency calculated with the axisymmetric element was slightly higher than predicted by the Timoshenko model, when the beam was uniform ($D_2/D_1 = 1$). As the step ratio was increased to 2, the axisymmetric model predicted a slightly lower fundamental frequency, implying that not all of the material was effective in resisting bending. Again, the larger error exhibited in the first natural frequency was due to the larger strain energy (change in bending angle) across the abrupt change in section diameter. This is consistent with previous work by Sanderson and Kitching [2] which shows that some of the added section thickness at the diameter change has no actual effect on the stiffness of the beam in static bending. As well, the first natural frequency peaks at a diameter ratio of about 1.3, and then falls. The natural frequency increases for $1 \leq D_2/D_1 \leq 1.3$ because increasing the diameter, $D_2$, increases the stiffness of the beam more than the mass is increased. When $1.3 < D_2/D_1 \leq 2.0$ the right hand end of the beam has become so stiff, that very little bending can occur in that portion. The increased diameter merely added mass and diametral moment of inertia to the end of the smaller diameter section, resulting in a natural frequency that dropped as the diameter increased. The second frequency calculated with the axisymmetric model was consistently higher than that predicted by the Timoshenko model.

The two different element types were also tested for bending of a hollow cantilever beam with an internal abrupt change in section diameter, as shown in Fig. 3.11. The small diameter $D_1$ was varied so that the ratio $D_2/D_1$ ranged from 1

$$E = 30 \times 10^6 \text{ psi.,} \quad \rho = 0.283 \text{ lbs./in.}^3, \quad \nu = 0.287, \quad K = 0.885$$
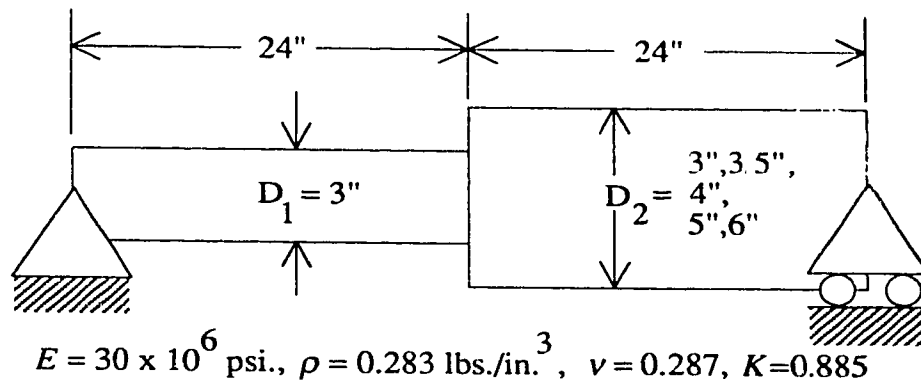
**FIGURE 3.8**: Simply Supported Beam, With Varying Step of Section

to 2. See Figures 3.12 and 3.13 for a comparison of the first two natural frequencies. For both the first and second modes, the axisymmetric and Timoshenko models predicted essentially the same natural frequencies, as the step ratio was varied.

## 3.3 Axisymmetric Shaft Element

The previous section dealt with a formulation of the axisymmetric element that only allowed bending in one plane. The element was restricted to essentially only beam type behaviour, but the elastic formulation allowed warping of the cross-section during bending. This section develops and tests the axisymmetric element as a full shaft model. That is, the element allows bending in two perpendicular planes, and accounts for the full gyroscopic effect of a spinning shaft on whirl speeds.

The isoparametric axisymmetric shaft element was tested on a simple overhung shaft with a disk, and the calculated whirl speeds are compared to those calculated with a Timoshenko shaft element. The axisymmetric shaft element was also tested on the Nelson and McVaugh rotor [19], and a comparison of the whirl speeds with those calculated using a Timoshenko shaft model, and those published by Nelson is given below.
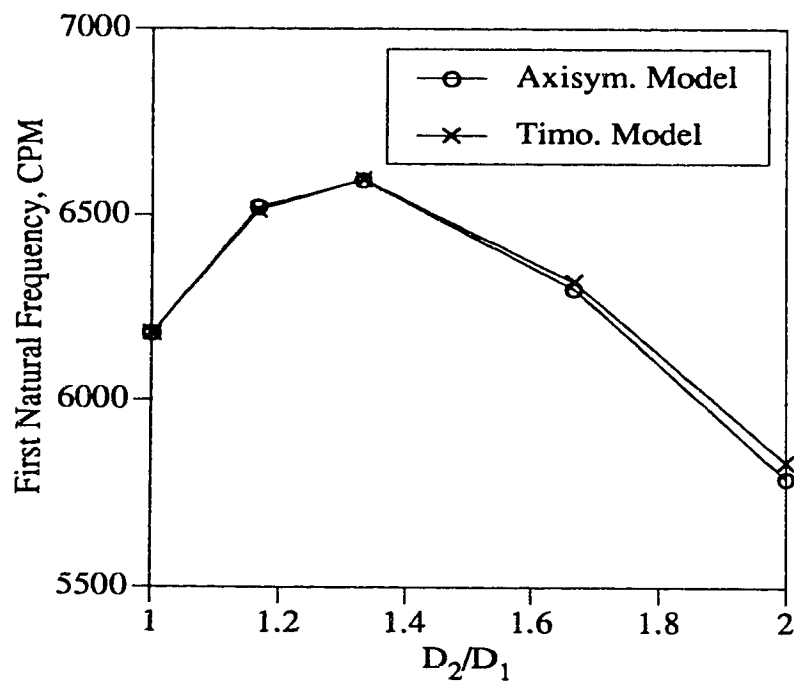
**FIGURE 3.9**: First Natural Frequency, Simply Supported Step
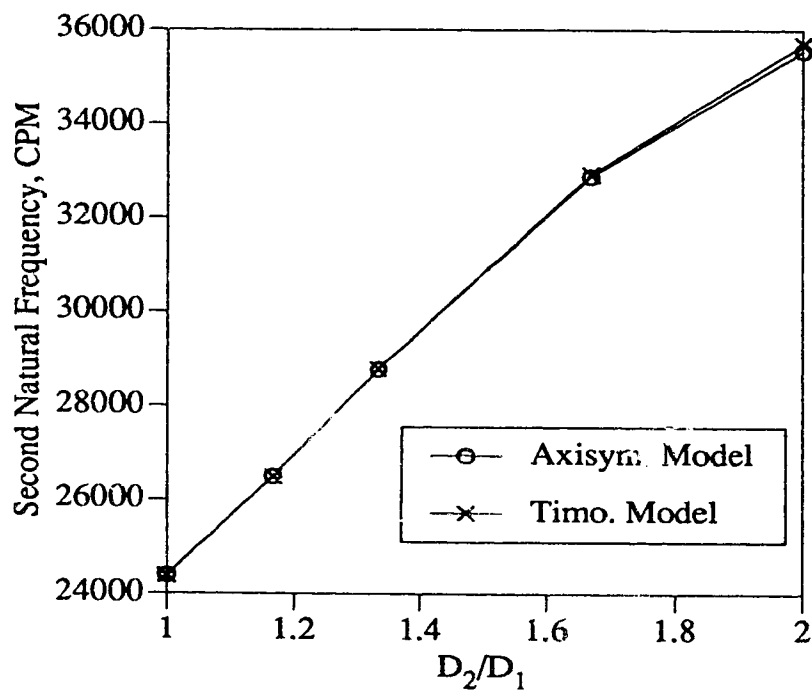


**FIGURE 3.10**: Second Natural Frequency, Simply Supported Step

$E = 30 \times 10^6$ psi., $\rho = 0.283$ lbs./in.$^3$, $\nu = 0.287$, $K = 0.885$
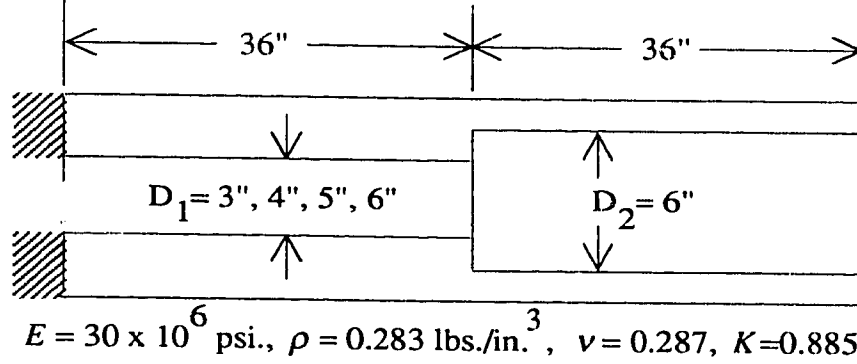
**FIGURE 3.11**: Hollow Cantilevered Beam, With Stepped Section

### 3.3.1 Shaft Element Formulation

To allow bending in two perpendicular planes, the generalized displacements $u$, $v$, and $w$ must be given by Eq. (3.2), where the displacement superscripted with 0 and 1 represents the contribution to the displacement from each of the bending planes (symmetric and antisymmetric to $\theta = 0°$). First consider the kinetic energy of an infinitesimal element of mass in an inertial cartesian coordinate system $x_i y_i z_i$. The kinetic energy is then:

$$T = \int_{vol} \left( v_x^2 + v_y^2 + v_z^2 \right) \rho \, dvol. \qquad (3.27)$$

Geradin and Kill [15] performed the following steps to calculate the gyroscopic portion of the kinetic energy in the axisymmetric coordinate system. Assume that the deformation of a point is given by $u_i$, $v_i$, and $w_i$ in the inertial cartesian coordinate system. Let there be a deformed cartesian coordinate system that can be derived from the inertial system by; a small rotation $\theta_i$ about the $y$-axis; small rotation $\psi_i$ about the $x_i$-axis; and a rotation of $\omega t$ about the shaft axis, the $z$-axis. The velocity can then be expressed in terms of the inertial velocity and position components, but using the deformed unit vectors. Substituting this expression into
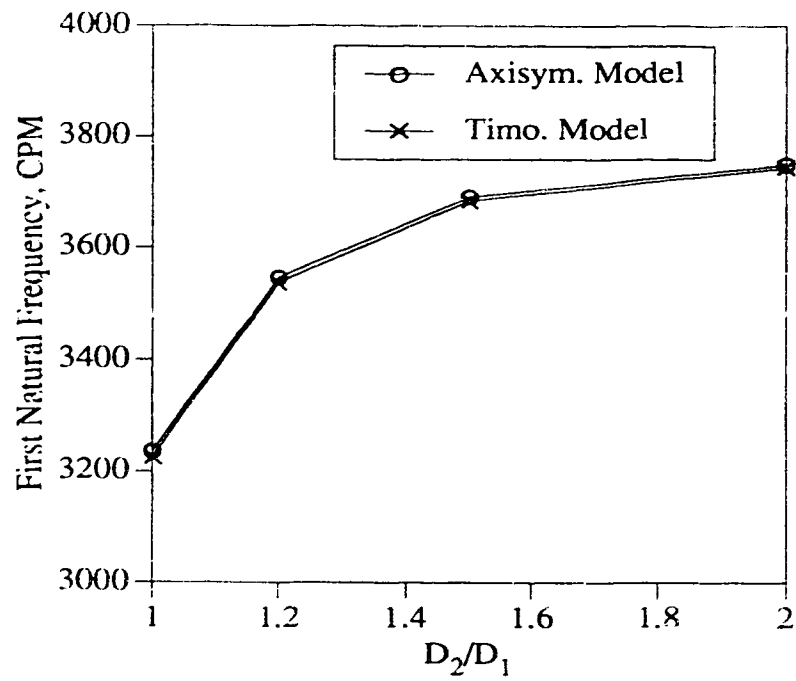
**FIGURE 3.12**: First Natural Frequency, Cantilevered Step
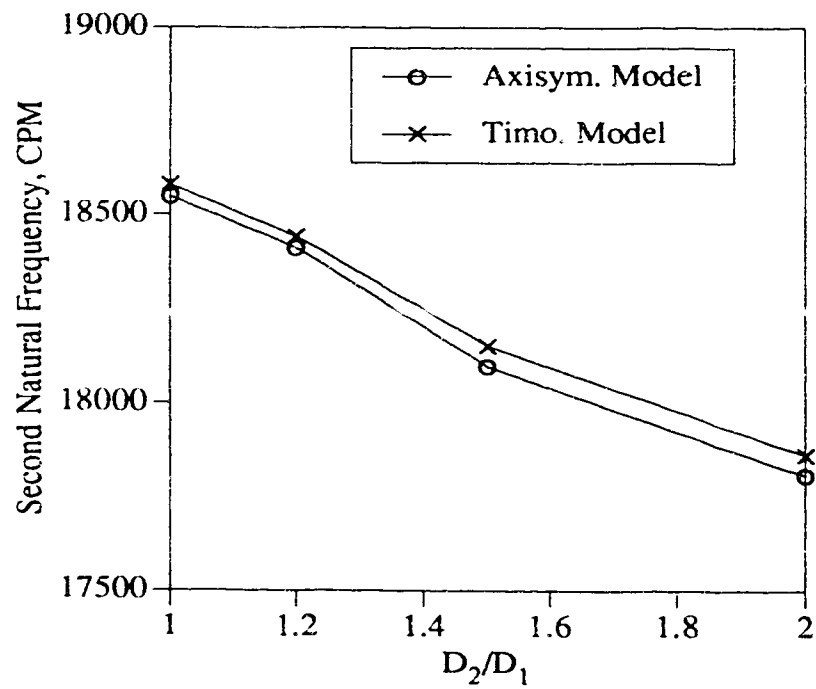


**FIGURE 3.13**: Second Natural Frequency, Cantilevered Step

the kinetic energy expression Eq. (3.27), and extracting the portion resulting in inertial effects gives:

$$T = -\Omega \int_{vol} w_i \left( \dot{\theta}_i y_i + \dot{v}_i x_i \right) \rho \, dvol. \tag{3.28}$$

The inertial position components may be related to the axisymmetric components by:

$$
\begin{aligned}
x_i &= r \cos \theta \\
y_i &= r \sin \theta \\
z_i &= z.
\end{aligned}
\tag{3.29}
$$

And, the displacements can be related by:

$$
\begin{aligned}
u_i &= u \cos \theta - w \sin \theta \\
v_i &= u \sin \theta - w \cos \theta \\
w_i &= v \\
\theta_i &= \Phi_r \cos \theta + \Phi_\theta \sin \theta \\
v_i &= -\Phi_r \sin \theta + \Phi_\theta \cos \theta.
\end{aligned}
\tag{3.30}
$$

As well:

$$\Phi_r = \frac{\partial u}{\partial z} \qquad \Phi_\theta = -\frac{\partial w}{\partial z}. \tag{3.31}$$

Substituting Eq. (3.29), Eq. (3.30) and Eq. (3.31) into Eq. (3.28) gives the following kinetic energy:

$$T = \frac{1}{2} \int_{vol} \left( \dot{u}^2 + \dot{v}^2 + \dot{w}^2 \right) \rho \, dvol - \Omega \int_{vol} v \dot{\Phi}_\theta \, \rho \, dvol. \tag{3.32}$$

The gyroscopic portion of the kinetic energy is the second term of the right hand side of Eq. (3.32). Rewriting the second term by substituting $\dot{\Phi}_\theta = \frac{\partial \dot{w}}{\partial z}$ results in the kinetic energy due to the gyroscopic effects of an axisymmetric shaft section Eq. (3.33).

$$T_{\text{gyro}} = -\Omega \int \int \int v \frac{d}{dt}(-\frac{\partial w}{\partial z})r\rho \, dvol \tag{3.33}$$

The displacements, $v$ and $w$, are given by the expressions Eq. (3.2), and the symmetric and antisymmetric components are given by:

$$u^0 = \{N\}^T\{u_e^0\} \qquad u^1 = \{N\}^T\{u_e^1\}$$

$$v^0 = \{N\}^T\{v_e^0\} \qquad v^1 = \{N\}^T\{v_e^1\} \tag{3.34}$$

$$w^0 = \{N\}^T\{w_e^0\} \qquad w^1 = -\{N\}^T\{w_e^1\}.$$

Note that the antisymmetric component of the axial displacement is defined as the negative sum of the serendipity functions times the antisymmetric axial displacements. This allows both the symmetric and antisymmetric portions of the stiffness and mass matrices to be the same, simplifying the computational effort.

The displacement in the axial and tangential directions can be written as:

$$v = \left\{\begin{array}{c} \{u_e^0\} \\ \{v_e^0\} \\ \{w_e^0\} \\ \{u_e^1\} \\ \{v_e^1\} \\ \{w_e^1\} \end{array}\right\}^T \left\{\begin{array}{c} 0 \\ \lfloor N \rfloor \cos\theta \\ 0 \\ 0 \\ \lfloor N \rfloor \sin\theta \\ 0 \end{array}\right\} = \{\delta_e\}^T\{A\}. \tag{3.35}$$

$$
w = \left\{ \begin{array}{c} 0 \\ 0 \\ \{N\}\sin\theta \\ 0 \\ 0 \\ -\{N\}\cos\theta \end{array} \right\}^{T} \left\{ \begin{array}{c} \{u_e^0\} \\ \{v_e^0\} \\ \{w_e^0\} \\ \{u_e^1\} \\ \{v_e^1\} \\ \{w_e^1\} \end{array} \right\}. \tag{3.36}
$$

Differentiating $w$ with respect to both $z$ and $t$ results in:

$$
\frac{d}{dt}\left(-\frac{\partial w}{\partial z}\right) = \left\{ \begin{array}{c} 0 \\ 0 \\ \{N_z\}\sin\theta \\ 0 \\ 0 \\ -\{N_z\}\cos\theta \end{array} \right\}^{T} \left\{ \begin{array}{c} \{\dot{u}_e^0\} \\ \{\dot{v}_e^0\} \\ \{\dot{w}_e^0\} \\ \{\dot{u}_e^1\} \\ \{\dot{v}_e^1\} \\ \{\dot{w}_e^1\} \end{array} \right\} = \{B\}^{T}\{\dot{\delta}_e\}. \tag{3.37}
$$

where:

$$
\{\delta_e\} = \left\{ \begin{array}{c} \{u_e^0\} \\ \{v_e^0\} \\ \{w_e^0\} \\ \{u_e^1\} \\ \{v_e^1\} \\ \{w_e^1\} \end{array} \right\}. \tag{3.38}
$$

Substituting Eq. (3.36) and Eq. (3.37) into Eq. (3.33) results in:

$$
T_{\text{gyro}} = \Omega\{\delta_e\}^{T}\left(\int\int\int r\rho\,\{A\}\{B\}^{T}\,dvol\right)\{\dot{\delta}_e\}. \tag{3.39}
$$

The portion of the Eq. (3.39) in brackets is the matrix $[G'_e]$, which is the gyroscopic portion of the Lagrangian defined by Eq. (3.6). Note that forming the product $\{A\}\{B\}^T$ results in all non-zero elements of the matrix having trigonometric terms. Since $\int_0^{2\pi} \cos^2\theta\, d\theta = \int_0^{2\pi} \sin^2\theta\, d\theta = \pi$, and $\int_0^{2\pi} \cos\theta \sin\theta\, d\theta = 0$, the full gyroscopic matrix $[G_e] = \Omega([G'_e]^T - [G'_e])$, in the equation of motion, Eq. (3.8), is given by:

$$[G_e] = \Omega\pi \int_z \int_r r^2 \rho\, [g(r,z)]\, dr\, dz, \tag{3.40}$$

where:

$$[g(r,z)] = \begin{bmatrix} 0 & 0 & 0 & 0 & 0 & 0 \\ 0 & 0 & 0 & 0 & 0 & \{N\}\lfloor N_z\rfloor \\ 0 & 0 & 0 & 0 & \{N_z\}\lfloor N\rfloor & 0 \\ 0 & 0 & 0 & 0 & 0 & 0 \\ 0 & 0 & -\{N\}\lfloor N_z\rfloor & 0 & 0 & 0 \\ 0 & -\{N_z\}\lfloor N\rfloor & 0 & 0 & 0 & 0 \end{bmatrix}. \tag{3.41}$$

The subscript $z$ represents differentiation with respect to the axial coordinate.

The gyroscopic matrix for the isoparametric axisymmetric element after transforming the coordinate system is:

$$[G_e] = \Omega\pi\rho \int_{-1}^1 \int_{-1}^1 r^2(\xi,\eta)\, [g'(\xi,\eta)]\, ||J(\xi,\eta)||\, d\xi\, d\eta, \tag{3.42}$$

where $[g']$ is the matrix given in Eq. (3.41), but transformed to the local coordinate system.

a) Cartesian        b) Cylindrical
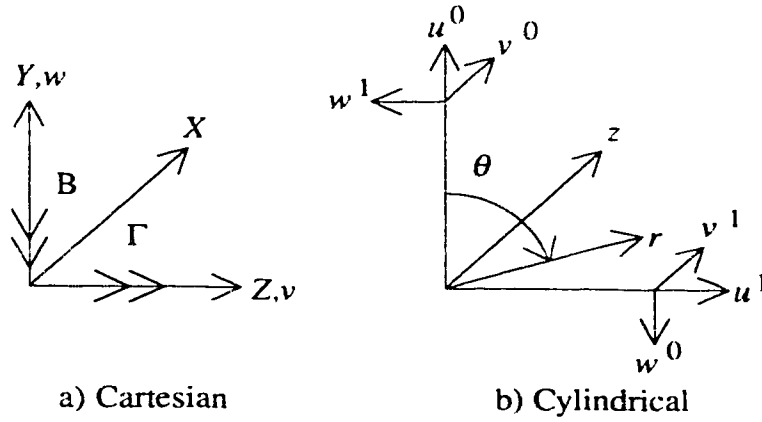
**FIGURE 3.14**: Displacements in the Cartesian and Cylindrical Coordinate Systems

Evaluating Eq. (3.42) using Gauss quadrature gives:

$$[G_e] = \Omega \pi \rho \sum_{i=1}^{n_\xi} \sum_{j=1}^{n_\eta} w_i\, w_j\, r^2(\xi_i, \eta_j)\, [g'(\xi_i, \eta_j)]\, \|J(\xi_i, \eta_j)\|, \qquad (3.43)$$

where $n_\xi$, $n_\eta$, and $w_\xi$, $w_\eta$ are the number of points, and the weighting factors for Gauss quadrature in the $\xi$ and $\eta$ directions respectively. Again, four point integration was used in both the $\xi$ and $\eta$ directions.

The axisymmetric gyroscopic matrix is both sparse and skew-symmetric, and as a result, considerable computational efficiencies can be attained by only calculating the duplicated non-zero components.

## 3.3.2 Boundary Conditions

The displacements in the cartesian and cylindrical coordinate systems at a particular axial and radial position are shown in Fig. 3.14. Note that $w^1$ is shown in the negative direction as given by the negative sum of equation Eq. (3.34). Boundary conditions for shafts are usually given as spring and damping coefficients in the cartesian coordinate system, which relate the effects of bearings and bearing

supports to shaft motion. The application of these boundary conditions is demonstrated by the transformation of the bearing stiffnesses at one particular point to stiffnesses applicable to the cylindrical coordinate system.

Referring again to Fig. 3.14, the displacement in the $Y$ direction of the cartesian coordinate system is given by $w$. The displacements in the cylindrical coordinate system at a particular position are defined either at $\theta = 0°$ or $\theta = 90°$ as shown. By inspection, the following relationships can be written for the nodal displacements:

$$u^0 = w \quad w^0 = -w$$
$$u^1 = v \quad w^1 = -v.$$

(3.44)

A bearing stiffness in the cartesian system, $K_{ww}$, represents a force in the $w$ direction (the first subscript) due to a unit displacement in the $w$ direction (second subscript). Using the relationships of Eq. (3.44), it can be seen from inspection that the additional stiffness $K_{ww}$ can be translated to the cylindrical coordinate system by adding or subtracting the bearing stiffness from the appropriate axisymmetric stiffnesses:

$$K_{u^0 u^0} \Rightarrow K_{u^0 u^0} + K_{ww}$$
$$K_{w^0 w^0} \Rightarrow K_{w^0 w^0} - K_{ww}.$$

(3.45)

Similarly, the effects of $K_{vv}$, $K_{wv}$, and $K_{vw}$ can be expressed as:

$$K_{u^1 u^1} \Rightarrow K_{u^1 u^1} + K_{vv}$$
$$K_{w^1 w^1} \Rightarrow K_{w^1 w^1} - K_{vv}$$

(3.46)

$$K_{u^0 u^1} \Rightarrow K_{u^0 u^1} + K_{uv}$$

$$K_{u^0 w^1} \Rightarrow K_{u^0 w^1} - K_{uv}$$

$$K_{w^0 u^1} \Rightarrow K_{w^0 u^1} - K_{uv}$$

$$K_{w^0 w^1} \Rightarrow K_{w^0 w^1} + K_{uv}$$

(3.47)

$$K_{u^1 u^0} \Rightarrow K_{u^1 u^0} + K_{vw}$$

$$K_{u^1 w^0} \Rightarrow K_{u^1 w^0} - K_{vw}$$

$$K_{w^1 u^0} \Rightarrow K_{w^1 u^0} - K_{vw}$$

$$K_{w^1 w^0} \Rightarrow K_{w^1 w^0} + K_{vw}.$$

(3.48)

Any damping coefficients that were expressed in the cartesian coordinates system could also be applied to the axisymmetric element model by using the same transformation of the displacements.

### 3.3.3 Zero Radius

At nodal circles with a radius of zero, the strain components containing $1/r$ terms, as given by Eq. (3.10), will have infinite magnitudes. To eliminate these strain components, the coefficients multiplying these $1/r$ terms must be zero (Belytschko [20]). This results in the following restrictions on displacements at zero radius:

$$u + \frac{\partial w}{\partial \theta} = 0$$

$$\frac{\partial u}{\partial \theta} - w = 0$$

(3.49)

$$\frac{\partial v}{\partial \theta} = 0.$$

Combining, Eq. (3.49) with the displacement relations given by Eq. (3.2), and collecting like trigonometric terms results in the following constraints at zero radius

(these constraints were given incorrectly by Geradin and Kill [15], and Stephenson and Rouch [21]):

$$u^0 = -w^0$$
$$v^0 = 0$$
$$u^1 = w^1$$
$$v^1 = 0.$$

(3.50)

These zero radius constraints have been applied for all the following shaft tests, and were also applied for all beam type tests.

### 3.3.4 Shaft Results

This section discusses the test of the full axisymmetric shaft element. However, the models in this section were calculated assuming that the shaft whirl and shaft running speed were synchronous, and that the orbit of the shaft was circular. The matrix equation of motion, where $[G^0]$ is the gyroscopic matrix due to the symmetric displacement components only, is:

$$
\begin{bmatrix} [M_e] & [0] \\ [0] & [M_e] \end{bmatrix} \begin{Bmatrix} \{\ddot{\delta}_e^0\} \\ \{\ddot{\delta}_e^1\} \end{Bmatrix} + \begin{bmatrix} [0] & [G_e^0] \\ [-G_e^0] & [0] \end{bmatrix} \begin{Bmatrix} \{\dot{\delta}_e^0\} \\ \{\dot{\delta}_e^1\} \end{Bmatrix}
$$

$$
+ \begin{bmatrix} [K_e] & [0] \\ [0] & [K_e] \end{bmatrix} \begin{Bmatrix} \{\delta_e^0\} \\ \{\delta_e^1\} \end{Bmatrix} = \begin{Bmatrix} \{0\} \\ \{0\} \end{Bmatrix}.
$$

(3.51)

Letting the antisymmetric displacements lag the symmetric displacements by $\pi/2$, and assuming a circular orbit results in the following relationships:

$$\{\delta_e^0\} = \{\delta_e\}e^{j\omega t} \qquad \{\delta_e^1\} = -j\{\delta_e\}e^{j\omega t}$$

$$\{\dot{\delta}_e^0\} = j\omega\{\delta_e\}e^{j\omega t} \qquad \{\dot{\delta}_e^1\} = \omega\{\delta_e\}e^{j\omega t} \qquad (3.52)$$

$$\{\ddot{\delta}_e^0\} = -\omega^2\{\delta_e\}e^{j\omega t} \qquad \{\ddot{\delta}_e^1\} = j\omega^2\{\delta_e\}e^{j\omega t}$$

Since from Eq. (3.52), $\{\dot{\delta}_e^0\} = \frac{1}{\omega}\{\ddot{\delta}_e^1\}$ and $\{\dot{\delta}_e^1\} = -\frac{1}{\omega}\{\ddot{\delta}_e^0\}$, then Eq. (3.51) can be rewritten as:

$$\begin{bmatrix} [M_e] - \frac{1}{\omega}[G_e^0] & [0] \\ [0] & [M_e] - \frac{1}{\omega}[G_e^0] \end{bmatrix} \left\{ \begin{array}{c} \{\ddot{\delta}_e^0\} \\ \{\ddot{\delta}_e^1\} \end{array} \right\}$$

$$+ \begin{bmatrix} [K_e] & [0] \\ [0] & [K_e] \end{bmatrix} \left\{ \begin{array}{c} \{\delta_e^0\} \\ \{\delta_e^1\} \end{array} \right\} = \left\{ \begin{array}{c} \{0\} \\ \{0\} \end{array} \right\}. \qquad (3.53)$$

As shown by Eq. (3.53), assuming synchronous circular whirl uncouples the symmetric and antisymmetric displacements of the shaft. Also, since the stiffness, mass, and gyroscopic matrices are the same for both the symmetric and antisymmetric unknowns of the element, only the mode shapes and frequencies for either the symmetric or antisymmetric displacements need to be calculated. Therefore, the degrees of freedom of a problem can be limited to the same number as that of the simple beam type representation using the axisymmetric element.

The element was first tested on the overhung shaft model shown in Fig. 3.15. The model was steel, and natural frequencies for zero shaft speed, and synchronous forward and backward whirl were calculated. The same idealization was also modelled using Timoshenko shaft elements and the whirl speed results are compared in Table 3.3. For the first whirl speed, the Timoshenko and axisymmetric models gave nearly equal results. However, for the second and third whirl speeds, the zero shaft speed, and forward whirl of the axisymmetric model were considerably different.

$$E = 30 \times 10^6 \text{ psi.,} \quad \rho = 0.283 \text{ lbs./in.}^3, \quad \nu = 0.30, \quad K = 0.886$$
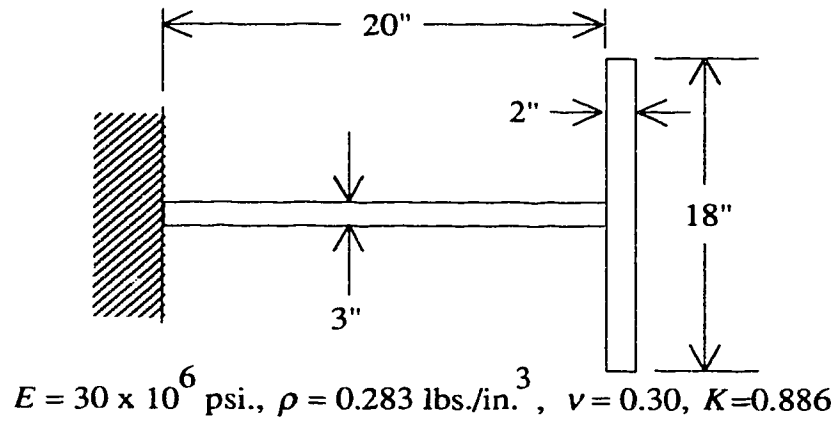
**FIGURE 3.15**: Overhung Shaft Model

**TABLE 3.3**: Whirl Speeds of Overhung Shaft (CPM)

| Mode | Timoshenko | | | Axisymmetric | | |
|---|---|---|---|---|---|---|
| | Back. Whirl | No Shaft Speed | For. Whirl | Back. Whirl | No Shaft Speed | For. Whirl |
| 1 | 2773 | 3060 | 3406 | 2811 | 3110 | 3489 |
| 2 | 10832 | 16720 | 73696 | 10651 | 13516 | 56609 |
| 3 | 75750 | 76832 | 184000 | 84413 | 85860 | 151900 |

The axisymmetric shaft element was also tested on the Nelson-McVaugh [19] rotor, as shown in Fig. 3.16. Since, modelling the rotor as one complete system using axisymmetric elements would have required too many degrees of freedom, the shaft was split into four subsections as shown in Fig. 3.17. The matrices for each subsection were then reduced in size using component mode reduction, and ten normal modes were retained for each. The master nodes for each subsection are also indicated in the diagram. Geradin also analyzed the rotor using component mode reduction, with the model being split into similar components, with a total of forty modes retained. A comparison of the first three whirl speeds predicted using the axisymmetric element, the Timoshenko element, the Nelson's beam-shaft element, and the Geradin axisymmetric element is given in Table 3.5. The Timoshenko model was broken down into the eighteen elements shown in Fig. 3.16. The shaded section of the shaft was an added disk with an outside diameter of 0.1032m, an inside diameter of 0.0406m, and a thickness of 0.0254m. There are a number of discrepancies between the dimensions of the rotor as given by Nelson-McVaugh and Geradin. For instance, the shaft radii listed by Nelson are actually diameters, and the added disk data is inconsistent (mass, polar and diametral moment of inertia). The dimensions used in this thesis are given in Table 3.4. The supports were transverse springs with the following stiffness: $4.378 \times 10^7 \text{N/m}$.

The zero shaft whirl speeds (natural frequencies) for the isoparametric axisymmetric element were lower than all the other models, except for the first. This suggests that the stiffness of the axisymmetric model was somewhat less than that of the beam type element models. The first natural frequency for the isoparametric axisymmetric model was higher than that predicted by the Timoshenko shaft model. This is due to the shaded disk only adding mass to the Timoshenko model, while for the axisymmetric model the disk added stiffness as well. In the first mode of vibration, the left end of the rotor acts essentially as a cantilever beam, so that the section with the disk underwent a large bending deflection. Therefore, the extra
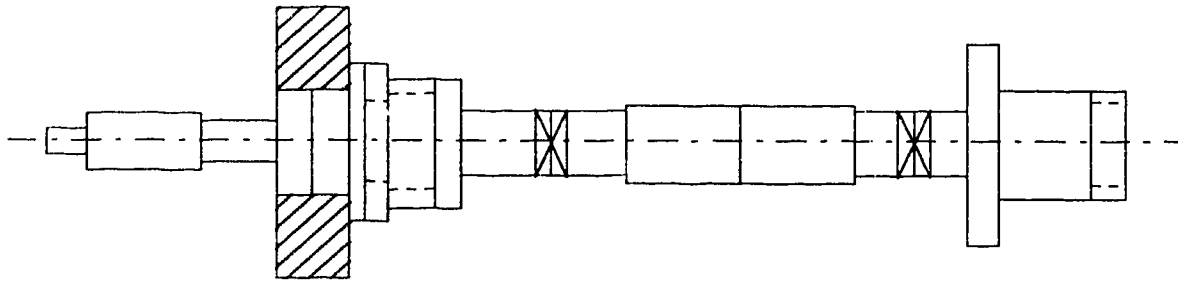
**FIGURE 3.16**: Nelson-McVaugh Rotor

stiffness of the disk in the axisymmetric model discretization increased the first natural frequency significantly. For the second mode, the right end of the rotor underwent the greatest deflection. While for the third mode, the middle section between the two supports underwent the greatest deflection. Hence, for these modes the stiffness of the disk in the axisymmetric model did not increase the predicted natural frequencies above those of the Timoshenko model. The Nelson-McVaugh rotor has a number of step changes, so that it is reasonable to expect that the stiffness of the rotor modelled with the axisymmetric elements would not be as high as predicted by bending theory. This agrees with the introductory discussion that at a step change in diameter the material on the larger diameter side of the change may not contribute fully to the bending stiffness. Some error is also inherent in the component mode reduction technique. With component mode reduction the model is partitioned into master and slave degrees of freedom, with the slave degrees of freedom being defined in terms of the master degrees of freedom using a static condensation technique. However, component mode reduction increases the accuracy of a dynamic analysis over that using a purely static condensation by retaining extra modes for each component, where the mode shapes are found by constraining the component master degrees of freedom.

Section I      Section II          Section III         Section IV

$$E = 2 \times 10^{11} N/m^2, \quad \rho = 7806 \ kg/m^3, \quad \nu = 0.287, \ K = 0.885$$
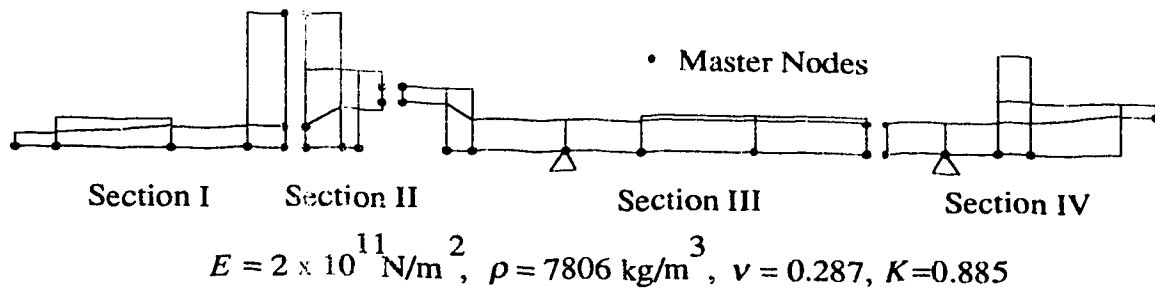
**FIGURE 3.17**: Axisymmetric Element Model of Nelson-McVaugh Rotor

**TABLE 3.4**: Nelson-McVaugh Rotor Dimensions

| Elem. No. | Len. m. | Inner Dia. m. | Outer Dia. m. | Elem. No. | Len. m. | Inner Dia. m. | Outer Dia. m. |
|---|---|---|---|---|---|---|---|
| 1 | 0.0127 | - | 0.0102 | 10 | 0.0305 | - | 0.0254 |
| 2 | 0.0381 | - | 0.0203 | 11 | 0.0254 | - | 0.0254 |
| 3 | 0.0254 | - | 0.0152 | 12 | 0.0381 | - | 0.0305 |
| 4 | 0.0127 | - | 0.0406 | 13 | 0.0381 | - | 0.0305 |
| 5 | 0.0127 | - | 0.0406 | 14 | 0.0203 | - | 0.0254 |
| 6 | 0.0051 | - | 0.0660 | 15 | 0.0178 | - | 0.0254 |
| 7 | 0.0076 | 0.0305 | 0.0660 | 16 | 0.0102 | - | 0.0762 |
| 8 | 0.0127 | 0.0356 | 0.0508 | 17 | 0.0305 | - | 0.0406 |
| 9 | 0.0076 | - | 0.0508 | 18 | 0.0127 | 0.0305 | 0.0406 |

**TABLE 3.5**: Whirl Speeds of Nelson-McVaugh Rotor

| Mode | Axisym. (CPM) | Timo. (CPM) | Neis.-McV. (CPM) | Ger.-Kill (CPM) |
|---|---|---|---|---|
| 1 | 15902 B<br>16649 N<br>17469 F | 15571 B<br>16358 N<br>17228 F | 15470 B<br>16267 N<br>17159 F | 14987 B<br>16119 N<br>17164 F |
| 2 | 43508 B<br>45421 N<br>47205 F | 47285 B<br>47357 N<br>47407 F | 46612 B<br>48384 N<br>49983 F | 45570 B<br>47761 N<br>49597 F |
| 3 | 61137 B<br>70027 N<br>85229 F | 65712 B<br>76874 N<br>91350 F | 64752 B<br>76382 N<br>96457 F | 62450 B<br>75155 N<br>92219 F |

B = Backward Whirl. N = No Shaft Speed, F = Forward Whirl
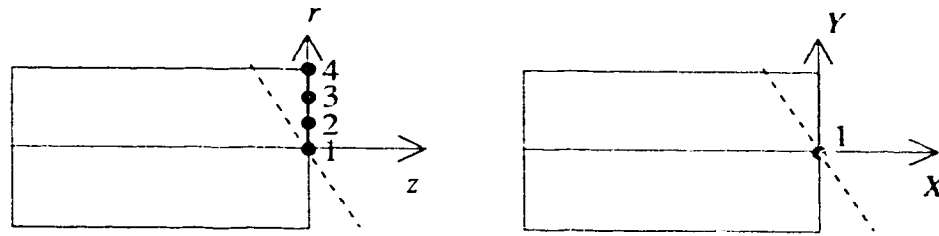
**FIGURE 3.18**: Transformation of Nodes

## 3.4 Coupling of Axisymmetric to Beam-Shaft Elements

Since the axisymmetric element has a large number of degrees of freedom, modelling a whole rotor system with the element may require large amounts of computer memory and time to calculate. The process may be simplified by using a condensation technique such as component mode reduction to make the problem a manageable size in terms of computer memory. However, fairly long sections of a rotor system are often uniform in size, and can be modelled adequately with just a Timoshenko shaft element. The axisymmetric element is necessary when modelling sections of the rotor system that have numerous diameter changes, tapers, or perhaps a number of wheels or disks. It would be advantageous to use both elements in one model thereby combining the simplicity and minimum memory requirements of the Timoshenko element with the accuracy of the axisymmetric element for the more complex geometry sections. This section describes a method for linking the two kinds of elements, and gives the results for a test of the method on a sample rotor.

The coordinate systems and displacements for the Timoshenko shaft element and the axisymmetric element were previously shown in Fig. 3.14. From this figure, the translations as defined in the two coordinate systems are related by $w = u^0$ at $\theta = 0°$, and $w = -w^0$ at $\theta = 90°$. The slope of the element faces can be related by $\Gamma = -\frac{\partial v^0}{\partial r}$ at $\theta = 0°$, and $B = -\frac{\partial v^1}{\partial r}$ at $\theta = 90°$. Since the displacements

in three dimensions at each of the nodal circles for the axisymmetric element must coincide with the translations and slopes at the single node of the Timoshenko shaft element as shown in Fig. 3.18. the relationships between the two are not unique. To join a shaft subsystem modelled with axisymmetric elements to one modelled with Timoshenko elements the number of nodal unknowns at the junction must be the same. The transformation chosen sets the lateral translation of all four nodal circles in the axisymmetric domain equal to the translation of the single node in the beam-shaft domain. Also. the axial displacement of the nodal circles can be calculated by multiplying the angle $\Gamma_1$ by the radius of the nodal circle. This constrains the interconnecting surface of the axisymmetric component to a planar translation and rotation as defined by bending theory, and can be written as:

$$
\begin{Bmatrix} u_1^0 \\ v_1^0 \\ w_1^0 \\ u_2^0 \\ v_2^0 \\ w_2^0 \\ u_3^0 \\ v_3^0 \\ w_3^0 \\ u_4^0 \\ v_4^0 \\ w_4^0 \end{Bmatrix} = \begin{bmatrix} 1 & 0 \\ 0 & 0 \\ -1 & 0 \\ 1 & 0 \\ 0 & -r_2 \\ -1 & 0 \\ 1 & 0 \\ 0 & -r_3 \\ -1 & 0 \\ 1 & 0 \\ 0 & -r_4 \\ -1 & 0 \end{bmatrix} \begin{Bmatrix} w_1 \\ \Gamma_1 \end{Bmatrix}.
\tag{3.54}
$$

The transformation is performed at any axisymmetric nodes to be connected to beam type nodes, which would normally occur at one or two places on the axisymmetric subsection. The intermediate nodal unknowns can be transformed

from the cylindrical coordinate system to the cartesian coordinate system by a simple one to one correspondence (i.e. an identity matrix).

This technique was tested on a simply supported shaft system as shown in Fig. 3.19. The results comparing modelling the subsections with Timoshenko and axisymmetric elements, and with either axisymmetric or Timoshenko elements totally, are given in Table 3.6. For the coupled element test, Sections I and III of the shaft were modelled with nine and three Timoshenko shaft elements respectively, and Section II was modelled with seven axisymmetric elements for a combined model of 150 degrees of freedom. When the shaft was completely modelled with axisymmetric elements, Sections I had two elements, Section II had seven elements, and Section III had a single element for a total of 194 degrees of freedom. The shaft was also completely modelled with eighteen, six and nine Timoshenko elements for the three sections respectively. As can be seen, the results between the three different modelling methods compare well. The lowest natural frequency using the combined axisymmetric and Timoshenko shaft element model was less than 2.0% different from that calculated with the completely axisymmetric model. The axisymmetric element is less constrained than the Timoshenko shaft element, and hence the natural frequencies of the axisymmetric model are lower than those of the Timoshenko model. However, the combined axisymmetric and Timoshenko shaft element model had a combination of the constraints of the other two models, and should predict natural frequencies between those of the other models. As shown, the combined model predicted natural frequencies less than those of the axisymmetric model, suggesting that the combined model is less constrained. The reason for this is unknown at the present time, and these results suggest that the coupling method presented here requires further investigation.
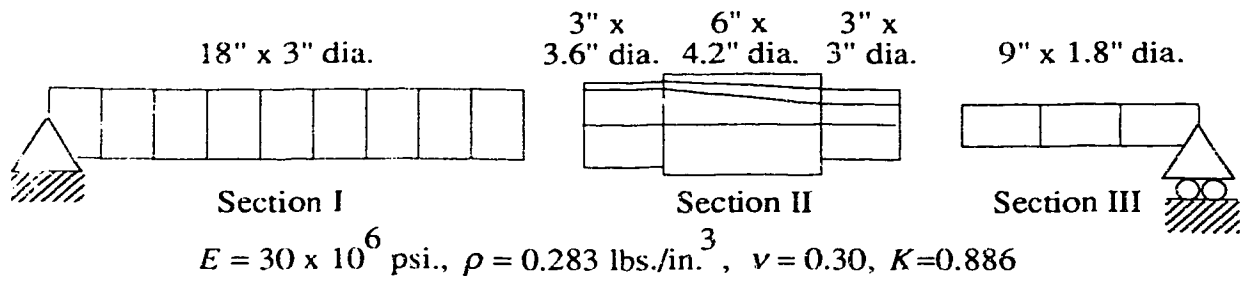
FIGURE 3.19: Test Shaft

TABLE 3.6: Nat. Frequencies of Test Shaft

| Mode | Axisymmetric (CPM) | Timoshenko (CPM) | Axi + Timo (CPM) |
|------|--------------------|-------------------|-------------------|
| 1 | 7528 | 7610 | 7398 |
| 2 | 28294 | 28657 | 28149 |
| 3 | 78516 | 79016 | 78267 |

# 3.5 Conclusions

Although the axisymmetric element allows greater freedom in modelling of shaft shapes, and includes the ability to represent torsional and axial vibration modes, the increased complexity and larger number of unknowns tend to outweigh the advantages. The axisymmetric element does provide better accuracy as well, but should be limited to use where the number of steps, tapers, etc., may introduce limitations in the accuracy of the Timoshenko type shaft elements. For the cases tested, the axisymmetric element did not provide results that were significantly different from those calculated with the Timoshenko shaft elements. Considering the large matrices generated when modelling shafts with the axisymmetric element, the use of the element is not justified for most situations. That is, the axisymmetric element should only be used where a non-uniform shaft section may severely limit the higher mode predictions of the Timoshenko element.

The axisymmetric element may provide a suitable basis for modelling and studying the stiffening effects of shrink fit wheels and disks. The modification of the element to accommodate thermal expansion is a suitable area of future research.

# CHAPTER 4

# On the Application of Bearings

*Methinks it is like a weasel.* *— Shakespeare*

## 4.1 Introduction

This chapter does not introduce new material, but instead recognizing the importance of the supports to the dynamics of the total rotor system, presents an overview of bearing and support modelling methods.

The classical boundary conditions for shafts and beams, as shown in Fig. 4.1, are approximations of the actual boundary conditions exhibited in turbomachines. A pinned end is similar to a spring or short bearing with an infinite translational stiffness; and a clamped end is similar to a support or long bearing with both infinite translational and rotational stiffnesses. Of course, these boundary conditions are normally modelled by constraining out the appropriate degrees of freedom representing the translational or angular stiffnesses, or by applying springs of several orders of magnitude greater stiffness than the flexible stiffness of the rotor being modelled.

However, these simple methods may not model actual bearings and their supports adequately, and as is well known, the actual boundary conditions can have a significant effect on the dynamic characteristics and response of a complete

70

(a)                                          (b)
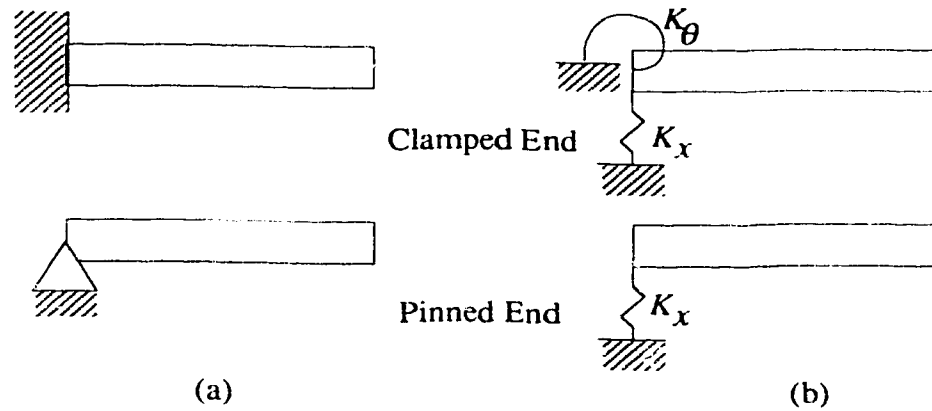
**FIGURE 4.1**: End Conditions: (  )    .     ) Modelled

rotor-bearing system.

Rolling element bearings have high stiffnesses, and can often be modelled well as pinned or clamped boundary conditions. As well, the bearing can be modelled with linear stiffness and damping terms, although these may have to be determined experimentally.

Journal (hydrodynamic) bearings are not well represented in this manner. The bearings have cross-coupling stiffnesses; that is, a vertical motion of the journal in the bearing will cause a horizontal reaction force. Also, journal bearings are often modelled with linear stiffness and damping terms, but for many possible motions of the journal in the bearing, the actual stiffness and damping introduced is highly non-linear. This chapter will discuss the hydrodynamic bearing model normally used, and also the effect of the bearing on the dynamic characteristics of the rotor-bearing system.
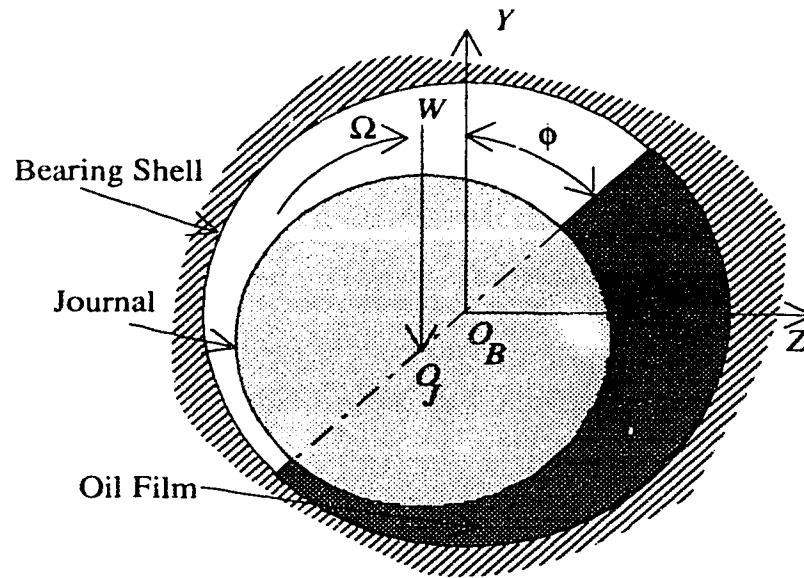
FIGURE 4.2: Hydrodynamic Bearing

## 4.2 Hydrodynamic Bearings: Steady Running

The simplest type of hydrodynamic bearing has a circular bearing shell made in two halves, that fit around the shaft (journal) with some diametral clearance (see Fig. 4.2). The ratio of the axial length of the bearing to the shaft diameter is normally in the range of 0.5 to 1.0. Oil is supplied to the bearing through two axial grooves at the bearing shell joints in the horizontal plane, and the oil exits the bearing by leaking out the bearing ends. The oil supply pressure is much lower than the pressure of the load on the journal projected over the bearing area, and as a result, hydrodynamic bearings rely on the pumping action of the spinning journal to create a fluid film that supports the rotor, and prevents metal to metal contact. In a few cases, the bottom half of the bearing may have holes to provide high-pressure jacking oil which lifts the journal away from the bearing shell only at low speeds, or when the rotor is not spinning.

When the rotor has reached some minimum speed, the pumping action of the

journal will form a convergent wedge of oil (oil film) which lifts the rotor out of contact with the bearing shell. The oil wedge starts at or near the position of maximum clearance, and continues around the journal in the direction of journal rotation to the position of minimum clearance. Outside of the oil wedge is a broken or aerated oil film which is at atmospheric pressure. The journal center, $O_J$, is displaced from the bearing center, $O_B$, and the ratio of center displacement to radial clearance is known as the eccentricity, $\varepsilon$. The angle from the vertical to the diameter through the maximum and minimum clearances is known as the attitude angle, $\phi$. The displacement of the journal center from the bearing center must fall on the attitude line.

The external load, $W$, results in a mean pressure on the projected area of the journal given by:

$$p' = \frac{W}{DL},$$  (4.1)

where $D =$ the journal diameter, and $L =$ the journal length.

A dimensionless pressure may be defined by:

$$p_m = \frac{p'}{\mu N} \left(\frac{D}{C}\right)^2.$$  (4.2)

Taking the reciprocal of Eq. (4.2) gives the Sommerfeld duty parameter (as given by Eq. (4.3)), which determines the attitude angle and eccentricity of the journal. The Sommerfeld number is used as a similarity number between bearings of similar shape. Here, $N =$ the shaft speed in revolutions per second, $\mu =$ the dynamic viscosity, and $C =$ the diametral clearance.

$$S = \frac{\mu DLN}{W} \left(\frac{D}{C}\right)^2$$  (4.3)

journal will form a convergent wedge of oil (oil film) which lifts the rotor out of contact with the bearing shell. The oil wedge starts at or near the position of maximum clearance, and continues around the journal in the direction of journal rotation to the position of minimum clearance. Outside of the oil wedge is a broken or aerated oil film which is at atmospheric pressure. The journal center, $O_J$, is displaced from the bearing center, $O_B$, and the ratio of center displacement to radial clearance is known as the eccentricity, $\varepsilon$. The angle from the vertical to the diameter through the maximum and minimum clearances is known as the attitude angle, $\phi$. The displacement of the journal center from the bearing center must fall on the attitude line.

The external load, $W$, results in a mean pressure on the projected area of the journal given by:

$$p' = \frac{W}{DL},$$

(4.1)

where $D$ = the journal diameter, and $L$ = the journal length.

A dimensionless pressure may be defined by:

$$p_m = \frac{p'}{\mu N} \left(\frac{D}{C}\right)^2.$$

(4.2)

Taking the reciprocal of Eq. (4.2) gives the Sommerfeld duty parameter (as given by Eq. (4.3)), which determines the attitude angle and eccentricity of the journal. The Sommerfeld number is used as a similarity number between bearings of similar shape. Here, $N$ = the shaft speed in revolutions per second, $\mu$ = the dynamic viscosity, and $C$ = the diametral clearance.

$$S = \frac{\mu DLN}{W} \left(\frac{D}{C}\right)^2$$

(4.3)

For many turbomachines under steady state running conditions, the load exerted on the bearing has a constant magnitude and direction. The greatest component of bearing load is normally the weight of the rotor system, with hydraulic forces adding smaller components in the non-vertical directions. As shown in Fig. 4.2 the vertical load $W$ causes a downward and horizontal displacement of the journal relative to the shell center. The journal will attain an eccentric equilibrium position for a steady load. A small perturbation in load will cause a small displacement with both horizontal and vertical components from the equilibrium position, but the journal motion will normally reattain the equilibrium position. Hence, the bearing can be considered stable under most steady-state conditions. However, when lightly loaded, the eccentricity of the journal is small, and the reaction forces due to a light constant load may include a significant component in the direction of shaft rotation. When this occurs, the journal will orbit about the bearing on a circular path, the amplitude of which is controlled by the damping introduced by the bearing, but which may still be excessive. The bearing then, is not considered stable under steady state conditions.

## 4.3  Hydrodynamic Bearings: Non-Steady Running

As was discussed in the steady running section, applying a steady vertical load to the bearing journal will cause it to move to an equilibrium position as shown in Fig. 4.2, where the center of the journal $O_J$ has moved downward and horizontally along the attitude line (at an angle $\phi$ from the vertical). For dynamic loads, the motion of the journal in the bearing and the structure of the oil film can have a variety of regimes. If a small additional rotating load, caused by imbalance or fluid-rotor dynamics (harmonic with the shaft rotation speed), is applied to the journal, the journal will whirl in a small elliptical orbit about its equilibrium position (see Fig. 4.3). As well, the position of the convergent fluid film in the bearing will
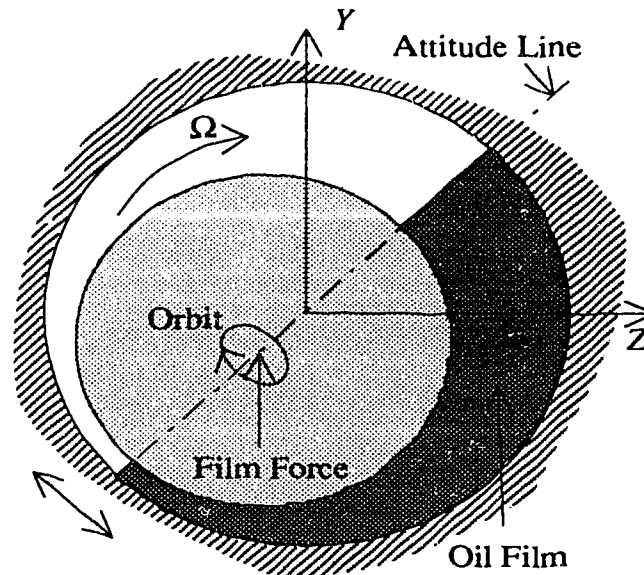
**FIGURE 4.3**: Oscillating Fluid Film

oscillate slightly. If the transient load amplitude is increased, the whirl orbit of the journal will increase in size, and the oscillation of the fluid film will increase. When the load amplitude is large enough the oscillation of t' e fluid film will cease, and instead the fluid film (and its position of minimum thickness) will whirl around the bearing with the journal in essentially a circular orbit with constant eccentricity. If the whirl frequency is less than one-half the shaft rotation frequency then the fluid film will trail the journal motion (as shown in Fig. 4.4). And when the whirl frequency is greater than one-half of the shaft ro. .ion frequency, the fluid film will lead the journal motion (see Fig. 4.5). Note that for rotating film cases the attitude line and resultant force exerted on the journal by the fluid film rotate around the inside of the bearing at the whirl frequency.

For the trailing rotating fluid film regime, the resultant force due to the fluid film pressure has a component normal to the attitude line that is in the direction of whirl. Therefore, energy is supplied to the whirl, and a trailing rotating fluid film is usually considered unstable. The resulting orbit may be limited by the non-
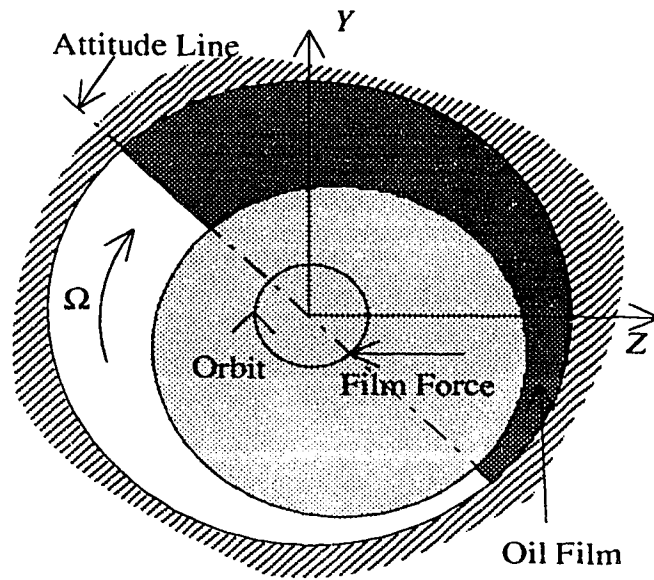
**FIGURE 4.4**: Trailing Rotating Fluid Film
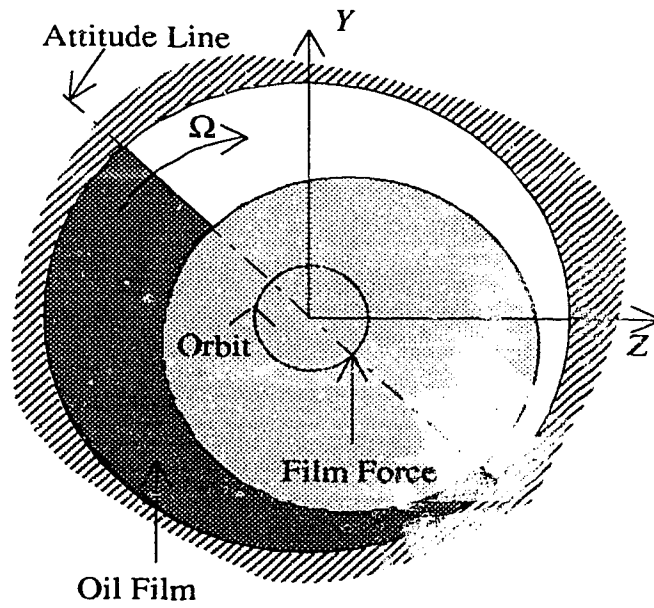


**FIGURE 4.5**: Leading Rotating Fluid Film

linearity of the stiffnesses of the bearing when the eccentricities are large, and by the damping introduced by the bearing. The instability is worse for journals subject to light steady loads. When the steady load is light, the journal eccentricity is small, and the resultant fluid film force is nearly perpendicular to the attitude line. In this case, the rotating force does not need to be large to induce the rotating fluid film and whirl of the shaft. When the steady load is large, the eccentricity of the journal will also be large, and the resulting fluid force on the journal will be nearly parallel to the attitude line. As a consequence, the heavily loaded bearing is much less likely to attain the rotating fluid film regime, and hence the condition of unstable whirl is not a concern.

For the leading rotating fluid film regime, the resultant fluid film force on the journal has a component normal to the attitude line pointing in the direction opposite to whirl, and as a result the force resists the whirling motion of the journal.

## 4.4  Bearing Models

To determine the stiffness and damping coefficients that would model a journal bearing a number of assumptions must be made. The common assumptions for conventional hydrodynamic theory are given by Smith [22], and are as follows:

1) The lubricating film thickness is small compared with the journal dimensions.

2) The journal is cylindrical and of known diameter, and the bearing is of known shape and dimensions.

3) The journal axis is parallel to the bearing axis.

4) The inertia of the lubricating film is negligible.

5) The film is unable to sustain sub-atmospheric pressures. And the film pressure is ambient along the supply and drain boundaries, and wherever the film is broken or cavitated.

6) The film flow is laminar.

7) The lubricating fluid is a simple Newtonian fluid.

8) The viscosity and density of the fluid is uniform throughout the bearing.

In an oil film for which the above assumptions are valid, and under conditions of steady load and speed, the pressure distribution in the film is given by the Reynold's equation for lubrication in a channel:

$$\frac{\partial}{\partial s}\left(\frac{\rho h^3}{\mu}\cdot\frac{\partial p}{\partial s}\right) + \frac{\partial}{\partial z}\left(\frac{\rho h^3}{\mu}\cdot\frac{\partial p}{\partial z}\right) = 6U\frac{\partial \rho h}{\partial s}. \tag{4.4}$$

where $h$ = the film thickness, $s$ = the distance in the tangential direction, $z$ = the distance in the axial direction, $\rho$ = the oil density, $\mu$ = the dynamic viscosity, and $U$ = the peripheral speed of the journal. To determine the stiffness and damping provided by the bearing, Eq. (4.4) is non-dimensionalized, and a small perturbation from the equilibrium position is imposed on the journal. The perturbation displacement has components in both the horizontal and vertical directions. and a first order linear perturbation analysis is done upon the Reynold's equation to calculate the resulting changes in reaction force. If $Z$ and $Y$ are the horizontal and vertical directions then the reaction force components on the journal are non-linear functions of the displacement and velocities in those directions. That is:

$$F_Z = F_Z(Z, Y, \dot{Z}, \dot{Y})$$
$$F_Y = F_Y(Z, Y, \dot{Z}, \dot{Y}).$$

(1.5)

However, using first order terms of Taylor series near the journal equilibrium position, these functions can be linearized. The total force is the sum of the static reaction force at equilibrium (subscript $o$), and the incremental reaction force due to the small perturbation from the equilibrium position. That is:

$$\vec{F} = \vec{F}_o + \triangle\vec{F},$$

(4.6)

where, the incremental force is given by:

$$\triangle\vec{F} = [K] \left\{ \begin{array}{c} \triangle Z \\ \triangle Y \end{array} \right\} + [C] \left\{ \begin{array}{c} \triangle \dot{Z} \\ \triangle \dot{Y} \end{array} \right\}.$$

(4.7)

And, the stiffness and damping matrices can be written as:

$$[K] = \left[ \begin{array}{cc} \frac{\partial F_Z}{\partial Z} & \frac{\partial F_Z}{\partial Y} \\ \frac{\partial F_Y}{\partial Z} & \frac{\partial F_Y}{\partial Y} \end{array} \right]_o = \left[ \begin{array}{cc} K_{ZZ} & K_{ZY} \\ K_{YZ} & K_{YY} \end{array} \right]$$

(4.8)

$$[C] = \left[ \begin{array}{cc} \frac{\partial F_Z}{\partial Z} & \frac{\partial F_Z}{\partial Y} \\ \frac{\partial F_Y}{\partial Z} & \frac{\partial F_Y}{\partial Y} \end{array} \right]_o = \left[ \begin{array}{cc} C_{ZZ} & C_{ZY} \\ C_{YZ} & C_{YY} \end{array} \right].$$

A diagrammatic representation of the normal bearing model is shown in Fig. 4.6. The diagram shows a bearing of a shaft rotating at speed $\Omega$, and looking along the $X$ axis. Hydrodynamic bearings are not well modelled as simple springs, as the bearing has cross-coupled stiffnesses. The hydrodynamic bearing can also introduce a significant amount of damping to the system.
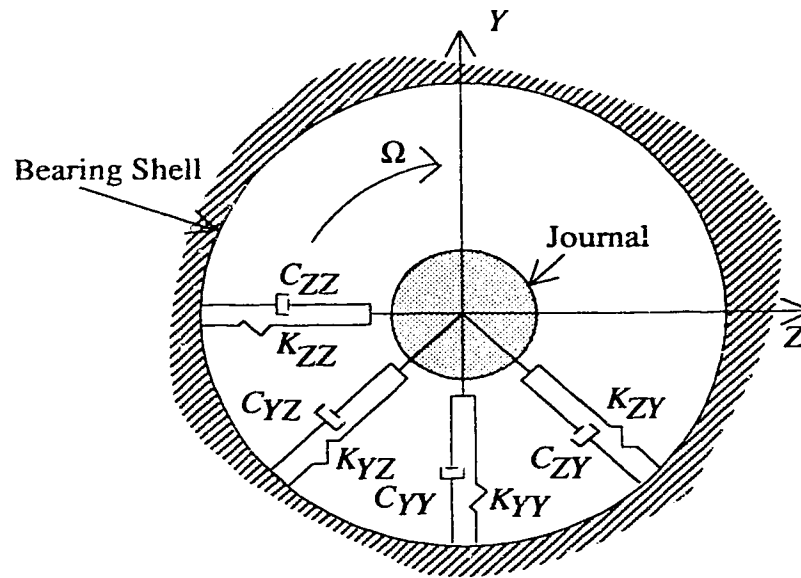
**FIGURE 4.6**: Bearing Dynamic Model

Note, it is generally the case that $K_{ZY} \neq K_{YZ}$. In fact, $K_{ZY}$ is usually negative (except for very large eccentricity ratios) with a magnitude considerably different from $K_{YZ}$. Because of these large cross-coupling stiffnesses, a load in one direction causes a displacement of the journal in that direction, as well as in the orthogonal direction. These displacements in return cause a restoring force in the direction of the load and an additional force orthogonal to it. The result is an elliptical orbit of the journal inside the bearing. The orbit may be circular if the displacement of the journal in the bearing is large. Then the journal will orbit about the inside diameter of the bearing, with an almost constant clearance between the journal and bearing. The orbit is generally in the same direction as shaft rotation, but may be in the opposite direction (backward whirl) if the stiffnesses of the shaft and/or bearing are not the same in both $Z$ and $Y$ directions.

The damping matrix has positive components and is symmetric, resulting in a complex solution, when examining the forced response of the system; and in complex eigenvalues and eigenvectors when calculating the natural frequencies of the system.

Calculated and measured non-dimensionalized dynamic coefficients for a number of bearing types may be found in references such as Someya [23] and MTI [24]. It must be noted that bearing coefficients must be calculated at each rotation speed of the shaft, as the journal eccentricity, and the stiffnesses and damping of the bearing are dependent on the shaft speed.

The effect of the bearing damping on the rotor-bearing system depends on the ratio of the stiffness of the bearings to the shaft flexural stiffness. If the bearings are much stiffer than the shaft, then the displacements at the bearings become small in comparison to the shaft bending deflections, and hence the velocities and energy dissipated at the bearings are small. Therefore, the bearing damping will not have much effect on the system. If bearing stiffnesses are small in comparison to shaft flexural stiffnesses, then the displacements at the bearings become large relative to the bending deflections, and the rotor motion is essentially that of a rigid body. Therefore, the damping due to the bearings will be effective at dissipating energy.

Present models for hydrodynamic bearings are deficient in two major areas. The first is that the angular displacement of the journal relative to the bearing shell (assumption (3)) in the axial direction does not cause any restoring moments or have any damping effect. This may be an acceptable error for bearings which are short (i.e., the length of the bearing shell over the diameter of the journal $\leq 0.5$). For long bearings, however, this is definitely a problem. For bearings that are very long ($L/D \geq 1.0$) the effect of the bearing begins to approach that of the clamped boundary condition. As well, the coefficients as they are now calculated assume that the oil film thickness is constant in the axial direction. Solutions of the Reynold's lubrication equation and calculation of the translational stiffness and damping coefficients must account for the angular misalignment of the shaft. In addition the calculation of the resultant angular stiffness and damping effects of misalignment is a worthy area of future research.

Second, bearing stiffness and damping coefficients are determined by examining the effect of small displacements of the journal from its equilibrium position. If a rotating force is applied which causes a large change in the eccentricity of the bearing, then the actual stiffness and damping of the bearing are highly non-linear. As a result, the linear spring and damping models in current use can only model the dynamics of the rotor-bearing system where the displacements from the equilibrium position are not too large. As noted by Taylor and Craggs [25], it is common for turbomachines to have journals with orbits taking up 60 − 70% of the bearing clearances, which is a large violation of the small perturbation assumption. From Eq. (4.3), the Sommerfeld number depends on shaft speed and external load. Since the eccentricity and attitude angle (equilibrium position) depend on the Sommerfeld number, and the stiffness and damping coefficients are determined in relation to a specific equilibrium position, the coefficients should be determined for each possible load and running speed of the machine. That is, the non-linearity of the coefficients require that the coefficients used should be calculated based on the predicted response of the journal to an applied external force. But, since the rotor response is dependent on the coefficients used, modelling a rotor-bearing system accurately would require that the bearing coefficients and response of the rotor be calculated iteratively for a certain rotating applied force, until a complementary set of coefficients and responses are determined.

## 4.5 Bearing Supports

Not only do the bearings themselves add flexibility and damping to the system, but so also do the bearing supports. That is, the bearing pedestals and foundations of the machine influence the rotor dynamic characteristics of the machine. And of course, the pedestals may also be modelled as beams which branch into the shaft, introducing additional degrees of freedom into the system. See Fig. 4.7.

The governing matrix equation of motion for a bearing and support is:

$$
\begin{bmatrix}
M_{ZZ_1} & 0 & 0 & 0 \\
0 & M_{YY_1} & 0 & 0 \\
0 & 0 & M_{ZZ_2} & 0 \\
0 & 0 & 0 & M_{YY_2}
\end{bmatrix}
\begin{Bmatrix}
\ddot{Z}_1 \\
\ddot{Y}_1 \\
\ddot{Z}_2 \\
\ddot{Y}_2
\end{Bmatrix}
$$

$$
+
\begin{bmatrix}
C_{ZZ_1} & C_{ZY_1} & -C_{ZZ_1} & -C_{ZY_1} \\
C_{YZ_1} & C_{YY_1} & -C_{YZ_1} & -C_{YY_1} \\
-C_{ZZ_1} & -C_{ZY_1} & C_{ZZ_1} & C_{ZY_1} \\
-C_{YZ_1} & -C_{YY_1} & C_{YZ_1} & C_{YY_1}
\end{bmatrix}
\begin{Bmatrix}
\dot{Z}_1 \\
\dot{Y}_1 \\
\dot{Z}_2 \\
\dot{Y}_2
\end{Bmatrix}
\qquad (4.9)
$$

$$
+
\begin{bmatrix}
K_{ZZ_1} & K_{ZY_1} & -K_{ZZ_1} & -K_{ZY_1} \\
K_{YZ_1} & K_{YY_1} & -K_{YZ_1} & -K_{YY_1} \\
-K_{ZZ_1} & -K_{ZY_1} & (K_{ZZ_1} + K_{ZZ_2}) & K_{ZY_1} \\
-K_{YZ_1} & -K_{YY_1} & K_{YZ_1} & (K_{YY_1} + K_{YY_2})
\end{bmatrix}
\begin{Bmatrix}
Z_1 \\
Y_1 \\
Z_2 \\
Y_2
\end{Bmatrix}
=
\begin{Bmatrix}
0 \\
0 \\
0 \\
0
\end{Bmatrix}.
$$

This assumes that the bearing support/pedestal is essentially a beam undergoing bending and axial loading. The support itself offers very little additional damping, but it does have mass, and very high bending and axial stiffnesses. The bending and axial stiffnesses of the bearing support are uncoupled.

The foundation of a machine physically ties the bearing supports together, and as a result, the foundation causes the modelled structure or degrees of freedom to loop.
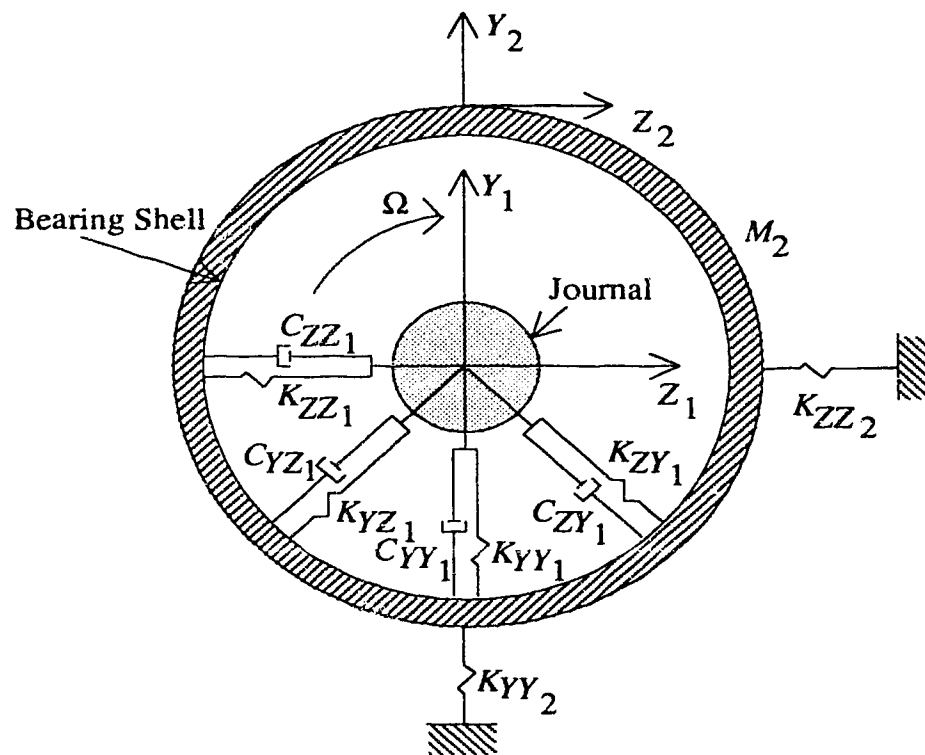
**FIGURE 4.7**: Bearing and Support Model

# 4.6 Conclusions

As has been discussed, hydrodynamic bearings and bearing supports can complicate the modelling of a rotor system considerably. The bearing coefficients are highly non-linear, and the coefficients and the rotor response are strongly interrelated. The model generally used is one of simple springs and viscous damping in both horizontal and vertical directions with some cross-coupling springs and damping as well. This model is valid only for calculating the dynamic characteristics and response of the rotor-bearing system in a very limited sense. Usually, the stiffness and damping matrices for a particular bearing are calculated for a particular load and shaft speed representing an intermediate value in the possible range. This is then used to evaluate the rotor response, and gives some idea of the expected rotor behavior.

Because no other model is presently available, the boundary conditions used in this work either model hydrodynamic bearings as given by Eq. (4.8), or the bearings are modelled as simple springs and damping as shown in Fig. 4.1.

# CHAPTER 5

# Continuous Coordinate Condensation

*All that glisters is not gold — Shakespeare*

## 5.1 Introduction

When calculating the critical speeds of machine shafts using the finite element method, one often needs to solve an eigenvalue problem. The solution of an eigenvalue problem of any significant size can be time consuming, and computational truncation can often lead to erroneous eigenvalues. Even with the use of static condensation, or component mode reduction, an eigenvalue problem still must be solved. This chapter introduces a new method of continuous coordinate condensation to reduce the matrix size, essentially combining the best features of the transfer matrix and the finite element methods.

Also, when examining the forced response of a structure, banded matrix solvers can be used to reduce computer memory or storage required. However, for branched or looped structures, such as a turbine-generator system with bearing supports and foundations included in the model, the global matrices may lose their bandedness, or the bandwidth may become quite large. The continuous coordinate condensation procedure presented allows the modelling of branched and looped structures while
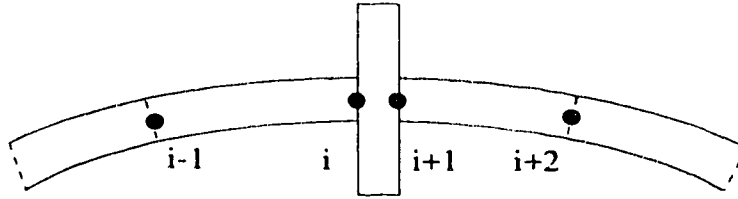
**FIGURE 5.1**: Transfer Matrix Method

maintaining a small matrix size.

With the transfer matrix method, the structure is discretized into sections of appropriate dimensions, as shown in Fig. 5.1. A state vector is defined which contains both the forces and the displacements at each end of the section. The state vectors at the opposite ends of a section are related using the principles of dynamics and strength of materials, resulting in a transfer matrix. Eq. (5.1) gives a sample matrix equation relating the state vector at node $i$ to that at node $i - 1$.

$$\left\{ \begin{array}{c} X \\ F \end{array} \right\}_i = [T_i] \left\{ \begin{array}{c} X \\ F \end{array} \right\}_{i-1} \tag{5.1}$$

The transfer matrix, $[T_i]$, relates the forces and displacements at one end of a discrete section to those at the other end. To model the whole structure, the transfer matrices for adjacent sections are pre-multiplied giving a single global transfer matrix for the entire structure. This global matrix is frequency dependent for problems of harmonic vibration, and has the same order as a single transfer matrix, even though it may represent the characteristics of several hundred discrete components. To find the natural frequency of the dynamic system, the natural and kinematic boundary conditions are applied at the ends of the structure reducing the order of the global transfer matrix, and the determinant of the reduced matrix is calculated. The determinant is iteratively calculated for a number of response frequencies, and a frequency which gives a zero value of the determinant represents

a natural frequency of the modelled system. The determinant being equal to zero is a requirement for satisfying the applied boundary conditions. The transfer matrix method is a matrix mathematics form of the Prohl-Myklestad method [26], which used a tabular procedure to arrive at the same natural frequencies. The disadvantage of the transfer matrix method is that for higher mode natural frequencies the determinant becomes the difference between two large numbers, and as a result, the higher mode natural frequencies cannot be accurately calculated.

The condensation method presented was first used in finite element modelling of acoustics (Craggs [27], and Christianson and Krenk [28]). Here, an application to shaft dynamics with the effect of gyroscopic moments and damping forces included is given (Eckert and Craggs [29], and Craggs and Eckert [30]). It uses finite elements to discretize the dynamic system, but, the elements are assembled into a condensed matrix that has the same order as a single element matrix, thereby combining the efficient computer storage of the transfer matrix method with the ability to calculate high mode natural frequencies of the finite element method.

Using the condensation procedure, the eigenvalues of a dynamic problem may be found by examining the forced harmonic response of a reduced finite element model. As each of the finite element matrices is assembled into the global matrices, the interconnecting nodal degrees of freedom are condensed out of the system. As a result, only the input and output nodes are retained, limiting the number of degrees of freedom of the global matrices to that of a single element of the model. However, this resulting superelement retains all the dynamic characteristics of the full finite element model. As with the transfer matrix method the condensation is performed iteratively for discrete forcing frequencies over the range of interest, and the resulting response to the input function clearly indicates the natural frequencies or critical speeds as well as giving an accurate estimate of the off resonant response. Both of these parameters are important in system identification as will be discussed in the next chapter.

## 5.2 Theory of Matrix Condensation

### 5.2.1 Simple Condensation

Let the structure of a dynamic system be modelled with discrete elements, and consider the equation of motion of a single element where damping and gyroscopic effects are ignored or are negligible. The equation of motion is:

$$[M]\{\ddot{q}\} + [K]\{q\} = \{f\}, \tag{5.2}$$

where $[M]$ and $[K]$ are the mass and stiffness matrices, and $\{q\}$ and $\{f\}$ are the general coordinate and forcing vectors of the element. Assuming a harmonic vibration of the element with a circular frequency of $\omega$, the dynamic matrix, $[D]$, can be defined as:

$$[D] = [K] - \omega^2[M]. \tag{5.3}$$

Now, consider two colinear elements that are chain assembled. The coordinates of the two element system can be defined as the input, center, and output coordinates (subscripted $i$, $c$, and $o$ respectively). The equation of motion of the two element system undergoing forced harmonic vibration can then be written in the following partitioned form:

$$\begin{bmatrix} D_{ii} & D_{ic} & D_{io} \\ D_{ci} & D_{cc} & D_{co} \\ D_{oi} & D_{oc} & D_{oo} \end{bmatrix} \begin{Bmatrix} Q_i \\ Q_c \\ Q_o \end{Bmatrix} = \begin{Bmatrix} F_i \\ 0 \\ F_o \end{Bmatrix}. \tag{5.4}$$

The matrices are normally in a banded form. That is, the output coordinates have no inertial or stiffness coupling to the input coordinates of the system. Therefore,

the banded equation of motion is given by Eq. (5.5).

$$
\begin{bmatrix}
D_{ii} & D_{ic} & 0 \\
D_{ci} & D_{cc} & D_{co} \\
0 & D_{oc} & D_{oo}
\end{bmatrix}
\begin{Bmatrix}
Q_i \\
Q_c \\
Q_o
\end{Bmatrix}
=
\begin{Bmatrix}
F_i \\
0 \\
F_o
\end{Bmatrix}
\tag{5.5}
$$

If the second equation of the matrix equation Eq. (5.5) is solved for the center coordinates, and assuming that no input forces exist at those coordinates then the center coordinates can be written in terms of the input and output coordinates.

$$
\{Q_c\} = -[D_{cc}]^{-1}([D_{ci}]\{Q_i\} + [D_{co}]\{Q_o\})
\tag{5.6}
$$

Substituting Eq. (5.6) back into the first and third equations of the matrix Eq. (5.5) results in the reduced equation of motion:

$$
\begin{bmatrix}
(D_{ii} - D_{ic}D_{cc}^{-1}D_{ci}) & (-D_{ic}D_{cc}^{-1}D_{co}) \\
(-D_{oc}D_{cc}^{-1}D_{ci}) & (D_{oo} - D_{oc}D_{cc}^{-1}D_{co})
\end{bmatrix}
\begin{Bmatrix}
Q_i \\
Q_o
\end{Bmatrix}
=
\begin{Bmatrix}
F_i \\
F_o
\end{Bmatrix}.
\tag{5.7}
$$

This reduced dynamic matrix for two elements can be considered to be the matrix of a superelement that retains the dynamic properties of the two elements at a particular forcing frequency. The total structure is modelled by assembling a single element to the model, and then performing the coordinate condensation procedure to give a new superelement dynamic matrix. When all the element dynamic matrices have been assembled and condensed into the reduced global dynamic system of the model, the corresponding response (at one of the retained coordinates) may be calculated. When this is performed iteratively over a forcing frequency range, and a response curve is plotted, the peak responses for an undamped system correspond to the natural frequencies of the system. A more accurate method for determining the

natural frequencies is the evaluation of the global dynamic matrix determinant. As with the transfer matrix method, when the determinant is zero, a natural frequency has been found. When damping is included, the response peaks and the phase of the response should also be plotted, or polar plots should be examined to find the critical frequencies.

If the frequency used is equal to the natural frequency of a subassembly of the total system, it is possible for the submatrix $[D_{cc}]$ to be singular. Normally, the forcing frequency will not be equal to a subsystem natural frequency exactly, but a small response peak may appear at values of the forcing frequency close to that natural frequency.

Using this method a superelement dynamic matrix that represents all the degrees of freedom of the model, but only being of the order of one element matrix can be used to model the entire system. The method is therefore very efficient in terms of the memory used to store the global dynamic matrix. However, some memory must also be set aside to store the individual element matrices, as they are used again for the condensation procedure for each forcing frequency calculated. But again, the memory to store the element matrices is a fraction of the memory needed to store the full assembled model. Also, storing the individual element matrices offers a computational speed advantage over reforming the element matrices for every forcing frequency.

This continuous coordinate condensation procedure produces a dynamic matrix that only has the beginning and final degrees of freedom available for inputting a force and calculating the response. If for instance, the user desires the placement of an input force, or the calculation of a response at an intermediate degree of freedom, then the condensation procedure must be modified somewhat. Instead of condensing the entire model into one superelement dynamic matrix, the system is broken into appropriate subcomponents with the interfaces occurring at the desired nodes. An example of a generic shaft system being modelled as subcomponents
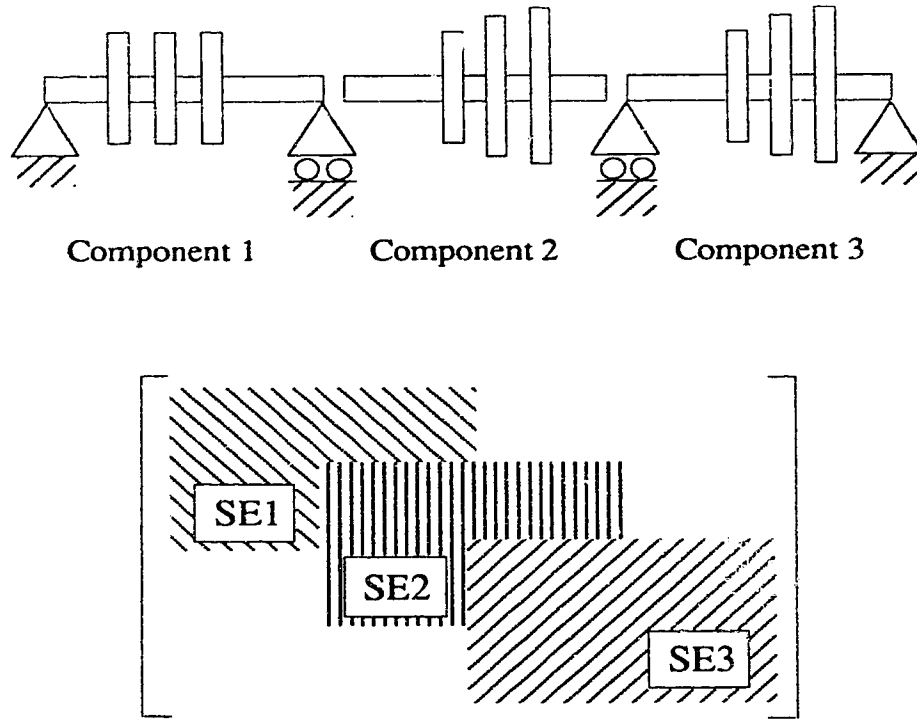
**FIGURE 5.2**: Shaft Modelled As Components

is shown in Fig. 5.2. The subcomponents are then condensed into superelement matrices for each component. The respective superelements are then assembled into a global dynamic matrix using the normal stiffness method (satisfying continuity at the interfaces). The resulting global matrix is then somewhat larger than for a single matrix, but the needed nodes and degrees of freedom are retained.

## 5.2.2 Condensation With Gyroscopic Effects

For a system that includes the gyroscopic effect of a spinning shaft undergoing angular displacement, the equation of motion is as follows:

$$[M]\{\ddot{q}\} + [G]\{\dot{q}\} + [K]\{q\} = \{f\}. \tag{5.8}$$

Eq. (5.8) can be expanded into two planes of vibration. as was done in Chapters 2 and 3, giving the equation of motion:

$$
\begin{bmatrix} M_{YY} & 0 \\ 0 & M_{ZZ} \end{bmatrix} \begin{Bmatrix} \ddot{q}_Y \\ \ddot{q}_Z \end{Bmatrix} + \begin{bmatrix} 0 & G(\Omega)_{YZ} \\ -G(\Omega)_{YZ} & 0 \end{bmatrix} \begin{Bmatrix} \dot{q}_Y \\ \dot{q}_Z \end{Bmatrix}
$$

$$
+ \begin{bmatrix} K_{YY} & 0 \\ 0 & K_{ZZ} \end{bmatrix} \begin{Bmatrix} q_Y \\ q_Z \end{Bmatrix} = \begin{Bmatrix} f_Y \\ f_Z \end{Bmatrix}. \tag{5.9}
$$

Assuming that the forcing function is a harmonic rotating force, and that the two planes of vibration are orthogonal, then the force vector can written as:

$$
\begin{Bmatrix} f_Y \\ f_Z \end{Bmatrix} = \begin{Bmatrix} F_Y \\ -jF_Z \end{Bmatrix} e^{j\omega t}. \tag{5.10}
$$

Also, assuming that the response vector is of the same form as the force vector, it can be written as:

$$
\begin{Bmatrix} q_Y \\ q_Z \end{Bmatrix} = \begin{Bmatrix} Q_Y \\ -jQ_Z \end{Bmatrix} e^{j\omega t}. \tag{5.11}
$$

The equation of motion, Eq. (5.9), can then be rewritten as:

$$
\left( \begin{bmatrix} K_{YY} & 0 \\ 0 & K_{ZZ} \end{bmatrix} - \omega^2 \begin{bmatrix} M_{YY} & 0 \\ 0 & M_{ZZ} \end{bmatrix} \right.
$$

$$
\left. +\omega \begin{bmatrix} 0 & G(\Omega)_{YZ} \\ G(\Omega)_{YZ} & 0 \end{bmatrix} \right) \begin{Bmatrix} Q_Y \\ Q_Z \end{Bmatrix} = \begin{Bmatrix} F_Y \\ F_Z \end{Bmatrix}. \tag{5.12}
$$

Now in Eq. (5.12), the gyroscopic matrix is symmetric and the whole equation is real. This allows the response to be solved without complex algebra. The dynamic matrix for the gyroscopic system is the term in brackets in Eq. (5.12), and is:

$$[D] = [K] - \omega^2[M] + \omega[G].$$ (5.13)

### 5.2.3 Condensation With Damping

When damping is included, the forced response solution to the equation of motion can no longer be reduced to a purely real equation, and therefore the problem must be solved using complex algebra. The full equation of motion including damping and gyroscopic effects can be written as:

$$[M]\{\ddot{q}\} + ([G] + [C])\{\dot{q}\} + [K]\{q\} = \{f\}.$$ (5.14)

Assuming an arbitrary harmonic forcing function vector and response vector, both with complex amplitudes, as shown:

$$\{f\} = (\{F\}_\Re + j\,\{F\}_\Im)e^{j\omega t}$$ (5.15)

$$\{q\} = (\{Q\}_\Re + j\,\{Q\}_\Im)e^{j\omega t},$$ (5.16)

the equation of motion can be written as:

$$\Big(([K] - \omega^2[M]) + j([G] + [C])\Big)(\{Q\}_\Re + j\,\{Q\}_\Im) = \{F\}_\Re + j\,\{F\}_\Im.$$ (5.17)

Let $[A] = [K] - \omega^2[M]$ and $[B] = [G] + [C]$, which are the real and imaginary matrices respectively, and then collect real and imaginary terms to arrive at:

$$\begin{bmatrix} [A] & -[B] \\ [B] & [A] \end{bmatrix} \left\{ \begin{array}{c} \{Q\}_\Re \\ \{Q\}_\Im \end{array} \right\} = \left\{ \begin{array}{c} \{F\}_\Re \\ \{F\}_\Im \end{array} \right\} . \tag{5.18}$$

The matrix in Eq. (5.18) is now the dynamic matrix for the system with damping, and the system of equations is now real, albeit with a dynamic matrix of twice the degrees of freedom of $[A]$ or $[B]$. The system response to a input force can be calculated with an algorithm for the solution of a set of real linear equations, such as Gaussian elimination.

As with the undamped case the center coordinates of the two elements to be condensed are solved for in terms of the input and output coordinates. But in this case the center coordinates consist of real and imaginary components, i.e. $\{Q_c\}_\Re$ and $\{Q_c\}_\Im$. The real and imaginary input and output responses are coupled by the damping terms and hence the phase between the input force and response may be any value between 0 and 360 degrees.

## 5.3  Results

In this section results of quantitative tests of the continuous coordinate condensation method are given.

An uniform steel beam with simple supports was modelled as shown in Fig. 5.3. The response of the beam to a forced harmonic input with a frequency range of 0 to 25000 CPM was calculated using 4, 16, and 512 elements condensed to one superelement using continuous coordinate condensation. The response measured was the angular displacement of the beam neutral axis at the right hand support, and the calculated curves are shown in Fig. 5.4. The three cases gave the same first three peak responses, with the fourth peak response frequency for the 4 element

$E = 30 \times 10^6$ psi., $\rho = 0.283$ lbs./in.$^3$, $\nu = 0.30$
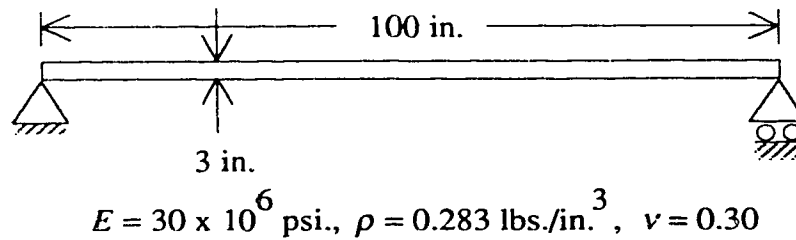
**FIGURE 5.3**: Simply Supported Beam Model

model being too high to appear on the plot. The condensation procedure therefore behaved as the full finite element model would. That is, as more elements were condensed into the model the natural frequencies (response peaks) converged to lower values. However, the 512 element condensed model did not predict the lowest peak response. This occurred because each individual element was so short that differences between numerical magnitudes of the element stiffness and mass matrices caused significant round-off error. When the forcing frequency was set to a high enough value for the difference in magnitude to become less significant, the round-off error was negligible. That is an opposite situation to a full matrix finite element solution technique, where using more elements would refine the solution; with the condensation procedure, however, using more elements does refine the solution to a certain point. Beyond that, increasing the number of elements is counterproductive in both computational time and accuracy. Unlike the transfer matrix method however, the condensed finite element method can be used to predict higher natural frequencies of a system.

The actual peak frequency values for a 32 element model of the uniform beam using the condensation method, and the full matrix eigensolution method (Jacobi's) are compared in Table 5.1. The continuous coordinate condensation procedure natural frequencies agree well with those from the full matrix eigenvalue solution.

An uniform cantilevered steel beam, as shown in Fig. 5.5, was modelled to demonstrate the method with different boundary conditions. The response of the
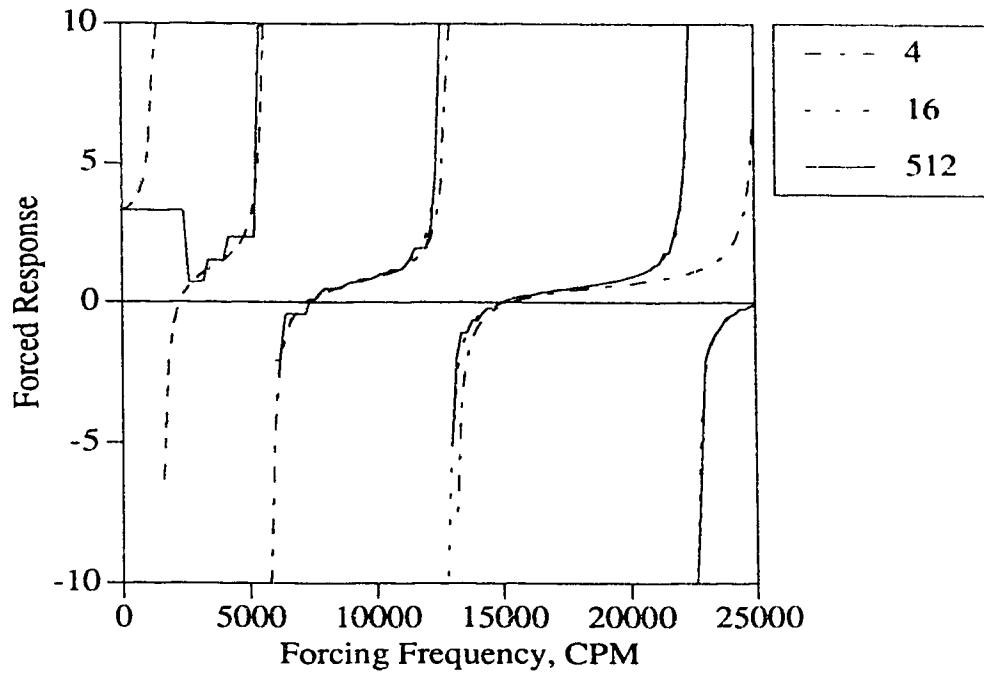
**FIGURE 5.4**: Simply Supported Beam Response

**TABLE 5.1**: Natural Frequencies of Simply Supported Beam

| Mode | Continuous Coordinate Condensation (32 el.) Peak Resonance (CPM) | Full Matrix Solution Using Jacobi's Method (CPM) |
|------|------|------|
| 1 | 1428 | 1429 |
| 2 | 5698 | 5697 |
| 3 | 12750 | 12751 |
| 4 | 22499 | 22508 |

$$E = 30 \times 10^6 \text{ psi.}, \quad \rho = 0.283 \text{ lbs./in.}^3, \quad \nu = 0.30$$



100 in.

3 in.
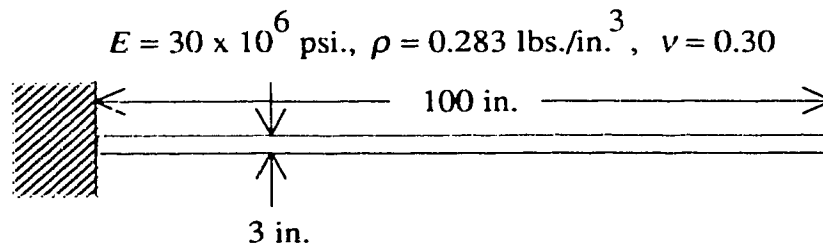
**FIGURE 5.5**: Cantilevered Beam Model

**TABLE 5.2**: Natural Frequencies of Cantilevered Beam

| Mode | Continuous Coordinate Condensation (32 el.) Peak Resonance (CPM) | Full Matrix Solution Using Jacobi's Method (CPM) |
|------|------|------|
| 1 | 517 | 509 |
| 2 | 3183 | 3182 |
| 3 | 8864 | 8867 |
| 4 | 17244 | 17256 |

beam to a harmonic force with a frequency range of 0 to 20000 CPM was calculated for 2, 128, and 512 condensed elements, with the responses measured being the lateral displacement of the free end, and the resultant curves are shown in Fig. 5.6. Again, the frequency peaks converged to lower values as the number of condensed elements in the model was increased. As in the previous case, the 512 element model was inaccurate at the lower forcing frequencies, and the 16 or 32 element model was more than sufficient in terms of accuracy. The numerical values of the first four frequency peaks for a 32 element model calculated with the normal full eigensolution and the condensation method are compared in Table 5.2. Again, there was excellent agreement between the two methods.
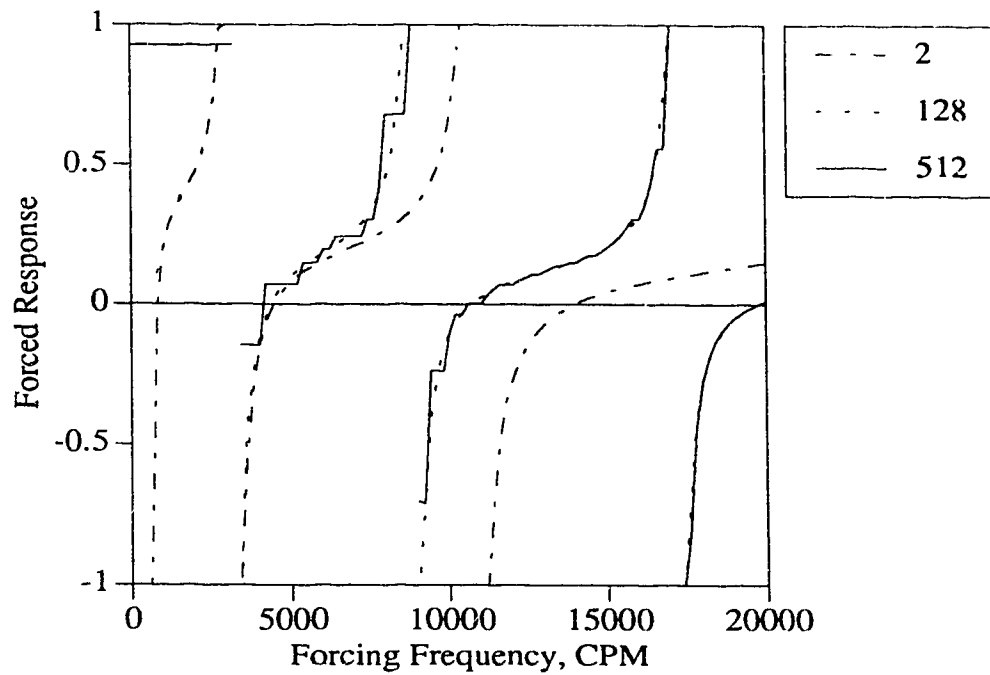
**FIGURE 5.6**: Cantilevered Beam Response



$E = 30 \times 10^6$ psi., $\rho = 0.283$ lbs./in.$^3$, $v = 0.30$
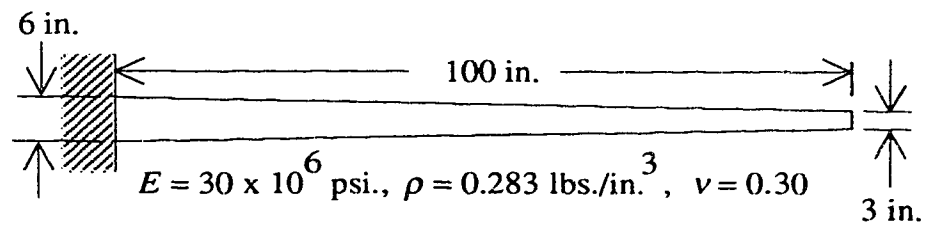
**FIGURE 5.7**: Tapered Beam Model
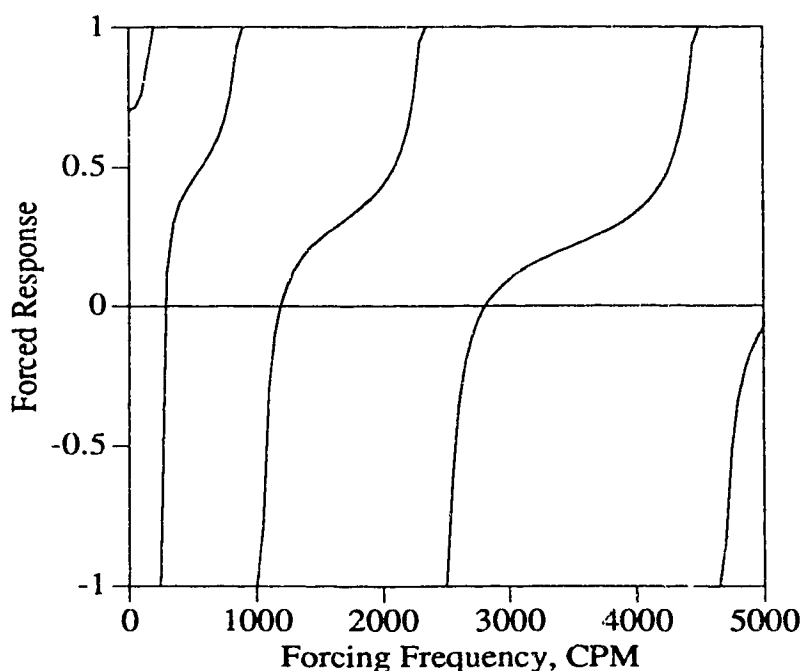
**FIGURE 5.8**: Tapered Beam Response

A tapered cantilevered steel beam shown in Fig. 5.7 was modelled using twenty condensed tapered beam elements. The response curve is shown in Fig. 5.8, and the numerical values for the natural frequencies using the full eigenvalue solution and the condensation method are given in Table 5.3. Again, excellent agreement between the two methods is evident.

To demonstrate the ability of the method to calculate the natural frequencies of a system with subcomponents, the beam in Fig. 5.9 was modelled in three subcomponents with each containing an equal number of condensed elements. The response curves were calculated with 2, 4, and 32 beam elements condensed into one subcomponent superelement, and are shown in Fig. 5.10. The curves for the 4 and 32 element models are nearly indistinguishable for forcing frequencies less than 3500 CPM. The natural frequencies are given in Table 5.4 for the case of subcomponents modelled with 32 elements each. The frequencies were calculated

**TABLE 5.3**: Natural Frequencies of Tapered Beam

| Mode | Continuous Coordinate Condensation Peak Resonance (CPM) | Full Matrix Solution Using Jacobi's Method (CPM) |
|------|---------------------------------------------------------|--------------------------------------------------|
| 1 | 233 | 239 |
| 2 | 982 | 983 |
| 3 | 2437 | 2436 |
| 4 | 4593 | 4590 |

with three different methods. First, the three subcomponents were condensed into one superelement dynamic matrix each, and then the superelements were assembled using the normal stiffness method for a total of 8 retained degrees of freedom. The natural frequencies were found by seeking the peak responses for a forced vibration. Second, the superelements were again formed, but were then condensed together also for a global dynamic matrix of 4 degrees of freedom, and the peak responses were examined. And third, the full matrix eigenvalue solution was performed with all 194 degrees of freedom. The numeric values given in Table 5.4 show excellent agreement between all three methods. The condensation method gave excellent results with a saving in computer memory and computational time required. The fully condensed model only required storage of 'ement stiffness and mass matrix, and a global dynamic matrix of the same siz( ( DOF), while the full matrix solution required storage of global stiffness and mass matrices of 194 DOF. The solution time for the fully condensed system was less than half of the time required for the full matrix system.

The previous models have been simple beam systems. When modelling shafts, vibration in two perpendicular planes is allowed, and if the shaft rotates, the angular displacement of the shaft sections and disks introduce gyroscopic effects into the

$$E = 30 \times 10^6 \text{ psi.}, \quad \rho = 0.283 \text{ lbs./in.}^3, \quad \nu = 0.30$$
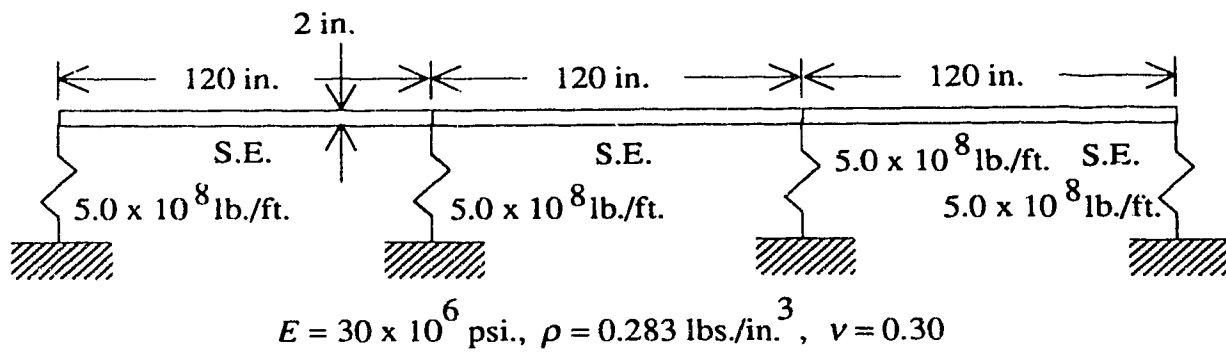
FIGURE 5.9: Superelement Model
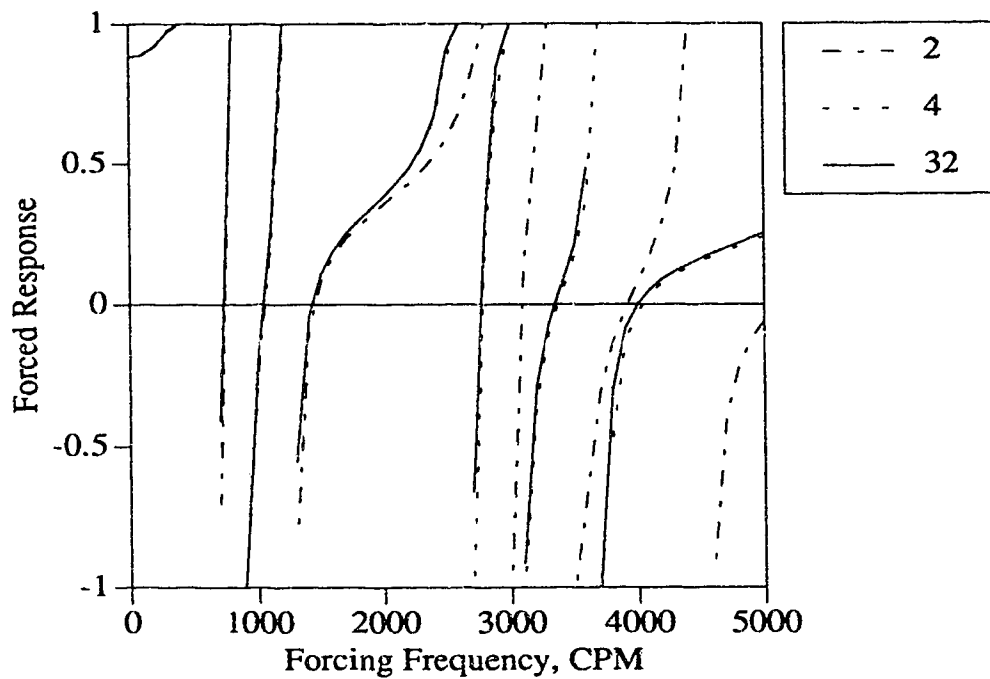


FIGURE 5.10: Superelement Response

**TABLE 5.4**: Natural Frequencies of Assembled Superelement Beam

| Mode | Cont. Coord. Condensation Peak Resonance Assembled S.E. (CPM) | Cont. Coord. Condensation Peak Resonance (CPM) | Full Matrix Solution Using Jacobi's Method (CPM) |
|------|------|------|------|
| 1 | 664 | 663 | 662 |
| 2 | 844 | 838 | 845 |
| 3 | 1239 | 1238 | 1238 |
| 4 | 2645 | 2638 | 2646 |
| 5 | 3014 | 3012 | 3013 |
| 6 | 3693 | 3688 | 3695 |

dynamic characteristics of the shaft. If the shaft is not spinning, and the shaft and support stiffnesses are isotropic, then the shaft natural frequencies in either plane are equal to those of a beam vibrating in one plane. A full matrix eigenvalue routine will give two pairs of natural frequencies; one pair for each plane and all four values will be the same for zero rotation speed. However, as the shaft speed is increased the eigenvalues split into two pairs of different values. The lower value will be the natural frequency of the shaft in the backward whirl mode. That is, for an overhung shaft with a disk at the free end, the shaft and disk will precess or whirl in an orbit opposite to the shaft rotation. The higher value is the natural frequency of the shaft in the forward whirl mode, where the disk precesses in the direction of shaft rotation. Again, for the isotropic case, the pairs of values calculated will be the same for both planes. The gyroscopic matrix is skew-symmetric, and as a result the full matrix solution of the eigenvalue problem must be solved using a non-symmetric method such as the Householder-QR method.

To show that the continuous coordinate condensation method would excite and find both forward and backward critical speeds of a shaft, an overhung disk was

$$E = 30 \times 10^6 \text{ psi.}, \quad \rho = 0.283 \text{ lbs./in.}^3, \quad \nu = 0.30$$
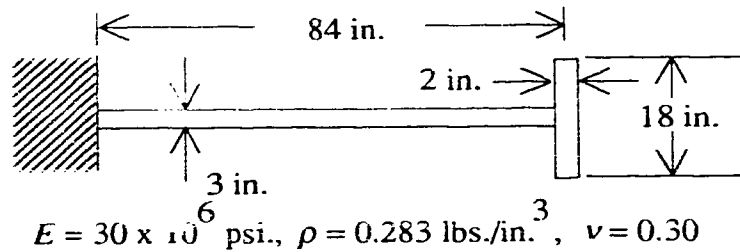
**FIGURE 5.11:** Overhung Shaft Model

modelled as shown in Fig. 5.11. The model consisted of seven Timoshenko shaft elements each twelve inches in length, and a disk was added to the free end. The entire model was condensed to one superelement dynamic matrix with the forcing function being applied to the retained angular displacement degree of freedom at the free end. The response was also measured at this point. The condensed peak response frequencies (whirl speeds) are shown in Fig. 5.12 and compared to the whirl speeds calculated from the full matrix model using the Householder-QR method. The speeds calculated with the condensation procedure are shown as discrete points marked by hollow circles and squares, while the full matrix solution speeds are given as continuous solid and dashed lines. As the figure shows, the zero shaft rotation speed split into forward and backward whirl speeds, and the values matched the full solution values almost exactly. The lowest whirl speed did not appear to split into forward and backward modes only because of the scale of the plot.

The responses for the overhung shaft to a range of forcing frequencies for a shaft rotation speed of 0 and 2000 RPM is also shown in Fig. 5.13. The response plotted was the lateral displacement of the disk center. Again, the zero shaft speed resulted in single response peaks or natural frequencies. Setting the shaft rotation speed to 2000 RPM split those peaks into pairs of peaks that straddled the zero speed peaks. The effect was most apparent at the higher forcing frequencies, and is exactly what is predicted by theory.
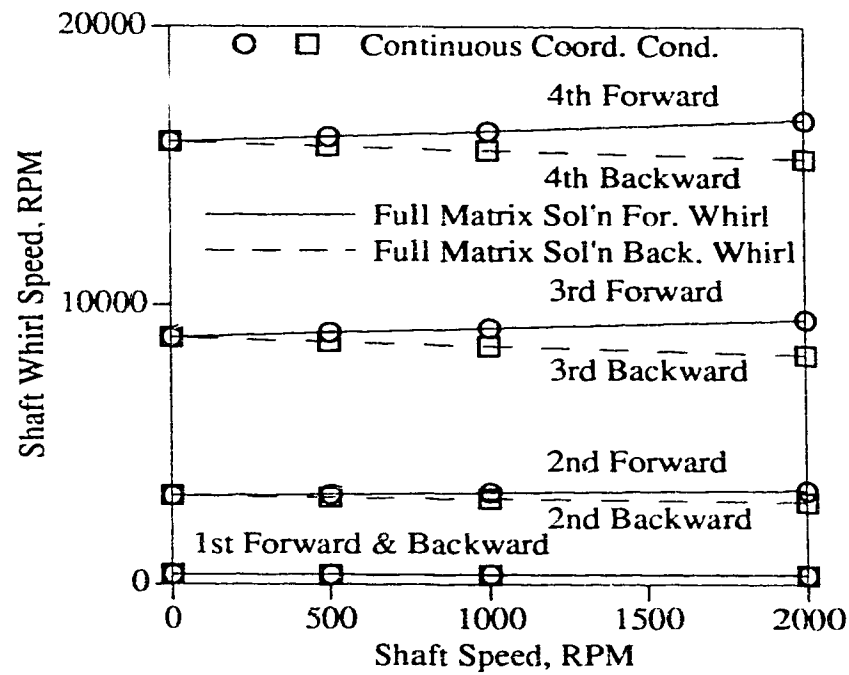
**FIGURE 5.12**: Whirl Speeds of Overhung Shaft
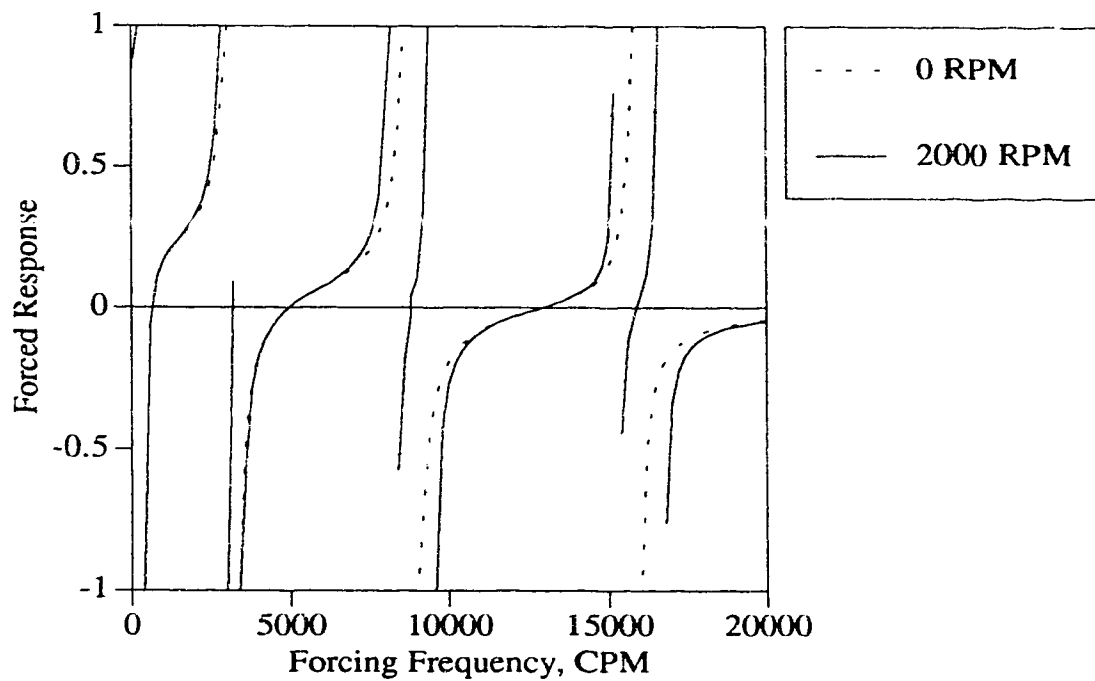


**FIGURE 5.13**: Overhung Shaft Response

**FIGURE 5.14**: Prohl Rotor



$$E = 29 \times 10^{6}\text{psi.}, \quad \rho = 0.283 \text{ lbs./in.}^{3}, \quad v = 0.30$$
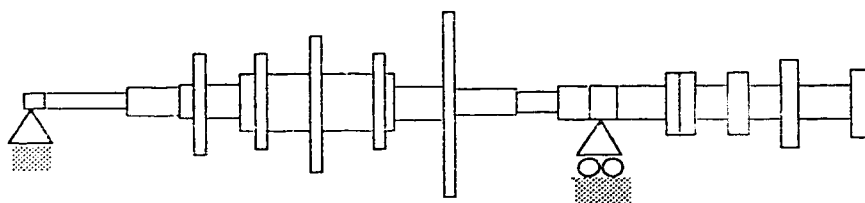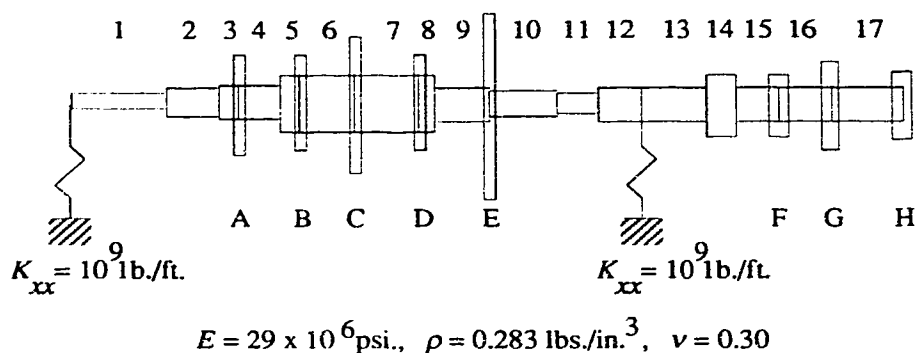
**FIGURE 5.15**: Prohl Rotor Finite Element Model

The continuous coordinate condensation procedure therefore, will excite forward and backward whirl modes, and can be used to predict both. Although, in real situations the backward whirl mode can only be excited if the stiffnesses of the shaft or bearings are not isotropic. The calculation procedure will give both modes because the forcing function used is general, and the input and direction can be specified by the analyst to give the responses sought.

The Prohl [26] rotor, as shown in Fig. 5.14, was also modelled with the condensation method. The seventeen Timoshenko shaft element model is shown in Fig. 5.15, and the element and disk dimensions are given in Table Table 5.5. Young's modulus was 30 × 10⁶, density was 0.283 lb./cu.in., and Poisson's ratio was 0.30. The model was again condensed to one superelement, with the response measured and the forcing function applied at the translational degree of freedom at the right end in the vertical plane, and the response curves for shaft speeds of 0

**TABLE 5.5**: Prohl Rotor Element Dimensions

| Elem. No. | Len. in. | Dia. in. | Elem. No. | Len. in. | Dia. in. |
|---|---|---|---|---|---|
| 1 | 8.13 | 1.66 | 10 | 6.13 | 2.19 |
| 2 | 3.63 | 2.06 | 11 | 2.38 | 2.00 |
| 3 | 1.56 | 2.34 | 12 | 3.69 | 2.19 |
| 4 | 3.63 | 2.34 | 13 | 4.25 | 2.19 |
| 5 | 1.59 | 5.78 | 14 | 2.00 | 4.94 |
| 6 | 5.29 | 5.78 | 15 | 3.81 | 2.19 |
| 7 | 5.25 | 5.78 | 16 | 4.25 | 2.19 |
| 8 | 0.75 | 5.78 | 17 | 5.56 | 2.19 |
| 9 | 4.25 | 2.34 | | | |
| Disk No. | Dia. in. | Thick. in. | Disk No. | Dia. in. | Thick. in. |
| A | 9.63 | 0.63 | E | 16.78 | 0.50 |
| B | 9.45 | 0.63 | F | 5.75 | 1.25 |
| C | 12.42 | 0.63 | G | 7.41 | 1.00 |
| D | 9.45 | 0.63 | H | 6.03 | 1.00 |

RPM (Fig. 5.16) and 11780 RPM (Fig. 5.17) are given. The 0 RPM response curve was very clean, and the peak responses and frequencies were easily determined. The response curve for 11780 RPM was much less smooth, and a number of additional peaks appeared. Off resonant responses, unfortunately, cluttered the response curve. To find the peak responses, the analyst must carefully determine the proper force input nodes, and desired response nodes to reduce the influence of unwanted modes.

The critical speeds of the shaft are given in Table 5.6 for the condensation method, and for Prohl's published results. Prohl calculated the critical speeds using a tabular form of the transfer matrix method. Again, the results agreed fairly well, although some differences were apparent. Since Prohl did not supply all the disk dimensions in his paper some of the diameters were estimated, and this is the most probable source of error.

A damped model with gyroscopic effects was also tested, as shown in Fig. 5.18.
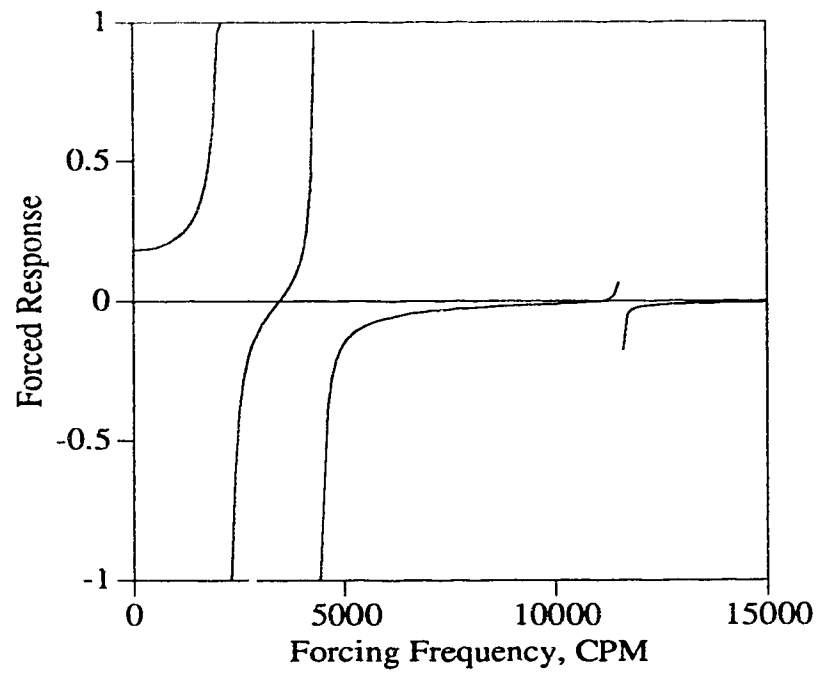
**FIGURE 5.16**: Prohl Rotor Response at 0 RPM
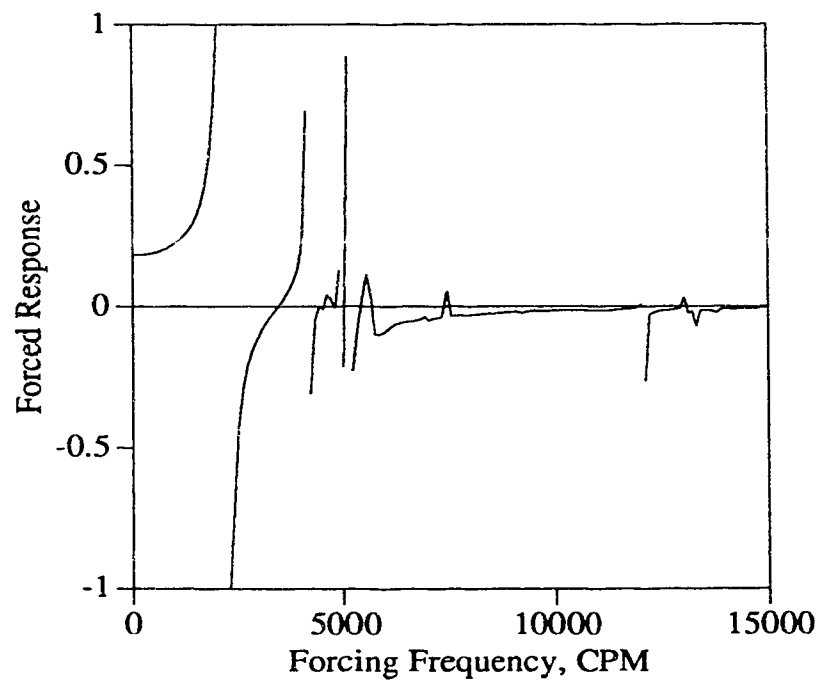


**FIGURE 5.17**: Prohl Rotor Response at 11780 RPM

**TABLE 5.6**: Critical Speeds of the Prohl Rotor

| Mode | Continuous Coordinate Condensation Peak Resonance (CPM) | Natural Frequency Using Prohl's Method (CPM) |
|---|---|---|
| 1 | 2200 | 2230 |
| 2 | 4400 | 4230 |
| 3 | 11600 | 11790 |

The model of the overhung shaft included the translational stiffnesses and damping of a hydrodynamic bearing. The rotational stiffnesses of the bearing were set very high to effectively clamp the angular degrees of freedom at the bearing, and no angular damping was included. The bearing translational stiffnesses and damping were as shown below.

$$[K] = \begin{bmatrix} 2.54 \times 10^6 & 2.54 \times 10^4 \\ 2.54 \times 10^4 & 7.62 \times 10^6 \end{bmatrix} \frac{lb.}{ft.}$$

$$[C] = \begin{bmatrix} 63.5 & 93.1 \\ 93.1 & 360.0 \end{bmatrix} \frac{lb. - sec.}{ft.}$$

The overhung shaft model was rotating at a speed of 2000 RPM, and therefore included gyroscopic effects as well as damping. The forced response of the shaft was first calculated using the full global matrices, and the response at the disk end of the shaft in the horizontal plane was plotted. A Bode plot (magnitude and phase of response) for a forcing frequency range of 0 to 5000 RPM is given in Fig. 5.19. The gyroscopic effect of the disk split the natural frequency peak into two distinct peaks, one at 2675 RPM and the other at 3050 RPM. A polar plot for the

$$E = 30 \times 10^6 \text{ psi.,} \quad \rho = 0.283 \text{ lbs./in.}^3, \quad v = 0.30$$
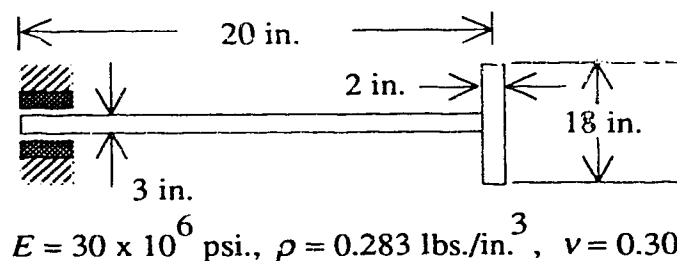
**FIGURE 5.18**: Damped Overhung Model

full matrix solution is also shown in Fig. 5.20. Again the two natural frequencies can be seen as two connected loops. The forced response using the continuous coordinate condensation procedure is shown in Fig. 5.21 and Fig. 5.22. The curves were identical to those derived from the full matrix solution, and the solution time for the condensation procedure was only 50% of the computer time needed for the full solution.

A more complex machine shaft model was tested as shown in Fig. 5.23. The steel model consisted of a three span machine supported on four journal bearings. The bearing loads were found by forming a finite element model of the shaft with Timoshenko beam elements and added disks, and then calculating the static reaction loads on very stiff supports at the bearing positions. The resultant loads were then used to calculate the bearing stiffness and damping coefficients from the data given in [23]. Unfortunately, the damping coefficients produced in this manner resulted in an overdamped system. Subsequently, the model was modified and run with the damping coefficients at the bearings being divided by one hundred, and are tabulated in Table 5.7. An additional case, where the bearing damping matrices were ten times those given in Table 5.7 was also run. This still resulted in a heavily damped rotor, and the results are given later. In both cases, the running speed of the machine was 1800 RPM, and the first span of the machine was modelled with four elements of eighteen inches length, the second span with four elements
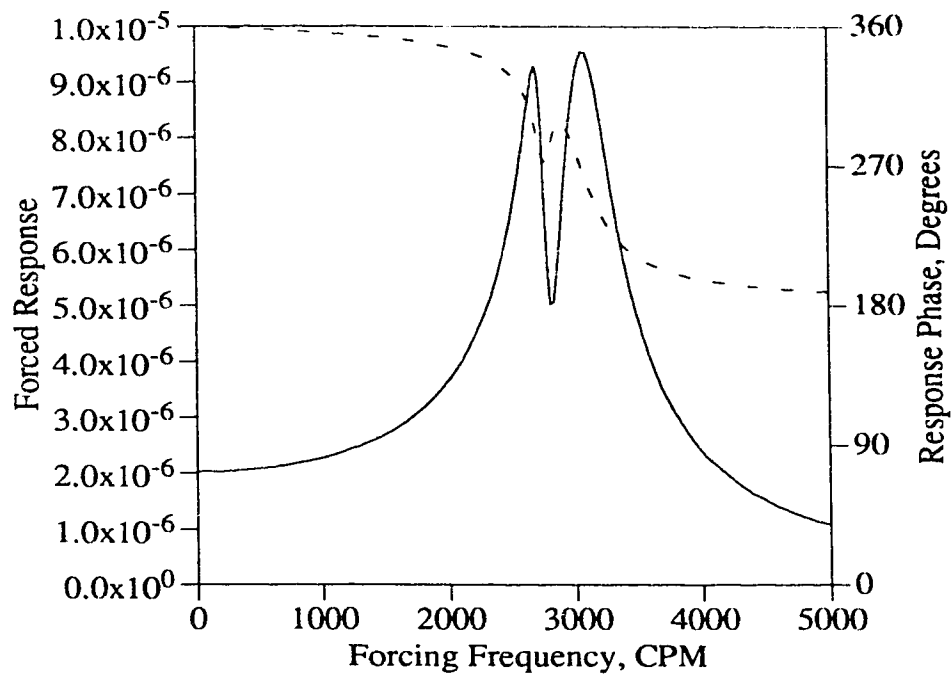
FIGURE 5.19: Full Matrix Bode Plot
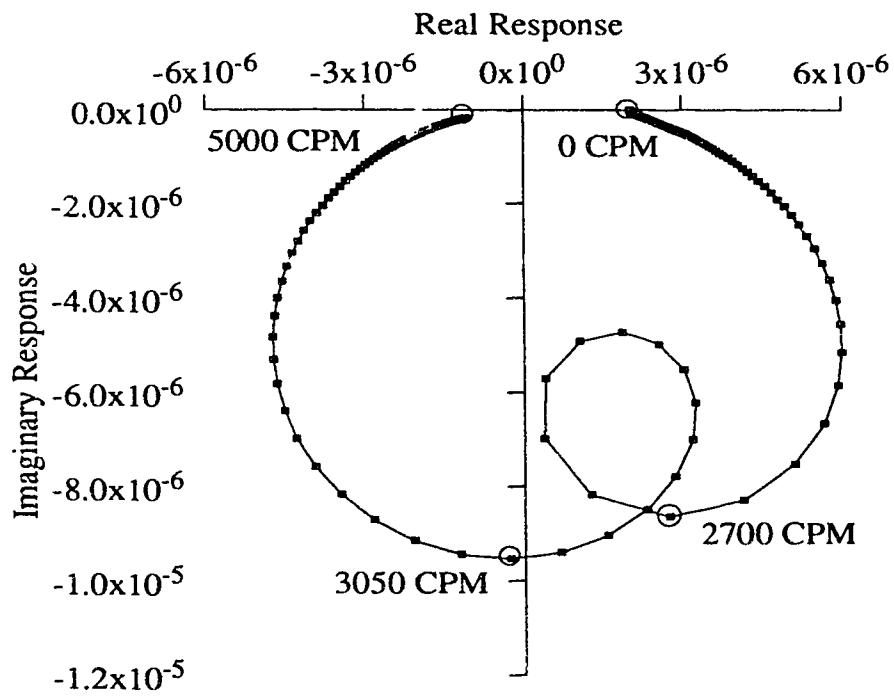


FIGURE 5.20: Full Matrix Polar Plot
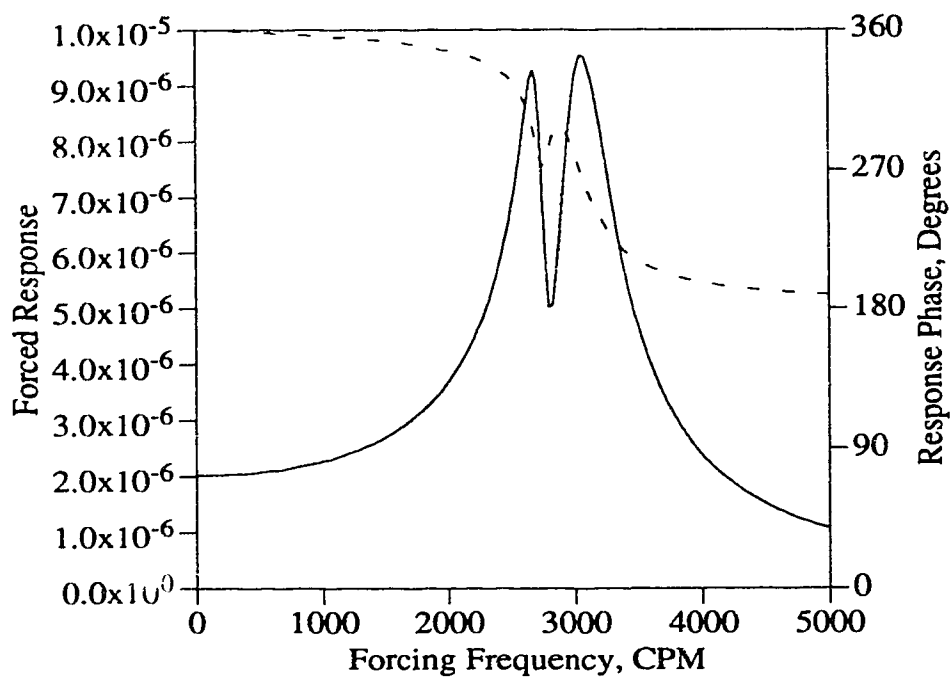
FIGURE 5.21: Condensed Matrix Bode Plot
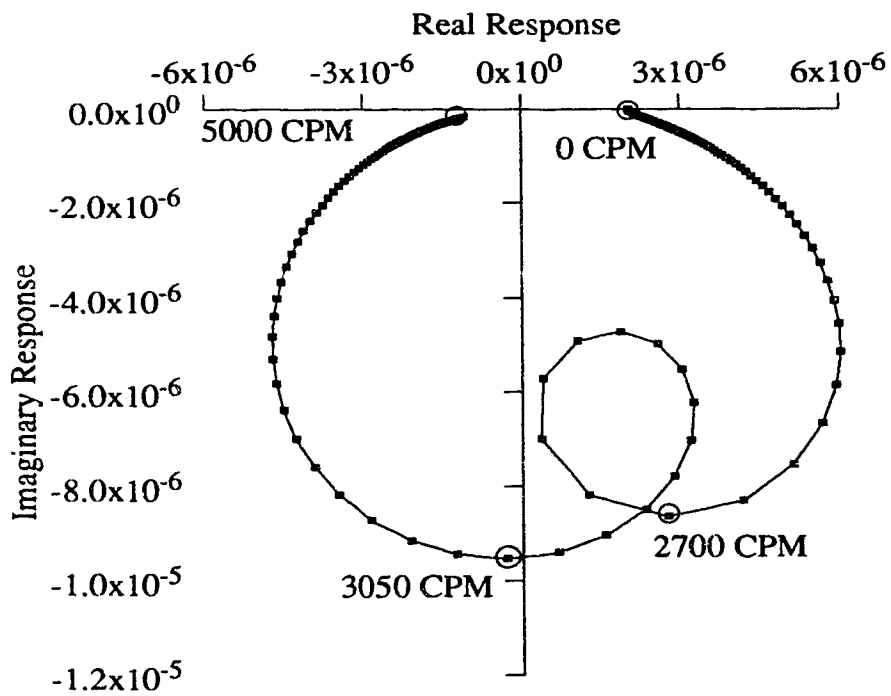


FIGURE 5.22: Condensed Matrix Polar Plot

**TABLE 5.7**: Bearing Coefficients of Machine Model

| Bearing | Load lb. | Stiffness Matrix $\times 10^6$ lb./ft. | Damping Matrix lb.-sec./ft. |
|---------|----------|----------------------------------------|------------------------------|
| A | 148.8 | $\begin{bmatrix} 1.250 & -0.476 \\ 2.380 & 1.786 \end{bmatrix}$ | $\begin{bmatrix} 78.96 & 63.17 \\ 63.17 & 221.10 \end{bmatrix}$ |
| B | 491.8 | $\begin{bmatrix} 3.541 & 0.590 \\ 7.869 & 12.79 \end{bmatrix}$ | $\begin{bmatrix} 156.60 & 219.20 \\ 219.20 & 834.90 \end{bmatrix}$ |
| C | 366.1 | $\begin{bmatrix} 2.636 & .0293 \\ 5.857 & 8.054 \end{bmatrix}$ | $\begin{bmatrix} 139.80 & 163.10 \\ 163.10 & 621.48 \end{bmatrix}$ |
| D | 118.3 | $\begin{bmatrix} 1.040 & -0.520 \\ 1.703 & 1.371 \end{bmatrix}$ | $\begin{bmatrix} 70.26 & 52.70 \\ 52.70 & 180.70 \end{bmatrix}$ |

Cylindrical bearings with 2 axial grooves, N= 1800 rpm, $\mu = 2.88 \times 10^{-4}$ lb.-sec./ft$^2$, $C_p = 0.003$ in., and L/D= 0.5.

of twenty-four inches length, and the third span with five elements of thirty inches length.

Fig. 5.24 shows the Bode plot for the vertical plane of the machine without damping, and not rotating. The forcing function was input at the node in the center span as shown in the model diagram, and response measured at the node in the third span. Also shown in Fig. 5.25 are the first three undamped modes of the machine. As is typical of large turbogenerator sets, the first mode consists primarily of motion in the generator section (right-most span), while the second and third modes excite the high pressure and low pressure turbine sections respectively (middle and left-most spans). The natural frequencies for the undamped non-rotating shaft in the vertical plane were: 778, 1283, 2121, and 2747 CPM.

Fig. 5.26 shows the polar plot for the damped machine calculated using the condensation technique, for a forcing frequency that was varied from 0 to 3000

72 in.

96 in.

150 in.

18 in.

24 in.

30 in.

20 in.

24 in.

A

B

C

Response Node

D

Force Input Node

2 in.

2.5 in.

3 in.

$$E = 30 \times 10^6 \text{ psi.}, \quad \rho = 0.283 \text{ lbs./in.}^3, \quad \nu = 0.30$$
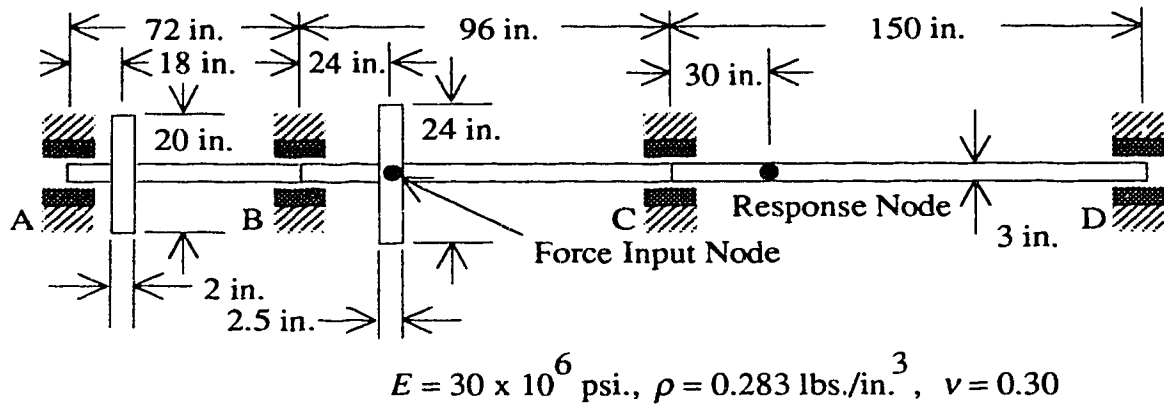
FIGURE 5.23: Machine with Bearings

2.5x10⁻³ — 360

2.0x10⁻³ — 270

1.5x10⁻³ — 180

1.0x10⁻³ — 90

5.0x10⁻⁴

0.0x10⁰ — 0

Forced Response

Response Phase, Degrees

0    1000    2000    3000

Forcing Frequency, CPM
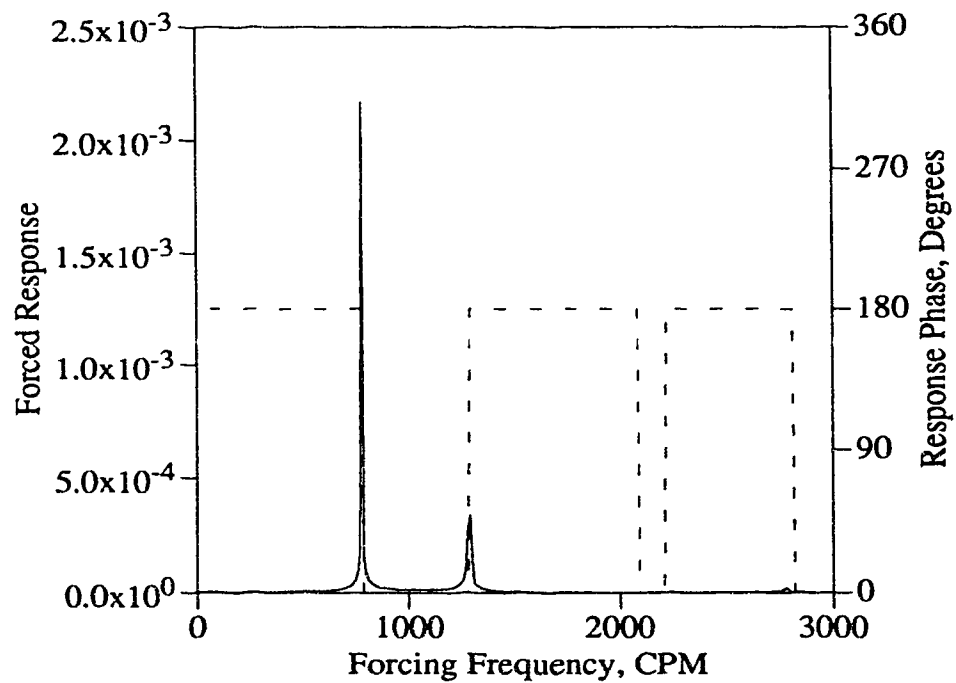
FIGURE 5.24: Undamped Bode Plot
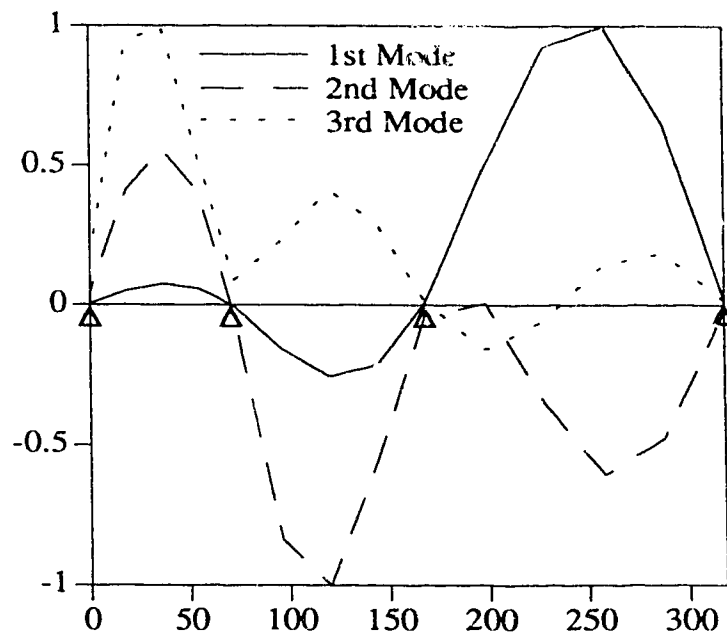
**FIGURE 5.25**: Undamped Mode Shapes
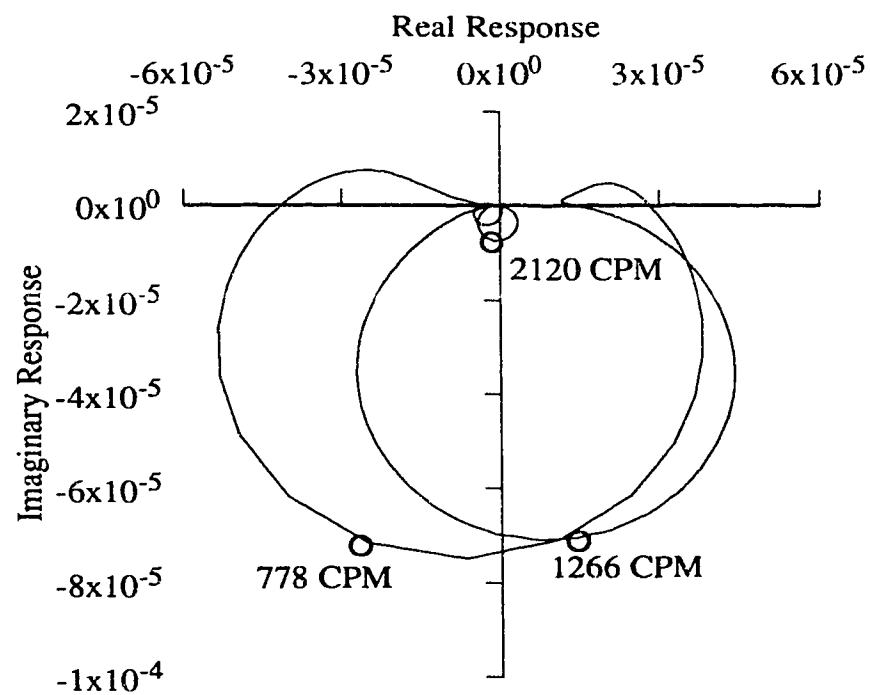


**FIGURE 5.26**: Damped Machine Polar Plot For All Modes
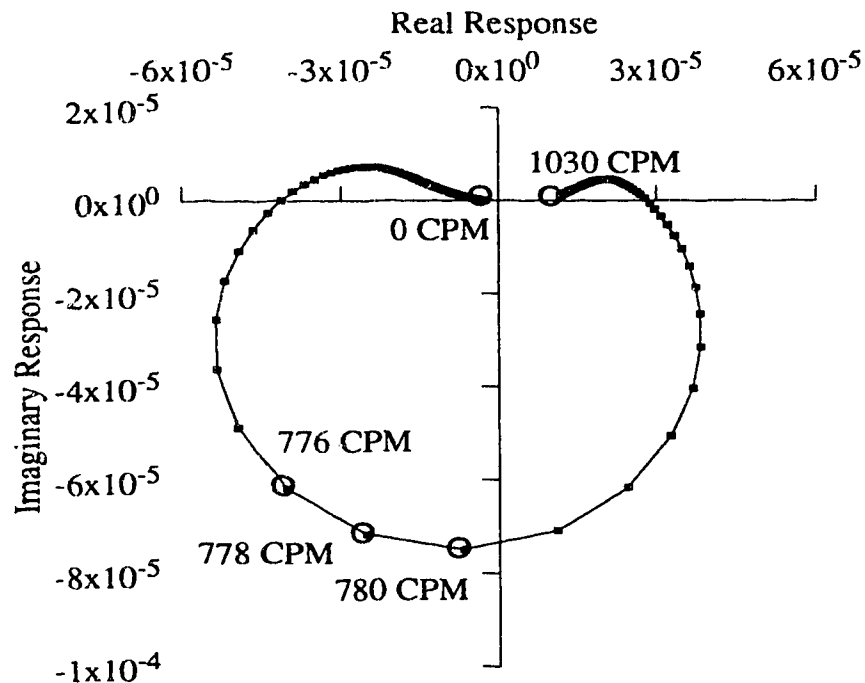
**FIGURE 5.27**: Damped Machine Polar Plot For First Mode

CPM, and covered the first five natural frequencies of the machine. The damping coefficients for this model were as given in Table 5.7. The plot displays the response of the machine with light damping and rotating at 1800 RPM, and the damped natural frequencies with gyroscopic effects included were: 778, 1266, 2120, 2752, and 2870 CPM.

Shown in Fig. 5.27, is the polar plot for the first natural frequency, which was the largest diameter loop in Fig. 5.26. The damped natural frequency of the shaft occurred between 778 and 780 CPM, because this step change in frequency resulted in the largest arc of the circle being drawn. The damped natural frequency was found by locating the frequency interval that resulted in the largest change in phase, which is equivalent to the largest arc of the circle. Note that the maximum response magnitude does not necessarily occur at the damped natural frequency. As well, the point at which the curve crosses the imaginary axis (real component is zero) is
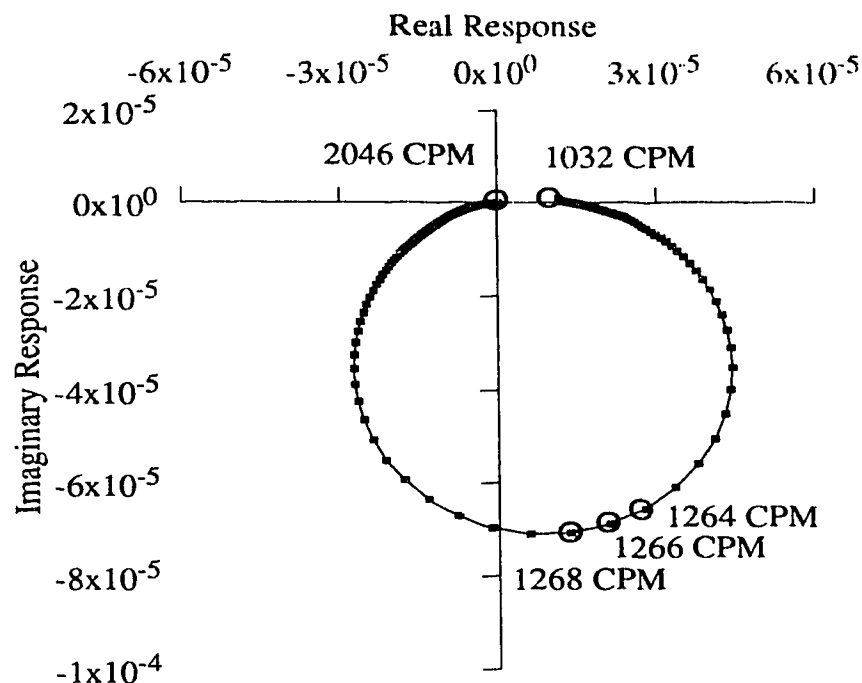
**FIGURE 5.28**: Damped Machine Polar Plot For Second Mode

the undamped natural frequency of the rotor. The fact that this circle had portions of its arc above the imaginary axis indicates that some additional residual response from the other modes was present.

Fig. 5.28 is the second natural frequency polar plot, which had a response amplitude slightly smaller than that of the first natural frequency. The residual contribution from the other modes was considerably smaller than for the first mode. The damped natural frequency was approximately 1266 CPM.

The response curve shown in Fig. 5.29, was for damping coefficients which were ten times those in Table 5.7, and the peaks were very broad and the first natural frequency almost disappeared into the second peak. This also can be seen in Fig. 5.30 where the first resonant loop of the polar plot was incomplete. This indicates that the machine was heavily damped.
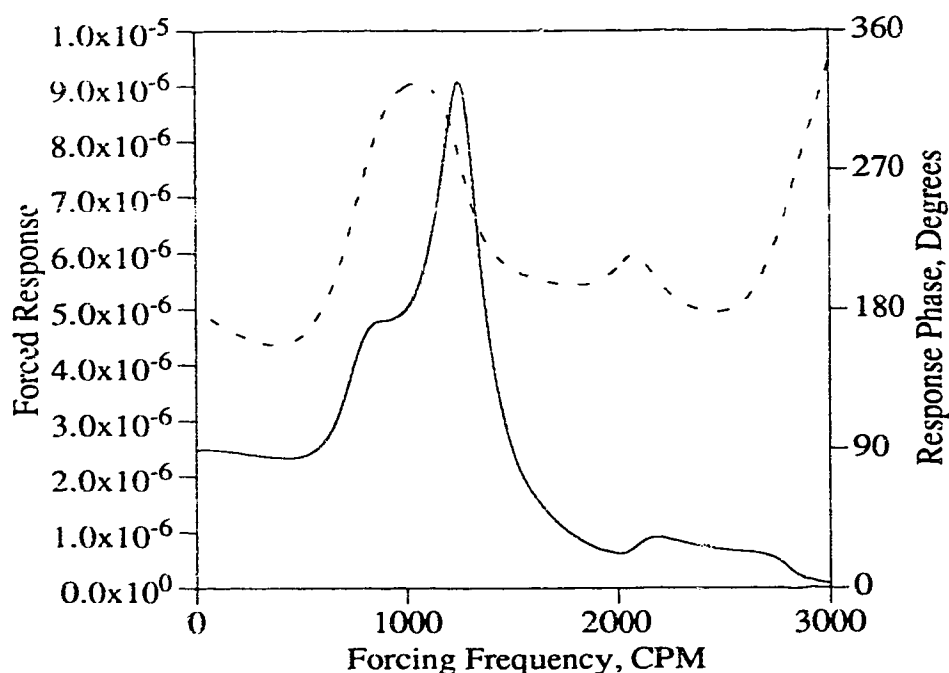
**FIGURE 5.29**: Bode Plot For Damped Machine (10 Times Damping)

## 5.4 Conclusions

The continuous coordinate condensation method provides an excellent means to calculate the forced response of a dynamic system while retaining a reduced need for storage memory and computational time. As well, the procedure can also be used to determine the natural frequencies of a dynamic system where the fully assembled global model would have a large number of degrees of freedom. The method is especially useful for chain assembled finite element systems where the algorithm to condense intermediate degrees of freedom is simple, and where only a few select coordinates are needed to represent the system motion.

The systems presented here included damping and gyroscopic effects. With only gyroscopic matrices, the system can still be reduced to a set of real equations, and the responses may be calculated by solving the set of linear equations using real

**Real Response**

-6x10⁻⁶-4x10⁻⁶-2x10⁻⁶ 0x10⁰ 2x10⁻⁶ 4x10⁻⁶ 6x10⁻⁶
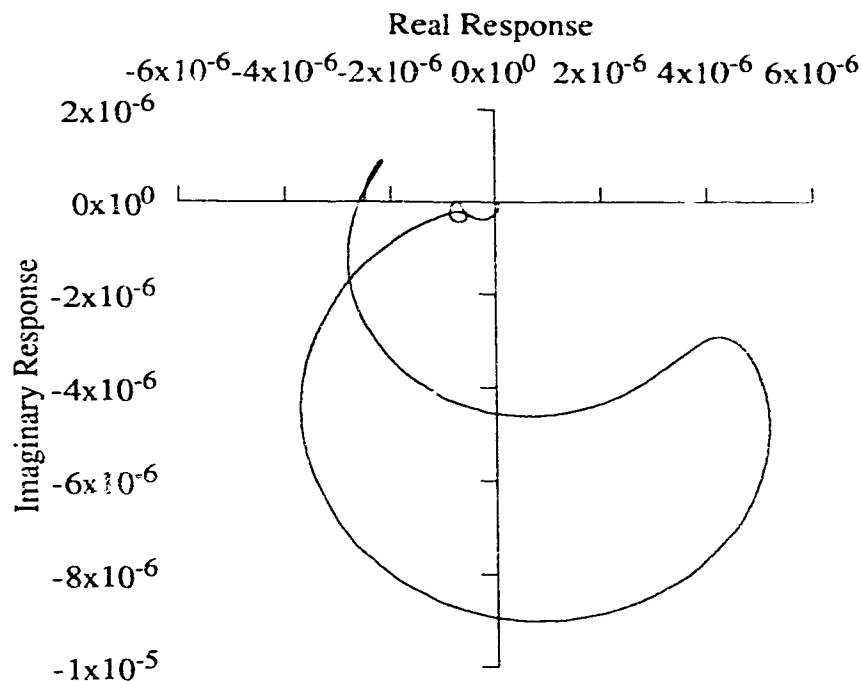


**FIGURE 5.30**: Polar Plot (10 Times Damping)

algebra. However, with the addition of damping, the set of equations is complex, and the solution must use a complex equation solver, or the degrees of freedom may be doubled and treated as a real system of equations. The solution of full matrix finite element models with either gyroscopic or damping matrices requires the use of non-symmetric eigenvalue solvers with increased memory and time required. For the case of damping, the condensation procedure must also look at the phase change to find the natural frequencies. As a result, rather than just plotting the frequency response function, the analyst must also plot the phase or plot the real and imaginary components of the response on a polar plot.

Again, the analyst has wide latitude in where the forcing function is input, and on how the response is measured. Some engineering judgment and foresight is required to prevent having the input force or response degree of freedom at a vibration node for a particular mode. These points may have to be moved for the

various modes to find the natural frequencies.

The analyst also can influence the speed of solution greatly, by specifying a coarse frequency step size when calculating the frequency response curves over the desired total range. The peak frequencies can then be refined by using finer frequency step sizes over a tighter frequency range about each of the peak frequencies.

# CHAPTER 6

# System Identification

*Measure For Measure — Shakespeare*

## 6.1  Introduction

Once a mathematical model of a dynamic system has been created, the accuracy of the model may still be somewhat in doubt. For instance, the presence of step changes in diameter, shrink fit wheels and hubs, and laminated shafts may introduce some stiffness effects that are not modelled well. That is, the local "effective" stiffness of the shaft may be different from the stiffness predicted by the actual shaft diameter. It may then be desirable to refine the model so that the predicted dynamic characteristics calculated with the mathematical model are closer to those that are actually measured. For example, if the calculated and measured natural frequencies of a modelled structure are significantly different, then any subsequent numerical analysis with an uncorrected model, such as the forced response of the structure, will be in error. Refinement usually requires the calculation of some adjustment factor of individual numerical parameters of the model by using the differences between experimentally measured and mathematically modelled dynamic characteristics. This process is known as system identification, or model refinement.

An accurate finite element model is useful in the area of turbomachinery

dynamics for vibration analysis, balancing, and dynamic design of proposed rotor system changes. In addition, a system identification technique can also be used for examining the change in vibration of a machine over a period of time, and identifying what physical parameters of the system have changed. For example, a change in vibration signature of a particular machine may be due to a change in balance or bearing condition. A refinement procedure may predict the location or nature of the problem, allowing a safe, planned maintenance shutdown.

System identification is essentially a subset of the inverse problem, where the physical properties of a system are calculated from the behaviour of the system. In terms of vibrations and dynamics, the inverse problem is one of calculating the mass, stiffness and damping distribution of a system from its measured dynamic responses. Normally the measured data is in the frequency domain; that is, the natural frequencies and mode shapes or the frequency response curves are known rather than the vibration time signal.

Many methods for the solution of the inverse problem have been presented which create complete mass, stiffness and damping matrices. Gladwell [31] showed that to create complete pentadiagonal matrices, such as those produced by beam finite element discretization, requires the measurement of three spectral data sets under different beam boundary conditions. Although the objectives are the same, the work of this chapter is concerned with the optimization or refinement of an already existing finite element model rather than the formulation of a complete model from experimental data.

In 1976, Stetson and Palma [32] presented a method which used the inversion of first-order perturbation theory to improve an already existing model. The method calculated the necessary changes to a mathematical model to perturb mode shapes a known amount. The method could be used to refine an existing finite element model by iteratively perturbing the calculated mode shapes and correcting the model until the mode shapes were the same as those measured experimentally.

And in 1980, Thomas and Littlewood [33] gave a method for calculating the axial stiffness distribution or profile of a rotor. The method used assumed a lumped mass model and calculated the moments of a Euler-Bernoulli beam at various axial positions in the rotor as the rotor was excited. From the bending moment at a particular location and the local curvature as measured from the mode shapes, the local effective stiffness and diameter were determined. Using this method Thomas predicted the axial position of a crack in a generator rotor, which was subsequently confirmed using non-destructive testing. In 1989, Vest and Darlow [34] expanded the Thomas method to include the rotatory inertia and shear deformation of Timoshenko beam theory, and also allowed a continuous mass distribution.

All the published methods require the input of measured mode shapes. This can present considerable difficulties in that the displacements of a shaft must be measured at the same locations as the nodes of the mathematical model, or curve fitting routines must be used to get the displacements at the required locations. Since the nodes frequently occur at changes in diameter, etc., it may be nearly impossible to accurately measure the displacement at these locations. As well, the angular displacement or slope of the neutral axis of the shaft is needed, and this can be difficult to measure even for an uniform shaft, and even more so for a shaft-disk system of complex geometry. Also inherent in the measured mode shapes is some amount of measurement noise which puts some numerical limitations on their use.

This chapter will present a simpler procedure for refining a mathematical model using Rayleigh's Quotient which does not require the use of complete or incomplete measured mode shapes (see Eckert and Craggs [35] [36]). The procedure was designed to be used to improve an existing finite element model that is not greatly in error by only comparing the analytically calculated and experimentally measured eigenvalues of the system. As well, the method is presented from the engineering point of view, in that it gives a usable mathematical model, but does not specifically address the problems of solution existence and uniqueness. The assumptions behind

the method are as follows:

1) The error in the model is mostly present in the stiffness matrix of the finite element model. That is, the stiffness effects of step changes etc., create the most uncertainty, or are the most difficult to model accurately. The material properties of the shaft and the dimensions of the shaft are usually well known, or are easily measured, and as a result, the mass matrix is a good representation of the physical distribution of mass in the actual shaft. Therefore, only the stiffness matrix of the model will be corrected by the algorithm.

2) The error that is present in the finite element stiffness matrix is not extremely large. The local "effective" stiffness diameter of the shaft is not more than 20% to 50% different than the modelled stiffness diameter. That is, the effective stiffness of the element varies by a factor of 0.5–5.0 times the original element stiffness.

3) The first six natural frequencies or fewer of the shaft or shaft section are to be corrected, and that the equivalent number of actual natural frequencies of the component have been measured in the free-free or simply-supported state. Normally modes higher than the sixth contribute negligible amounts to the response of a shaft, and therefore, higher modes are not corrected.

4) The analyst has some idea or is able to calculate which of the finite elements in the model contribute most to the error, and therefore decides a priori which elements are to be refined or corrected to improve the overall model.

5) The method must not change the bandedness of the original model. That is, the procedure must not introduce values into the global

stiffness matrix that were originally zero. As well, the method must only correct the model by adjusting the stiffnesses of individual finite elements of the model, thereby keeping the same quality or structure in the global matrix as that of the original finite element model.

6) Only the natural frequencies need to be measured. Since the assumed corrections of the finite element model are small adjustments to the stiffness matrix, the calculated mode shapes of the structure are close to actual. The natural frequencies of the structure are more sensitive to small errors in the stiffness matrix than the mode shapes, and hence measured mode shapes are not needed reducing the practical difficulties of measurement greatly.

Assumption 5) states that adjustment of the model shall only be done on the individual element matrices. However, the refinement method given in this chapter does not require specifically that only the element matrices be adjusted. For instance, several element stiffness matrices may be assembled together as a system component with that stiffness submatrix being corrected. The choice of which element matrices to adjust, and which element matrix corrections should be corrected as a submatrix is not part of the refinement algorithm presented. It is, however, up to the modeller to use engineering judgment in making those decisions.

To justify the use of calculated mode shapes instead of measured mode shapes, as stated in assumption 6), a numerical experiment was conducted. The first six eigenvalues and mode shapes of an uniform cantilever beam modelled with simple Euler-Bernoulli beam elements were calculated, and then compared to those calculated when the "stiffness" diameter of the center elements, as shown in Fig. 6.1, was doubled. Doubling the diameter increased the stiffness of the center elements by sixteen times the uniform diameter stiffness, which is a greater correction than the refinement algorithm would be expected to calculate.

$$E = 30 \times 10^6 \text{ psi.,} \quad \rho = 0.283 \text{ lbs./in.}^3$$
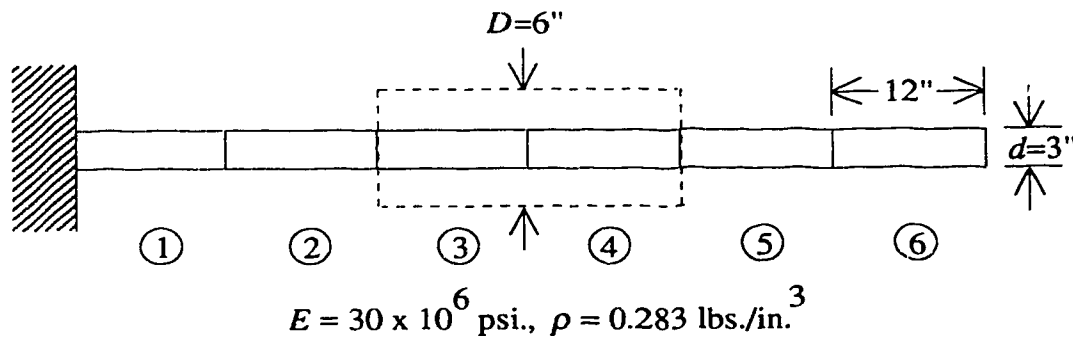
**FIGURE 6.1**: Model To Test Effects Of Varying Stiffnesses

The first six eigenvalues versus the diameter ratio of the center elements are plotted on a log-linear plot in Fig. 6.2. Increasing the stiffness of the center elements to sixteen times the uniform stiffness resulted in the first natural frequency increasing by 20% (eigenvalue by 44%). The second natural frequency increased by 58% (eigenvalue by 150%). The other four natural frequencies increased by similar or greater amounts. Therefore, doubling the stiffness diameter of the center section of the beam resulted in significant increases in the eigenvalues, ensuring that an algorithm which corrects the stiffnesses on the basis of the eigenvalues is stable for this particular case.

The first two mode shapes for the uniform stiffness diameter and for double the stiffness diameter are shown in Fig. 6.3. The mode shapes can be seen to be essentially the same. The second mode shows the most variation in the center of the beam, where the change in bending angle and hence the greatest storage of strain energy occurs in the stiffened elements. Since the mode shapes are relatively close for a large increase in stiffness of the center elements, it was decided that the calculated modes shapes were an acceptable alternative to measured mode shapes in the refinement procedure. This numerical experiment demonstrated that the mode shapes are much less sensitive to changes in element stiffnesses than are the eigenvalues.
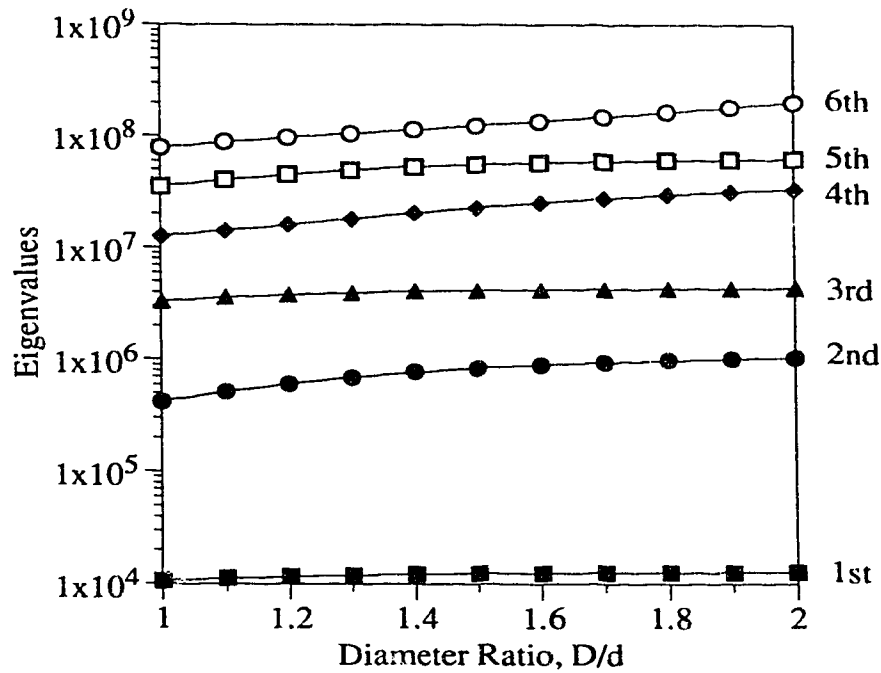
**FIGURE 6.2:** Stiffness Effect On Eigenvalues

The refinement algorithm is used by measuring the required eigenvalues with the shaft suspended in the free-free or simply-supported state. The free-free boundary condition can be accomplished by hanging the shaft from cables and exciting it in the horizontal plane. The rigid body modes introduced have very low natural frequencies, and can be easily separated from the flexible modes of the shaft. The excitation frequency should be swept through the frequency band of interest, and the resulting response curve measured with an accelerometer. The frequencies at which the response is a peak, and the corresponding response-to-excitation phase shifts by 180° are natural frequencies. Acceptable measurement accuracy of the natural frequencies should be readily attainable. The algorithm then compares the measured eigenvalues to those calculated by the uncorrected finite element model and gives the needed stiffness correction factors for the specified elements. The factors are applied and the correlation between the measured and analytical eigenvalues is
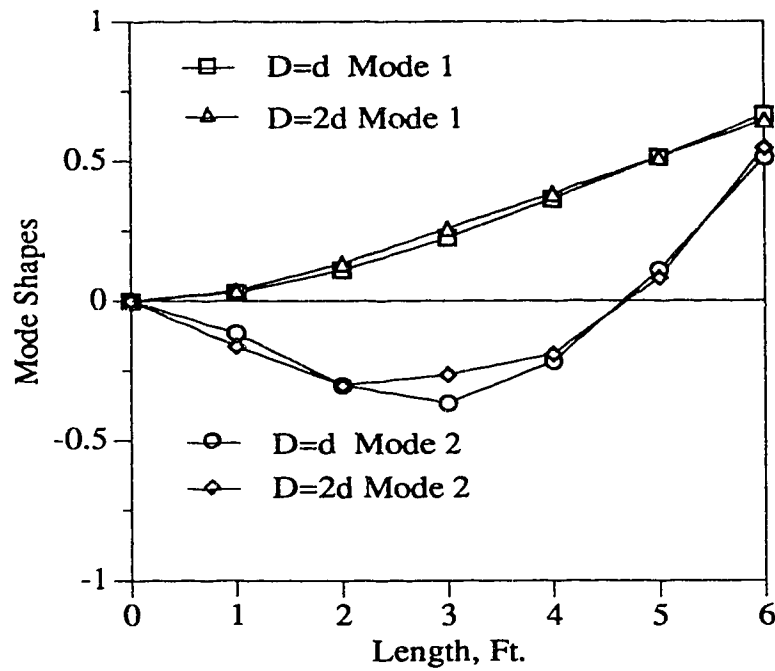
**FIGURE 6.3**: Stiffness Effect On Mode Shapes

checked. The corrections proceed iteratively until the eigenvalues match within a specified tolerance.

The number of eigenvalues correlated by the refinement algorithm does not need to be the same as the number of elemental stiffnesses to be corrected. The methods needed to correct the model when the number of eigenvalues are greater or less than the element corrections are discussed later.

## 6.2 Theory Of System Identification

Assuming that an undamped structure is being modelled, the matrix equation of motion for that structure in free vibration is:

$$[M]\{\ddot{x}\} + [K]\{x\} = \{0\}.$$  (6.1)

Now, let the solution to Eq. (6.1) be a harmonic solution and recast the equation of motion as an eigenvalue problem.

$$\left([K] - \omega^2[M]\right) \{X\} = \{0\} \tag{6.2}$$

In Eq. (6.2) the eigenvalue, $\omega^2$, is the square of the natural frequency of the modelled structure, while the eigenvector, $\{X\}$, is the mode shape of the structure when vibrating at the natural frequency.

For a conservative system vibrating with the single mode shape, $\{X\}$, the maximum kinetic energy due to the motion of the system must be equal to the maximum potential energy due to the elastic displacement of the system. This can be written in the following matrix form assuming the system is vibrating with the natural frequency $\omega$.

$$\frac{1}{2}\omega^2 \{X\}^T [M] \{X\} = \frac{1}{2} \{X\}^T [K] \{X\} \tag{6.3}$$

Rearranging Eq. (6.3) to get the eigenvalue alone on one side of the equality results in the well known Rayleigh's Quotient [4]:

$$\omega^2 = \frac{\{X\}^T [K] \{X\}}{\{X\}^T [M] \{X\}}. \tag{6.4}$$

Rayleigh's Quotient has been used historically to predict the natural frequency of a dynamic system. If the mass and stiffness distribution of the system are known, and the mode shape of vibration is estimated, then the natural frequency given by Eq. (6.4) is an upper bound approximation of the first natural frequency of the system. As the error between the approximate mode shape and the real mode shape is reduced the calculated natural frequency approaches the real natural frequency.

| 1 | 2 | 3 | 4 | 5 |
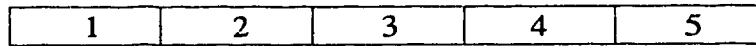
**FIGURE 6.4**: Chain Assembled Model

If the exact mode shape is known, then Rayleigh's Quotient will result in the exact natural frequency of the dynamic system for that mode.

Suppose that the eigenvalue equation as given by Eq. (6.2) represents the system of equations for a model of chain assembled finite elements as shown in Fig. 6.4. Then assume that the global stiffness matrix in Rayleigh's Quotient is given by the following equation, where the individual element stiffness matrices are properly placed in the global stiffness matrix.

$$[K] = \begin{bmatrix} [K_{e1}] & & \\ & \ddots & \\ & & \ddots \end{bmatrix} + \begin{bmatrix} \ddots & & \\ & [K_{e2}] & \\ & & \ddots \end{bmatrix} + \cdots + \begin{bmatrix} \ddots & & \\ & \ddots & \\ & & [K_{e5}] \end{bmatrix} \tag{6.5}$$

Now if the theoretical stiffness of the $j$th element of the model is incorrect by the fraction $a_j$, then the $j$th element actual stiffness matrix may be written as:

$$[K_{ej}]_{\text{actual}} = (1 + a_j)[K_{ej}]_{\text{theoretical}}. \tag{6.6}$$

Substituting Eq. (6.5) and Eq. (6.6) into Rayleigh's Quotient Eq. (6.4), results in:

$$\lambda_i^2 \approx \omega_i^2 + a_j \frac{\{X_i\}^T [[K_{ej}]] \{X_i\}}{\{X_i\}^T [M] \{X_i\}}, \tag{6.7}$$

where $\lambda_i^2$ is the $i$th measured or actual eigenvalue of the system, $\omega_i^2$ is the $i$th calculated eigenvalue from the uncorrected model, $a_j$ is the stiffness correction factor for the $j$th element of the model, and $\{X_i\}$ is the $i$th calculated eigenvector of the

uncorrected model. Note that $[[K_{ej}]]$ is the $j$th element stiffness matrix properly placed inside a null matrix of global order. Rearranging Eq. (6.7) gives:

$$\frac{\{X_i\}^T [[K_{ej}]] \{X_i\}}{\omega_i^2 \{X_i\}^T [M] \{X_i\}} a_j = \frac{\lambda_i^2}{\omega_i^2} - 1. \tag{6.8}$$

The right hand term in Eq. (6.8) represents the error between the $i$th calculated and measured eigenvalues. The left hand term is the correction factor, $a_j$, for the $j$th element times its corresponding coefficient. Suppose that the number of element stiffness matrices to be corrected is $p$, then to account for the effects of all the possible elemental corrections on the $i$th eigenvalue, Eq. (6.8) must be modified to sum over all $p$ elements.

$$\sum_{j=1}^{p} \frac{\{X_i\}^T [[K_{ej}]] \{X_i\}}{\omega_i^2 \{X_i\}^T [M] \{X_i\}} a_j = \frac{\lambda_i^2}{\omega_i^2} - 1 \tag{6.9}$$

Eq. (6.9) is one equation representing the effects of all the $p$ corrected element stiffnesses on the $i$th eigenvalue. Writing similar equations for the other eigenvalues to be corrected, $n$ in total, results in the following matrix equation with $n$ equations in $p$ unknowns.

$$\underset{n \times p}{[C]} \quad \underset{p}{\{a\}} = \underset{n}{\{\delta\}} \tag{6.10}$$

The matrix $[C]$, represents the coefficients of all the elemental corrections for each individual eigenvalue error. The vector, $\{a\}$, is a column of the correction factors for each element to be modified, and the vector, $\{\delta\}$, is a column of the errors for each eigenvalue to be correlated. The calculated mode shapes together with the element stiffness matrices and global mass matrix give each coefficient in the matrix, $[C]$. The error vector is easily calculated from the difference between the calculated and measured eigenvalues. Assuming that the number of elemental stiffnesses to

be corrected, and the number of measured eigenvalues of the system are the same, the resulting $n$ linear equations in $n$ unknowns can solved for the correction factor vector.

The refinement process for the system is an iterative one. First, the uncorrected finite element model of the system is assembled. Then the required number of eigenvalues and eigenvectors are calculated from this original model. The calculated eigenvalues are compared to the experimentally measured eigenvalues, and the corresponding correction factors are calculated for the finite element stiffnesses. The elements to be corrected are specified by the analyst before the refinement procedure begins. The element stiffnesses are then adjusted by the calculated correction factors (applying an underrelaxation factor to the corrections seems to improve the convergence) and a new adjusted finite element model is assembled. This model is now used to calculate a new set of eigenvalues and vectors, and the correction procedure is continued in this manner until the calculated eigenvalues are within an acceptable tolerance of the measured eigenvalues.

If the number of element stiffnesses, $p$, to be adjusted is not equal to the number of measured eigenvalues to be matched, $n$, then a system of $n$ equations in $p$ unknowns is formed. This may be solved in a number of ways. First, a linear regression may be performed by pre-multiplying Eq. (6.10) by the transpose of matrix $[C]$. This gives a new system of $p$ equations in $p$ unknowns as shown below.

$$\underset{p \times n}{[C]^T} \underset{n \times p}{[C]} \underset{p}{\{a\}} = \underset{p \times n}{[C]^T} \underset{n}{\{\delta\}} \tag{6.11}$$

Eq. (6.11) may be rewritten as:

$$\underset{p \times p}{[C']} \underset{p}{\{a\}} = \underset{p}{\{\delta'\}} \tag{6.12}$$

If the number of elements to be adjusted are less than the number of eigenvalues to be matched, that is $p < n$, then adjustment correction factors may also be calculated by solving the system of equations with groups of $p$ eigenvalues to be matched. That is, the first $p$ measured eigenvalues are used as input to the refinement algorithm. After the process has converged to a set of correction factors, the model is then adjusted and used as the starting model for the next set of adjustment factors. The input for the next set of correction factors is the set of $p$ eigenvalues starting with the second measured value. The second newly corrected model is then used as the starting point for matching the set of $p$ eigenvalues starting with the third measured value and so on, until all $n$ measured and calculated eigenvalues are equal. This method will be demonstrated with a beam element model, with the results given later in this chapter.

When the number of elements are greater than the number of eigenvalues to be corrected, that is $p > n$, then instead of linear regression the analyst may reduce the number of elements to be adjusted. Or, the analyst may reexamine the model and constrain a number of the elements to be adjusted the same amount, thereby reducing the number of correction factors $p$ to the number of measured eigenvalues available.

Using simple linear regression and solving Eq. (6.12) for a set of adjustment factors works satisfactorily for uncomplicated finite element models with few degrees of freedom. If however, the model is quite large, then the matrix, $[C'']$, may become singular or nearly singular, and therefore the solution of the equation using matrix inversion or Gaussian elimination becomes impossible. For these cases, it is more useful to recast the equations slightly and use singular value decomposition routines to solve for the least squares solution. Suppose, that instead of calculating a small adjustment factor $a_j$ for the $j$th element, as in Eq. (6.6), an overall multiplier for the $j$th element stiffness is calculated. That is:

If the number of elements to be adjusted are less than the number of eigenvalues to be matched, that is $p < n$, then adjustment correction factors may also be calculated by solving the system of equations with groups of $p$ eigenvalues to be matched. That is, the first $p$ measured eigenvalues are used as input to the refinement algorithm. After the process has converged to a set of correction factors, the model is then adjusted and used as the starting model for the next set of adjustment factors. The input for the next set of correction factors is the set of $p$ eigenvalues starting with the second measured value. The second newly corrected model is then used as the starting point for matching the set of $p$ eigenvalues starting with the third measured value and so on, until all $n$ measured and calculated eigenvalues are equal. This method will be demonstrated with a beam element model, with the results given later in this chapter.

When the number of elements are greater than the number of eigenvalues to be corrected, that is $p > n$, then instead of linear regression the analyst may reduce the number of elements to be adjusted. Or, the analyst may reexamine the model and constrain a number of the elements to be adjusted the same amount, thereby reducing the number of correction factors $p$ to the number of measured eigenvalues available.

Using simple linear regression and solving Eq. (6.12) for a set of adjustment factors works satisfactorily for uncomplicated finite element models with few degrees of freedom. If however, the model is quite large, then the matrix, $[C']$, may become singular or nearly singular, and therefore the solution of the equation using matrix inversion or Gaussian elimination becomes impossible. For these cases, it is more useful to recast the equations slightly and use singular value decomposition routines to solve for the least squares solution. Suppose, that instead of calculating a small adjustment factor $a_j$ for the $j$th element, as in Eq. (6.6), an overall multiplier for the $j$th element stiffness is calculated. That is:

$$[K_{ej}]_{\text{actual}} = b_j [K_{ej}]_{\text{theoretical}}. \qquad (6.13)$$

where $b_j = 1 + a_j$. Then Eq. (6.7) becomes:

$$\lambda_i^2 \approx \frac{\{X_i\}^T [K]_{\text{unc.}} \{X_i\}}{\{X_i\}^T [M] \{X_i\}} + b_j \frac{\{X_i\}^T [[K_{ej}]] \{X_i\}}{\{X_i\}^T [M] \{X_i\}}, \qquad (6.14)$$

where $[K]_{\text{unc.}}$ represents the remaining uncorrected portion of the global matrix that will not be adjusted. Let:

$$\frac{\{X_i\}^T [K]_{\text{unc.}} \{X_i\}}{\{X_i\}^T [M] \{X_i\}} = \gamma_i^2. \qquad (6.15)$$

where $\gamma_i^2$ represents the contribution to the $i$th eigenvalue of the elements that will not be corrected. Since this portion of the equation is known, it can be taken to the other side of the equation. Then, accounting for the effects of all the elements to be corrected on the $i$th eigenvalue, gives the following equation:

$$\sum_{j=1}^{p} \frac{\{X_i\}^T [[K_{ej}]] \{X_i\}}{\{X_i\}^T [M] \{X_i\}} b_j = \lambda_i^2 - \gamma_i^2. \qquad (6.16)$$

Writing the equations for the other measured eigenvalues to be matched results in the following:

$$\underset{n \times p}{[C'']} \quad \underset{p}{\{b\}} = \underset{n}{\{\delta''\}}. \qquad (6.17)$$

Eq. (6.17) is now a set of $n$ equations in $p$ unknowns where the vector $\{\delta''\}$ is now almost constant from one iteration to the next. The only components of the vector that change are the calculated mode shapes, and these do not change

greatly. With the previous formulation of Eq. (6.12) the vector $\{\delta'\}$ tends to become a null vector as the difference between the calculated and measured eigenvalues gets smaller on subsequent iterations. As well, with the previous formulation the matrix $[C'']$ becomes singular or nearly singular, resulting in a singular homogeneous system of equations. A non-zero vector is a possible solution for a singular set of homogeneous equations. However, after a number of iterations, the desired solution vector is the null vector, or trivial solution. Therefore, any other solution will lead to an incorrect adjustment of the element stiffness matrices. The new solution vector, $\{b\}$ of Eq. (6.17) tends to become a column of numbers close to 1.0 . Since the number of unknowns is not generally the same as the number of equations, singular value decomposition [37] should be used for the determining the best fit solution. Singular value decomposition can be used to solve the following, where $m \geq n$:

$$\underset{m \times n}{[A]} \quad \underset{n}{\{x\}} \quad = \quad \underset{m}{\{y\}} \ . \tag{6.18}$$

The matrix $[A]$ is decomposed as follows:

$$\underset{m \times n}{[A]} \quad = \quad \underset{m \times n}{[U]} \quad \underset{n \times n}{[W]} \quad \underset{n \times n}{[V]^T} \ , \tag{6.19}$$

where $[W]$ is a diagonal matrix, $[U]$ is column-orthogonal, and $[V]$ is column and row-orthogonal. Then the solution can be found by:

$$\underset{n}{\{x\}} \quad = \quad \underset{n \times n}{[V]} \quad \underset{n \times n}{[W]^{-1}} \quad \underset{n \times m}{[U]^T} \quad \underset{m}{\{y\}} \ , \tag{6.20}$$

where the inverse of $[W]$ is simply given by taking the reciprocal of the diagonal elements. The reciprocal of any zero diagonal element of $[W]$ is simply set to zero. When $[A]$ is originally square and nearly singular, and therefore ill-conditioned, before back substitution takes place the diagonal values of $[W]$ which are relatively
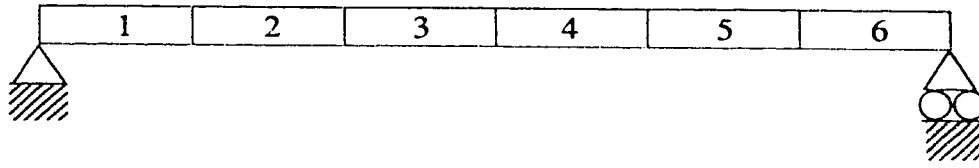
**FIGURE 6.5**: Example of a Simply-Supported Model

small are zeroed. This is the same as discarding a linear combination of the set of equations used. When the number of equations is less than the number of unknowns, then both the [A] matrix and the {y} vector are augmented with rows of zeros at the bottom, so that $m = n$. Before back substitution, at least the same number of diagonals of [W] as rows added will be zero or negligible. In both these cases, the matrix [A] is singular, and therefore an unique solution is not expected. Singular value decomposition gives the solution vector with the smallest value in the least squares sense. When there are more equations than unknowns, then no diagonals of [W] need be set to zero before solution.

The adjustment vector, {b}, calculated by the singular value decomposition of Eq. (6.17) will be the one with the smallest numerical values. Since, the solution may not be unique, the solution with the least amount of correction to the element stiffnesses is assumed to be the correct engineering solution.

An additional problem that can be encountered is symmetry of the model. Suppose the model is of a simply-supported system as shown in Fig. 6.5, with elements of equal size, and that the two center elements are to be corrected on the basis of the first two measured eigenvalues. Then, the symmetry and antisymmetry of the first and second mode shapes about the center of the model would result in the correction algorithm having to solve the following equation:

$$\begin{bmatrix} C_1 & C_1 \\ C_2 & C_2 \end{bmatrix} \begin{Bmatrix} a_1 \\ a_2 \end{Bmatrix} = \begin{Bmatrix} \delta_1 \\ \delta_2 \end{Bmatrix}. \tag{6.21}$$

Since Eq. (6.21) is not an independent set of equations, it is not possible to solve for the correction factors. Therefore, the analyst must be careful to model the shaft with elements of different lengths. However, since real shafts generally have more complex geometries, it is not likely that this problem would be encountered when modelling the shaft of an actual machine.

## 6.3 Results

### 6.3.1 Torsional Model Test

The element chosen for the torsional refinement test was a simple one-dimensional shaft element with distributed mass which was chain assembled to form an overall system model. A single torsional shaft element is shown in Fig. 6.6, and has an applied torque, $T$, and an angular displacement, $\theta$, at each end of the element. The element mass (polar mass moment of inertia) and stiffness matrices are:

$$[M] = \frac{\rho I L}{6} \begin{bmatrix} 2 & 1 \\ 1 & 2 \end{bmatrix} \quad [K] = \frac{IG}{L} \begin{bmatrix} 1 & -1 \\ -1 & 1 \end{bmatrix}, \tag{6.22}$$

where $\rho$=mass density, $I$=polar moment of inertia, $L$=length of element, and $G$=shear modulus.

The particular steel shaft modelled is shown in Fig. 6.7. All six elements, including the disks were modelled as torsional elements, and as a result, the disks acted as extremely stiff torsional components, effectively leaving the model with only three flexible elements and degrees of freedom. Since a real shaft was not available for measurement of the eigenvalues, the "measurements" were created by calculating the system eigenvalues after adjusting the stiffnesses of the shaft sections by known factors. The eigenvalues calculated from the adjusted model were input into the refinement algorithm as the measured eigenvalues to perform a totally
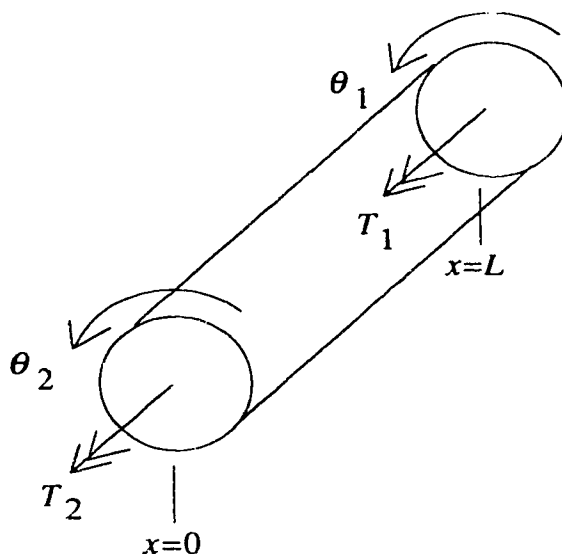
**FIGURE 6.6**: Torsional Shaft Element

numerical experiment. The adjusted stiffness diameters are represented in Fig. 6.7 as the dashed lines. The "actual" or target model had the stiffness of element 1 decreased to 70.61% of the original stiffness, while elements 3 and 5 were increased by 85.26% and 37.74%. The mass of the measured model was calculated using the uncorrected diameters, and the theoretical model was started as three uniform shaft elements of equal dimensions, with three disks of equal dimensions.

Since the model only had three torsional shaft elements to be corrected (elements 1, 3, and 5), but six corrected eigenvalues were desired, the refinement algorithm was tested by correlating the eigenvalues in groups of three only. That is, a set of three linear equations in three unknowns were formed and solved iteratively. The algorithm was tested by calculating three sets of corrections on the basis of matching the eigenvalues in the following groups: 1, 2, and 3; 2, 3, and 4; and 3, 4, and 5. The results of the tests are given in Table 6.1. The upper portion of the table compares the eigenvalues of the original uncorrected model, the measured or target shaft, and the eigenvalues of the three corrected models. The two upper left columns give the

①  ②  ③  ④  ⑤  ⑥

12"

3"

|← 12" →|← 12" →|← 12" →|

2" →|

$G = 11.5 \times 10^6$ psi., $\rho = 0.283$ lbs./in.$^3$
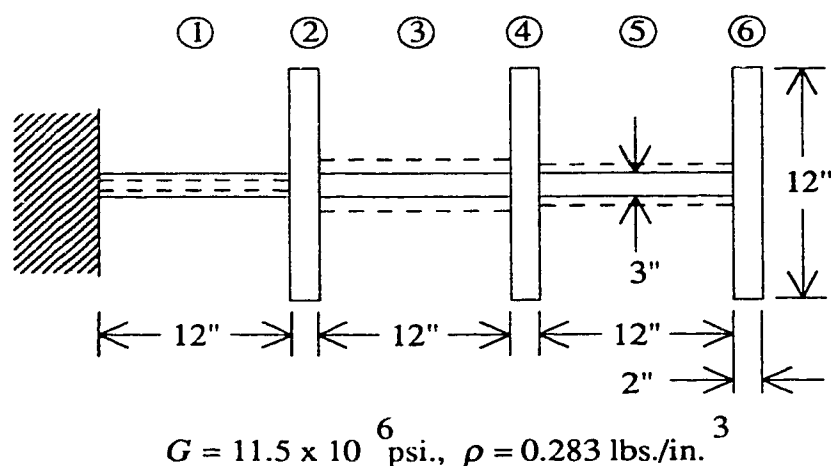
**FIGURE 6.7**: Torsional Model

**TABLE 6.1**: Torsional Model Correction

| Uncorrected Model | Measured Shaft | Corrected On Basis Of Eigenvalues | | |
|---|---|---|---|---|
| | | 1,2,3 (5 Iter.) | 2,3,4 (3 Iter.) | 3,4,5 (2 Iter.) |
| Eigenvalues | | | | |
| $4.9780 \times 10^6$ | $4.7115 \times 10^6$ | $4.7089 \times 10^6$ | $3.9875 \times 10^6$ | $4.2665 \times 10^6$ |
| $3.9208 \times 10^7$ | $4.7556 \times 10^7$ | $4.7455 \times 10^7$ | $4.7389 \times 10^7$ | $4.6478 \times 10^7$ |
| $8.2197 \times 10^7$ | $1.2889 \times 10^8$ | $1.2900 \times 10^8$ | $1.2906 \times 10^8$ | $1.2943 \times 10^8$ |
| $4.4423 \times 10^{11}$ | $4.4423 \times 10^{11}$ | $4.4423 \times 10^{11}$ | $4.4423 \times 10^{11}$ | $4.4423 \times 10^{11}$ |
| $4.5369 \times 10^{11}$ | $4.5378 \times 10^{11}$ | $4.5378 \times 10^{11}$ | $4.5377 \times 10^{11}$ | $4.5378 \times 10^{11}$ |
| $4.6301 \times 10^{11}$ | $4.6310 \times 10^{11}$ | $4.6310 \times 10^{11}$ | $4.6311 \times 10^{11}$ | $4.6310 \times 10^{11}$ |
| Stiffness Relative To Uncorrected Stiffness | | | | |
| El. 1:    1 | 0.7061 | 0.7049 | 0.5723 | 0.6211 |
| El. 2:    1 | 1.0000 | 1.0000 | 1.0000 | 1.0000 |
| El. 3:    1 | 1.8526 | 1.8585 | 1.8283 | 1.8866 |
| El. 4:    1 | 1.0000 | 1.0000 | 1.0000 | 1.0000 |
| El. 5:    1 | 1.3774 | 1.3721 | 1.4538 | 1.3663 |
| El. 6:    1 | 1.0000 | 1.0000 | 1.0000 | 1.0000 |

six eigenvalues of the original uncorrected model and of the measured shaft, and only the first three eigenvalues showed any significant numerical differences. ' remaining three upper columns give the calculated eigenvalues from the corrected finite element models. The first test case based on eigenvalues 1, 2, and 3 corrected the first three eigenvalues of the model to within an acceptable tolerance (1%). The fourth, fifth and sixth eigenvalues of the uncorrected model were already correct, and remained so after the correction. The second test case corrected the model so that the second and third eigenvalues were correct. As expected however, because this test case used the fourth measured eigenvalue, which was already correct, as input data the resulting corrected model did not predict the first eigenvalue within tolerance. The third test case used the fourth and fifth measured eigenvalues which the original model already gave exactly, and hence the adjusted model did not predict the first two eigenvalues correctly.

The lower columns of Table 6.1 give the stiffness ratios relative to the stiffnesses of the elements of the original uncorrected model. The values in the second column are the measured stiffness ratios or correction factors that the algorithm should have produced. For example, element number 1 of the measured model had a stiffness of 70.61% of the original model stiffness. The three columns on the lower right hand side of the table give the stiffness ratios of the model after correction by the refinement algorithm. As with the eigenvalues, the refinement algorithm gave the correct adjusted model when the first three measured eigenvalues were used as input. But, the other correction cases did not work well because of the use of uncorrected and measured eigenvalues of equal numerical value.

## 6.3.2 Beam Model Test

The Rayleigh's Quotient refinement algorithm was also tested on a beam model, as shown in Fig. 6.8, that was formed of Euler-Bernoulli beam elements (element

$$E = 30 \times 10^6 \text{ psi.}, \quad \rho = 0.283 \text{ lbs./in.}^3$$
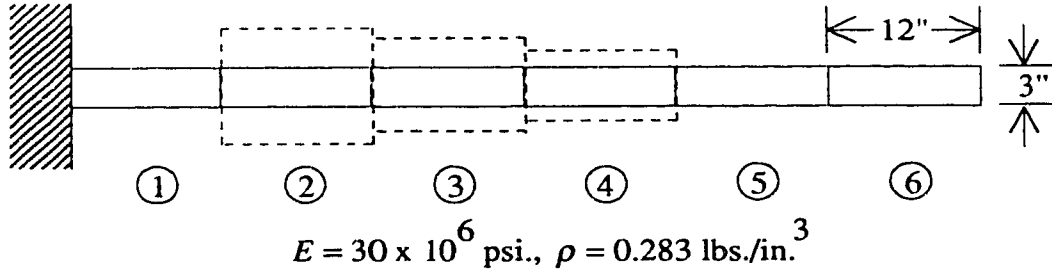
**FIGURE 6.8**: Euler-Bernoulli Beam Model

matrices are given by Eq. (6.23)) with the same degrees of freedom as shown in Fig. 2.2. Each of the six elements were twelve inches in length and three inches in diameter and where modelled as steel. As shown by the dashed lines in Fig. 6.8 the stiffness diameters of elements 2, 3, and 4 were increased when calculating the eigenvalues of the "measured" beam to again create a set of target eigenvalues for a numerical experiment. The stiffnesses of the target beam were adjusted as follows: element 2 was increased to 2.5 times the original stiffness; element 3 was increased to 2.0 times; and element 4 was increased to 1.5 times. The uncorrected model, which is the starting point for the refinement algorithm, is shown as the uniform beam (solid lines) in Fig. 6.8.

$$[M] = \rho A L \begin{bmatrix} \dfrac{13}{35} & \dfrac{11L}{210} & \dfrac{9}{70} & \dfrac{-13L}{420} \\[2mm] \dfrac{11L}{210} & \dfrac{L^2}{105} & \dfrac{13L}{420} & \dfrac{-L^2}{140} \\[2mm] \dfrac{9}{70} & \dfrac{13L}{420} & \dfrac{13}{35} & \dfrac{-11L}{210} \\[2mm] \dfrac{-13L}{420} & \dfrac{-L^2}{140} & \dfrac{-11L}{210} & \dfrac{L^2}{105} \end{bmatrix}$$

$$[K] = \frac{EI}{L^3} \begin{bmatrix} 12 & 6L & -12 & 6L \\ 6L & 4L^2 & -6L & 2L^2 \\ -12 & -6L & 12 & -6L \\ 6L & 2L^2 & -6L & 4L^2 \end{bmatrix}$$

(6.23)

**TABLE 6.2**: Beam Model Correction

| Uncorrected Model | Measured Shaft | Corrected On Basis Of Eigenvalues | | |
|---|---|---|---|---|
| | | 1,2,3 (3 Iter.) | 2,3,4 (5 Iter.). | 3,4,5 4,5,6 |
| Eigenvalues | | | | |
| $1.0602 \times 10^5$ | $1.4215 \times 10^5$ | $1.4109 \times 10^5$ | $1.4210 \times 10^5$ | $1.4210 \times 10^5$ |
| $4.1647 \times 10^6$ | $5.7692 \times 10^6$ | $5.7245 \times 10^6$ | $5.7686 \times 10^6$ | $5.7686 \times 10^6$ |
| $3.2755 \times 10^7$ | $4.5047 \times 10^7$ | $4.4711 \times 10^7$ | $4.5028 \times 10^7$ | $4.5028 \times 10^7$ |
| $1.2694 \times 10^8$ | $1.7479 \times 10^8$ | $2.0005 \times 10^8$ | $1.7474 \times 10^8$ | $1.7474 \times 10^8$ |
| $3.5283 \times 10^8$ | $4.7442 \times 10^8$ | $5.0528 \times 10^8$ | $4.7433 \times 10^8$ | $4.7433 \times 10^8$ |
| $7.8990 \times 10^8$ | $1.0666 \times 10^9$ | $1.0759 \times 10^9$ | $1.0663 \times 10^9$ | $1.0663 \times 10^9$ |
| Stiffness Relative To Uncorrected Stiffness | | | | |
| El. 1:    1 | 1.0 | 1.0000 | 1.0000 | 1.0000 |
| El. 2:    1 | 2.5 | 4.0970 | 2.4954 | 2.4954 |
| El. 3:    1 | 2.0 | 0.9708 | 1.9986 | 1.9986 |
| El. 4:    1 | 1.5 | 4.2447 | 1.5005 | 1.5005 |
| El. 5:    1 | 1.0 | 1.0000 | 1.0000 | 1.0000 |
| El. 6:    1 | 1.0 | 1.0000 | 1.0000 | 1.0000 |

This numerical test differed from the torsion model test, in that the algorithm was only allowed to correct the stiffnesses of elements 2, 3, and 4, but was required to match the first six measured and calculated eigenvalues. This is equivalent to setting up a system of six linear equations with three unknowns (the correction factors). The solution could have been arrived at using linear regression, but instead the correction factors were first calculated by comparing measured eigenvalues 1, 2, and 3 to those calculated. The results of this correction were then used as the starting point or uncorrected model for calculating the correction factors by matching eigenvalues 2, 3, and 4. The corrections were then continued on the basis of matching the next group of three eigenvalues, until all six were within the specified tolerance. The results of the test are shown in Table 6.2.

The first set of correction factors, on the basis of the lowest three eigenvalues, resulted in a correction considerably different from the "target" or measured shaft.

The system was underconstrained, meaning that the available data was not enough to ensure an unique solution. Note that, although the correction factors were in error, the first three corrected eigenvalues were calculated within the specified tolerance of 1% of the measured eigenvalues. Therefore, a corrected or adjusted finite element model was created by the refinement algorithm that had the same lowest three eigenvalues, but had different actual stiffnesses from the measured shaft. The second set of correction factors, based on eigenvalues 2, 3, and 4, and using the first correction as the starting point, matched the measured shaft almost exactly within five iterations. As a result, the last two sets of corrections based on eigenvalue groups 3, 4, and 5, and 4, 5, and 6, did not provide any additional correction to the beam model.

As an additional test, since there are six elements in the cantilever beam model, and six measured eigenvalues, the correction algorithm was run allowing some adjustment of all the elements. That is, there were six equations in six unknowns. The starting model was the uniform diameter cantilever beam as shown in Fig. 6.8, and the target beam with its measured eigenvalues are as given in Table 6.2. The algorithm gave the correct stiffness adjustments and eigenvalues (with 0.5% tolerance) within 9 iterations. The method worked well for this case, in that the elements to be corrected were not specified prior to the correction.

## 6.3.3  Step Test

The finite element model refinement procedure was also tested on a simply supported beam with step change in section modelled with Euler-Bernoulli beam elements as shown in Fig. 6.9. The test was done to evaluate the amount of stiffness correction that could be accurately found by the Rayleigh's Quotient method. Again the starting model was an uniform beam, and the target beam had the stiffnesses of elements three and four increased over the uniform beam stiffnesses by up to
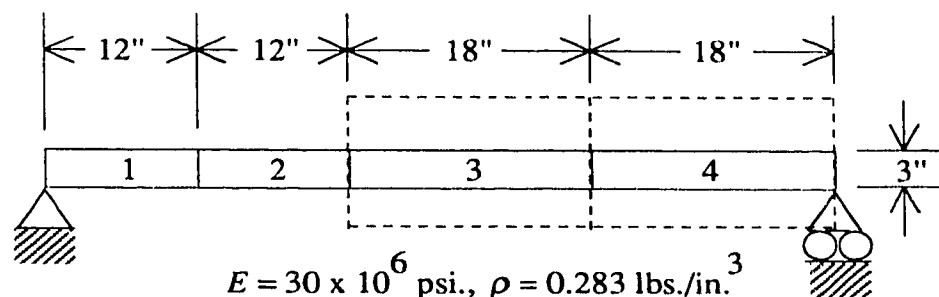
**FIGURE 6.9**: Step Change Beam Model

twenty times. In this test case, only elements three and four were specified to be corrected, and the first six measured eigenvalues were to be matched. The algorithm was limited to correcting the elements by matching two eigenvalues at a time as with the previous beam model, rather using the linear regression solution method. The corrected model at this point then became the starting model for subsequent matching subsequent eigenvalue pairs. At element stiffness ratios of 12 to 1, the algorithm gave the correct element adjustment on the basis of matching the first two measured eigenvalues. Further correction on the remaining four measured eigenvalues was not needed. For a stiffness ratio of 14 to 1, the method also correctly adjusted the stiffnesses, but a small additional correction was made by matching the second pair of measured eigenvalues. When the stiffness ratio was raised higher, the algorithm did not converge to a solution within the allowed twenty iterations. The calculated element adjustments were large, and the solution vector tended to oscillate. The eigenvalues of target beam, uncorrected model, and corrected model, and the element stiffness ratios are give in Table 6.3.

The correction of elements three and four was also attempted by using the simple linear regression method of Eq. (6.11). The first six measured eigenvalues were matched as a group. The correct stiffness adjustment was calculated within seven iterations for a target stiffness fifty times the starting stiffness, and the corrected

**TABLE 6.3**: Step Test Correction (14:1 Stiffness Ratio)

| Target Beam | Uncorrected Model | Corrected On Basis Of Eigen. | |
|---|---|---|---|
| | | 1,2 (11 Iter.) | 2,3 (2 Iter.) |
| Eigenvalues | | | |
| $4.5848 \times 10^5$ | $1.7332 \times 10^5$ | $4.6125 \times 10^5$ | $4.5849 \times 10^5$ |
| $1.3440 \times 10^7$ | $2.7955 \times 10^6$ | $1.3434 \times 10^7$ | $1.3442 \times 10^7$ |
| $5.0023 \times 10^7$ | $1.5119 \times 10^7$ | $4.8485 \times 10^7$ | $5.0023 \times 10^7$ |
| $2.3851 \times 10^8$ | $5.3144 \times 10^7$ | $2.3762 \times 10^8$ | $2.3852 \times 10^8$ |
| $5.2165 \times 10^8$ | $1.4887 \times 10^8$ | $5.2103 \times 10^8$ | $5.2172 \times 10^8$ |
| $1.6130 \times 10^9$ | $3.6043 \times 10^8$ | $1.6180 \times 10^9$ | $1.6132 \times 10^9$ |
| Stiffness Relative To Uncorrected Stiffness | | | |
| El. 1: 1 | 1.0000 | 1.0000 | 1.0000 |
| El. 2: 1 | 1.0000 | 1.0000 | 1.0000 |
| El. 3: 14 | 1.0000 | 15.551 | 14.009 |
| El. 4: 14 | 1.0000 | 12.201 | 13.996 |

eigenvalues matched the measured eigenvalues with a tolerance of 0.1%. Table 6.4 compares the eigenvalues of the target beam and uncorrected and corrected models, and the corresponding element stiffness ratios.

Additionally, the correction was done on all four elements by solving the equations with the simple linear regression method where the target beam had the stiffnesses of elements 3 and 4 multiplied by a factor of five. The first case started with the uniform beam as in the previous case. However, after running the maximum of 50 iterations the algorithm had adjusted the stiffnesses of all four elements to a set of unexpected values, and matched the first six eigenvalues within 9% as shown in Table 6.5. After the fifth iteration the stiffness multipliers were changing in the fourth or fifth decimal places only. The second least squares correction of all four elements started with a different uncorrected model. The new uncorrected model was formed by multiplying the stiffnesses of the original finite element model by the following factors: element 1 by 1.0, element 2 by 0.8, element 3 by 2.0, and

**TABLE 6.4**: Step Test Least Squares Correction of Elements 3 and 4

| Target Beam | Uncorrected Model | Corrected Model (7 Iter.) |
|---|---|---|
| Eigenvalues | | |
| $4.9927 \times 10^5$ | $1.7332 \times 10^5$ | $4.9929 \times 10^5$ |
| $2.0963 \times 10^7$ | $2.7955 \times 10^6$ | $2.0962 \times 10^7$ |
| $1.0700 \times 10^8$ | $1.5119 \times 10^7$ | $1.0690 \times 10^8$ |
| $3.1096 \times 10^8$ | $5.3144 \times 10^7$ | $3.1085 \times 10^8$ |
| $1.3464 \times 10^9$ | $1.4887 \times 10^8$ | $1.3456 \times 10^9$ |
| $2.0646 \times 10^9$ | $3.6043 \times 10^8$ | $2.0640 \times 10^9$ |
| Stiffness Relative To Uncorrected Stiffness | | |
| El. 1:   1 | 1.0000 | 1.0000 |
| El. 2:   1 | 1.0000 | 1.0000 |
| El. 3:   50 | 1.0000 | 50.048 |
| El. 4:   50 | 1.0000 | 49.840 |

**TABLE 6.5**: Step Test Least Squares Correction of Entire Model

| Target Beam | Corrected Model 1 (50 Iter.) | Corrected Model 2 (6 Iter.) |
|---|---|---|
| Eigenvalues | | |
| $3.7793 \times 10^5$ | $3.8828 \times 10^5$ | $3.7783 \times 10^5$ |
| $7.1021 \times 10^6$ | $6.7768 \times 10^6$ | $7.0970 \times 10^6$ |
| $3.4147 \times 10^7$ | $3.5065 \times 10^7$ | $3.4138 \times 10^7$ |
| $1.3621 \times 10^8$ | $1.2378 \times 10^8$ | $1.3610 \times 10^8$ |
| $3.2940 \times 10^8$ | $3.5034 \times 10^8$ | $3.2920 \times 10^8$ |
| $8.6054 \times 10^8$ | $8.9250 \times 10^8$ | $8.5992 \times 10^8$ |
| Stiffness Relative To Uncorrected Stiffness | | |
| El. 1:   1 | 2.2884 | 0.9964 |
| El. 2:   1 | 2.6478 | 1.0018 |
| El. 3:   5 | 2.0234 | 4.9751 |
| El. 4:   5 | 2.5447 | 5.0222 |

$E = 30 \times 10^6$ psi., $\rho = 0.283$ lbs./in.$^3$, $v = 0.30$
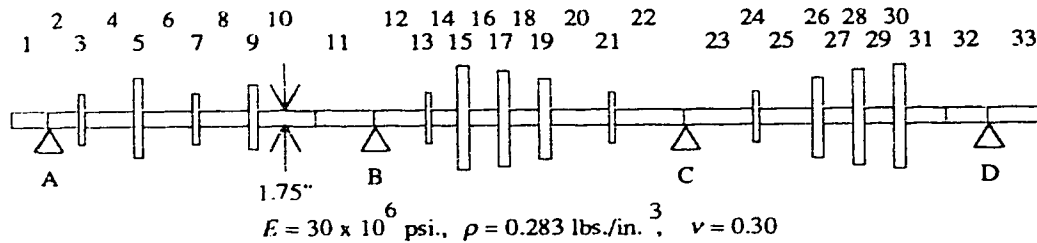
**FIGURE 6.10**: Scale Turbine Finite Element Model

element 4 by 4.0. This new starting model gave the correct model stiffness ratios and eigenvalues within 6 iterations. The results are given as the corrected model 2 in Table 6.5.

## 6.3.4 Turbine Model

All the previous examples have been numerical experiments where the measured eigenvalues were calculated by manually adjusting some of the stiffnesses of a finite element model. These measured eigenvalues were then used as input to the correction algorithm. However, a test of a correction of a finite element model of a real shaft was also done. In this case the shaft was the scale turbine model designed and built for Robertson's Master's thesis [38]. The finite element model of the shaft is shown in Fig. 6.10, with the dimensions given in Table 6.6. The scale model consists of a steel shaft with thirteen shrunk on disks suspended in four journal bearings and is driven by a variable speed motor through a flexible coupling at the f.. of element 1. The first five eigenvalues were measured for the non-rotating s.. while being simply supported at the bearing locations A and D, and being excited near the middle of element 6 (shaker location 2, Table 3.1 of [38]).

The shaft was modelled with thirty-three Timoshenko beam elements, and all the disks were included as short stiff beam elements contributing both mass and stiffness to the model. The diameter used to calculate the starting stiffness matrix

**TABLE 6.6**: Scale Turbine Model Element Dimensions

| Elem. No. | Dia. in. | Len. in. | Elem. No. | Dia. in. | Len. in. |
|---|---|---|---|---|---|
| 1 | 1.75 | 4.25 | 18 | 1.75 | 3.00 |
| 2 | 1.75 | 3.50 | 19 | 8.00 | 1.50 |
| 3 | 6.00 | 0.50 | 20 | 1.75 | 6.50 |
| 4 | 1.75 | 5.25 | 21 | 6.00 | 0.50 |
| 5 | 9.50 | 1.00 | 22 | 1.75 | 7.50 |
| 6 | 1.75 | 5.25 | 23 | 1.75 | 8.00 |
| 7 | 6.00 | 0.50 | 24 | 6.00 | 0.50 |
| 8 | 1.75 | 5.25 | 25 | 1.75 | 5.50 |
| 9 | 8.00 | 1.00 | 26 | 8.00 | 1.50 |
| 10 | 1.75 | 6.38 | 27 | 1.75 | 3.00 |
| 11 | 1.75 | 6.38 | 28 | 10.0 | 1.50 |
| 12 | 1.75 | 5.50 | 29 | 1.75 | 3.00 |
| 13 | 6.00 | 0.50 | 30 | 12.0 | 1.50 |
| 14 | 1.75 | 2.50 | 31 | 1.75 | 4.50 |
| 15 | 12.0 | 1.50 | 32 | 1.75 | 4.50 |
| 16 | 1.75 | 3.00 | 33 | 1.75 | 6.25 |
| 17 | 10.0 | 1.50 | | | |

for each individual element of the model was 1.75in., while the mass diameter was the actual diameter listed in Table 6.6. The correction procedure was performed for two different cases.

For the first correction case it was decided to allow the stiffnesses of all the elements to be corrected except for elements 1 and 33. Since these were short shaft elements outside the supports, their stiffness would have very little effect on the shaft natural frequencies. Correcting 31 elements with five measured eigenvalues resulted in a system of five equations in 31 unknowns. The correction was first applied using the simple linear regression technique of Eq. (6.12). However, it was found that the resulting square matrix was very nearly singular. Gaussian elimination with pivoting produced a solution vector with large numerical values. Substituting the solution back into the equation did give the correct right hand side vector, however, the resulting stiffness corrections were so large that the procedure was unable to converge to a final stiffness correction. Singt r value decomposition was then used on the $[C''']$ matrix of Eq. (6.17) with the matrix being augmented by additional rows of zeros at the bottom to achieve a square matrix of order 31. The resulting solution vector had numerical values in the order of 1.0, and the procedure was able to converge to a solution in six iterations with a tolerance of 2% of the measured eigenvalues. The final corrections or factors that the element stiffnesses were multiplied by are given in Table 6.7 as corrected model 1, and elements with a correction factor of 1 were restricted from adjustment by the algorithm. Shaft elements near the middle of the shaft, especially those between the disks, such as elements 18 and 20 had large corrections. As an example, the stiffness of shaft element 20 was multiplied by 4.2 over its starting stiffness. The disk elements received a variety of corrections. The smaller disk 3 had its stiffness multiplied by .03, while disk 17 had its stiffness multiplied by 1.3.

To check if the corrections were reasonable, the ratio of each elements strain energy to overall model kinetic energy for each of the first five modes of the original

uncorrected model was calculated as follows:

$$\frac{\{X_i\}^T [[K_{ej}]] \{X_i\}}{\omega_i^2 \{X_i\}^T [M] \{X_i\}} = \text{element contribution.} \qquad (6.24)$$

As expected the sum of the ratios for all the elements divided by the corresponding eigenvalue did result in unity, and the shaft elements in the mid-span of the shaft contributed most for the first five modes. Therefore, it was expected that the middle shaft sections would be the most effective element stiffnesses to adjust to achieve the corrected model as found by the correction procedure. Also, the elements modelling the disks contributed the least to the overall strain energy and would have little or no effect on the correction of the model. This was because the shaft elements representing the disks were short and relatively stiff, and had a small change in bending angle along the element length. This lead to attempting a second element adjustment where only the shaft sections, excluding elements 1 and 31, were corrected.

For this second correction case, the procedure was also able to converge to a corrected model with eigenvalues within 2% of those measured. The corresponding correction factors (Corr. Fact. 2) are also given in Table 6.7. Again, the shaft elements in the mid-span had their stiffnesses greatly increased, while the elements near the supports had their stiffnesses decreased. There is reasonable agreement between the correction factors of the two cases for those elements that were allowed to be adjusted, although the two different correction sets indicated that there was no unique solution to the problem.

Table 6.8 compares the natural frequencies measured, and calculated from the uncorrected model, and corrected models 1 and 2. Also, the percentage change in natural frequencies from the uncorrected values to final corrected values are given. The change required for the first three natural frequencies were substantial with

**TABLE 6.7**: Model Element Stiffness Corrections

| Elem. No. | Start. Fact. | Corr. Fact. 1 | Corr. Fact. 2 | Elem. No. | Start. Fact. | Corr. Fact. 1 | Corr. Fact. 2 |
|---|---|---|---|---|---|---|---|
| 1 | 1 | 1 | 1 | 18 | 1 | 2.666 | 2.068 |
| 2 | 1 | 0.076 | 0.066 | 19 | 1 | 1.285 | 1 |
| 3 | 1 | 0.032 | 1 | 20 | 1 | 4.178 | 3.665 |
| 4 | 1 | 0.845 | 0.619 | 21 | 1 | 0.233 | 1 |
| 5 | 1 | 0.284 | 1 | 22 | 1 | 2.585 | 1.888 |
| 6 | 1 | 1.757 | 0.848 | 23 | 1 | 2.712 | 1.622 |
| 7 | 1 | 0.199 | 1 | 24 | 1 | 0.220 | 1 |
| 8 | 1 | 2.497 | 1.311 | 25 | 1 | 2.822 | 2.301 |
| 9 | 1 | 0.570 | 1 | 26 | 1 | 0.855 | 1 |
| 10 | 1 | 3.460 | 2.901 | 27 | 1 | 1.518 | 1.460 |
| 11 | 1 | 3.040 | 3.393 | 28 | 1 | 0.623 | 1 |
| 12 | 1 | 2.529 | 2.899 | 29 | 1 | 0.974 | 0.731 |
| 13 | 1 | 0.243 | 1 | 30 | 1 | 0.433 | 1 |
| 14 | 1 | 1.293 | 1.214 | 31 | 1 | 0.826 | 0.502 |
| 15 | 1 | 0.898 | 1 | 32 | 1 | 0.161 | 0.114 |
| 16 | 1 | 2.210 | 1.406 | 33 | 1 | 1 | 1 |
| 17 | 1 | 1.290 | 1 | | | | |

**TABLE 6.8**: Scale Turbine Model Natural Frequencies

| Measured Hz. | Uncorrected Model Hz. | Corrected Model 1 Hz. | Change % | Corrected Model 2 Hz. | Change % |
|---|---|---|---|---|---|
| 8.00 | 6.17 | 7.97 | 29.2 | 8.02 | 29.9 |
| 29.7 | 26.88 | 29.59 | 10.1 | 29.44 | 9.5 |
| 55.5 | 50.51 | 55.32 | 9.5 | 55.09 | 9.1 |
| 112.2 | 106.10 | 111.95 | 5.5 | 11 .67 | 5.3 |
| 170.0 | 166.19 | 169.36 | 1.9 | 169.57 | 2.0 |

the first natural frequency being 30% higher than the original uncorrected models. The second and third natural frequencies were about 10% higher than those of the uncorrected model. The final corrected natural frequencies for both corrections were almost identical to those measured, indicating a successful correction of the original finite element model.

## 6.4 Conclusions

The Rayleigh's Quotient refinement algorithm has been shown to be a reliable method for modifying a preliminary finite element model so that the calculated dynamic characteristics of the model closely match the real shaft. The method has been successfully applied to beam and torsional element models, and does not require measured mode shape data. With some modes, the resulting equations were ill-conditioned, but this could be avoided by using a different trial model, and selecting different modes as a basis for the correction procedure.

The method was also tested on a step change in beam stiffness, and was able to correct the stiffness of the original model by up to fourteen times the original element stiffness easily, far exceeding the required stiffness corrections envisioned for the procedure.

The Rayleigh's Quotient system identification method was also used to correct the finite element model of a real machine shaft and was able to adjust the element stiffnesses so that the first five eigenvalues of the model were the same as those measured. The test case also showed that the different correction solutions can be achieved by rerunning the model refinement algorithm with different elements selected for adjustment.

One problem this method does not address is the uniqueness of the solution. Because only a limited number of measured eigenvalues are used, the method may make adjustments or corrections to the model that are unexpected or not

unique. That is, for a given set of measured data, there may exist several different corrected models that would predict the desired eigenvalues, and different starting or uncorrected models may lead to different correction solutions. The analyst should compare the calculated mode shapes to the approximate actual mode shapes to see if there are unacceptable differences. Or, a comparison of actual to calculated forced response curves over the frequency range of interest would indicate the validity of the corrected model. It is possible, that a corrected model would give the proper forced response of the dynamic system if the frequency range of interest is covered by the corrected eigenvalues that were input into the algorithm. Although, it is very probable that the model would not give acceptable results for frequencies much outside of that range.

The manufacturer of a particular rotating machine could use this method to provide a corrected finite element model of the machine rotor to the end user. The user would then have an accurate finite element model to use in future balancing, and vibration analysis of the rotor. The correction factors for the rotor model would be done on the basis of measured eigenvalues of the rotor, with the rotor being suspended in the free-free or simply-supported state.

The refinement method does however, require that the finite element analyst performing the procedure have some knowledge of which elements require correction. That is, the analyst must predetermine the most likely areas of error in the model. Some clues as to the correction areas may be found by examining the mode shapes for eigenvalues to be corrected. The areas of the mode shape that exhibit the greatest change in slope of the neutral axis would certainly be the most sensitive to small changes in element stiffness. If incomplete measured mode shape data is available, then algorithms do exist to locate the areas of error in the stiffness matrix. See, for example, Sidhu and Ewins [39] for a method that localizes the error using reduced stiffness matrices from mode shape data over the frequencies of interest.

This method can be used to refine a system model by correcting components first.

That is, the model could be refined by experimentally measuring the eigenvalues of the rotor system components separately and correcting the corresponding component models. Then with the system physically assembled the eigenvalues would be experimentally measured, and then used to correct the mathematical overall model coupling stiffnesses to give a corrected global finite element model.

# CHAPTER 7

# Conclusions

*All's Well That Ends Well — Shakespeare*

This thesis has presented three specific methods for improving the modelling of machinery rotor dynamics, using the finite element technique. First, an isoparametric axisymmetric shaft element based on three-dimensional elasticity, rather than one-dimensional beam theory was developed. Second, a matrix condensation procedure for forced analysis and calculation of natural frequencies of a shaft system needing only a small amount of computer memory was presented. And third, a model refinement method based on Rayleigh's Quotient using the measured free-free eigenvalues was given. The following is a short synopsis of each of the chapters of the thesis.

In the second chapter background into the beam elements normally used to model turbomachinery shafts was given. Additionally, a brief description of numerical difficulties that may be encountered when modelling shafts with gyroscopic effects, and one solution were presented

The third chapter presented an extension of an element for the modelling of shaft dynamics from a subparametr. ∙ ∙ an isoparametric formulation. This axisymmetric element was based on three di ... isional elasticity theory, and was therefore not restricted by the assumptions of simple beam theory. For example, the element

allows the perpendicular cross-sections of a shaft to warp at abrupt changes in section when loaded in bending. Unfortunately, the added accuracy of this element comes at the expense of element matrix size and computational time. The element should be used for shaft sections that have a wide variety of section diameters. This element may also provide some advantage in modelling the effects of shrunk on wheels, where the interference fit has some physical stiffening effect on the shaft. The application of this element for the modelling of an interference fit wheel on a shaft is a suitable area of future research.

An overview of present techniques for modelling the behaviour of journal bearings was also presented. The linear stiffness and damping models for journal bearings are of use only for small perturbation from the journal equilibrium position. However, unbalance, hydrodynamic and aerodynamic forces can often cause large motions of the shaft journal inside the bearing. As a result, accurate dynamic analyses of rotor-bearing systems are difficult. Suitable models based on large perturbations of the journal should be explored. This will most probably require the use of non-linear models and solution techniques, and may also require the introduction of the mathematics of chaos into rotor dynamics.

Chapter 5 gave the continuous coordinate condensation technique for calculating the forced response of a shaft system. The method allows the assembly of a global finite element model which retains the number of degrees of freedom of a single element matrix. This allows the use of very little computer memory, and essentially combines the memory advantages of the transfer matrix method with the accuracy at higher frequencies of the finite element method. Coordinate condensation can be used to great advantage for sections of structure that are modelled with a number of elements of like size and material properties. Two similar elements can be condensed to form a superelement. Two of the superelements can then be used to form a new superelement having the accuracy of four elements, but the same matrix size as a single element. Applied recursively, each condensation step can then double the

effective number of equal size elements in that section of the model. This method has had some use in the area of finite element modelling of acoustics, and the results presented clearly indicate the suitability and ease of use for the modelling of rotor dynamics as well.

Chapter 6 introduced an entirely new system identification procedure that allows moderate adjustment of individual element stiffnesses on the basis of correlating certain calculated and measured eigenvalues of a shaft. The method uses Rayleigh's Quotient to calculate the correction factors, with linear regression and singular value decomposition being applied for solution of the linear systems of equations. A major advantage of this method is that only the first few measured eigenvalues of the actual shaft are needed. The difficulty of measuring accurate mode shapes is thereby avoided. The successful application of a correction to the model of a real machine was presented. Further work needs to be done on automating a procedure for the selection of elements for correction. Also, the modification of the Rayleigh's Quotient system identification method for the correction or creation of the bearing stiffness and damping matrices should be also be examined.

It is hoped that the methods and discussion presented by this work will be of some value for future analysis of rotor dynamics and perhaps for the dynamics of structures in general. Listings of computer programs used will be published as a department report.

# References

[1] William Shakespeare. *The Complete Works of William Shakespeare*. Chatham River Press, New York, 1987.

[2] N. Sanderson and R. Kitching. Flexibility of Shafts with Abrupt Changes of Section. *Int. J. mech. Sci.*, 20:189–199, 1978.

[3] J.S. Archer. Consistent Mass Matrix for Distributed Mass Systems. *Journal of the Structural Division, Proc. of the ASCE*, 89:161–178, Aug. 1963.

[4] J. W. Strutt, Baron Rayleigh. *The Theory of Sound*, volume I. Dover Publications, New York, second edition, 1945.

[5] S. Timoshenko. *Vibration Problems in Engineering*. D. Van Nostrand, Princeton, New Jersey, third edition, Jan. 1965.

[6] R.A. Anderson. Flexural Vibrations in Uniform Beams According to the Timoshenko Theory. *Journal of Applied Mechanics*, pages 504–510, Dec. 1953.

[7] T.C. Huang. The Effect of Rotatory Inertia and of Shear Deformation on the Frequency and Normal Mode Equations of Uniform Beams With Simple End Conditions. *Journal of Applied Mechanics, Trans. of the ASME*, pages 579–584, Dec. 1961.

[8] G.R. Cowper. The Shear Coefficient in Timoshenko's Beam Theory. *Journal of Applied Mechanics, Trans. of the ASME*, 33:335–340, Jun. 1966.

[9] J.S. Archer. Consistent Matrix Formulations for Structural Analysis Using Finite Element Techniques. *American Institute of Aeronautics and Astronautics Journal*, 3(10):1910-1918, Oct. 1965.

[10] D.L. Thomas, J.M. Wilson, and R.R. Wilson. Timoshenko Beam Finite Elements. *Journal of Sound and Vibration*, 31(3):315-330, 1973.

[11] R. Davis, R.D. Henshell, and G.B. Warburton. A Timoshenko Beam Element. *Journal of Sound and Vibration*, 22(4):475-487, 1972.

[12] K.K. Kapur. Vibrations of a Timoshenko Beam, Using Finite Element Approach. *The Journal of the Acoustical Society of America*, 40(5):1058-1063, 1966.

[13] H.D. Nelson. A Finite Rotating Shaft Element Using Timoshenko Beam Theory. *Journal of Mechanical Design, Trans. ASME*, 102:793-803, Oct. 1980.

[14] Leonard Meirovitch. *Computational methods in structural dynamics*. Sijthoff & Noordhoff, Alphen aan den Rijn, The Netherlands, 1980.

[15] M. Geradin and N. Kill. A New Approach to Finite Element Modelling of Flexible Rotors. *Eng. Comput.*, 1:52-64, Mar. 1984.

[16] R.W. Stephenson, K.E. Rouch, and R. Arora. Modelling of Rotors with Axisymmetric Solid Harmonic Elements. *Journal of Sound and Vibration*, 131(3):431-443, 1989.

[17] W.F. Eckert and A. Craggs. The Use of Finite Elements in Rotordynamics Analysis. In *Eleventh Machinery Dynamics Seminar*, pages 48-55, Toronto, Oct. 1990. National Research Council Canada - Machinery Dynamics Subcommittee.

[18] O.C. Zienkiewicz. *The Finite Element Method in Engineering Science*. McGraw-Hill, London, 1971.

[19] H.D. Nelson and J.M. McVaugh. The Dynamics of Rotor-Bearing Systems Using Finite Elements. *Journal of Engineering for Industry, Trans. ASME*, pages 593–600, May 1976.

[20] Ted Belytschko. Finite Elements for Axisymmetric Solids Under Arbitrary Loadings With Nodes on Origin. *American Institute of Aeronautics and Astronautics Journal*, 10(11):1532–1533, Nov. 1972.

[21] R.W. Stephenson and K.E. Rouch. Modelling Rotating Shafts Using Axisymmetric Solid Finite Elements with Matrix Reduction. In *Rotating Machinery Dynamics. DE-Vol.18-1*, pages 141–148, Montreal, Sept. 1989. ASME Design Technical Conferences-12th Biennial Conference on Mechanical Vibration and Noise.

[22] D.M. Smith. *Journal Bearings in Turbomachinery*. Chapman and Hall Ltd., London, 1969.

[23] Tsuneo Someya, editor. *Journal-Bearing Databook*. Springer, Berlin, 1989.

[24] Shaker Research Corporation/Mechanical Technology Incorporated, Latham, New York. *ROTATING MACHINERY: Vibration Analysis and Diagnostic Techniques*, Jun. 1986. Seminar course notes.

[25] A.G. Taylor and A. Craggs. A Review of Fluid Effect Modelling in Rotor Dynamics. In *Eleventh Machinery Dynamics Seminar*, pages 64–95, Toronto, Oct. 1990. National Research Council Canada - Machinery Dynamics Subcommittee.

[26] M.A. Prohl. A General Method for Calculating Critical Speeds of Flexible Rotors. *Journal of Applied Mechanics*, pages A-142–A-148, Sept. 1945.

[27] A. Craggs. The Application of the Transfer Matrix and Matrix Condensation Methods with Finite Elements to Duct Acoustics. *Journal of Sound and Vibration*, 132(2):393–402, 1989.

[28] P.S. Christianson and S. Krenk. A Recursive Finite Element Techinque for Acoustic Fields in Pipes with Absorption. *Journal of Sound and Vibration*, 122(1):107–118, 1988.

[29] W.F. Eckert and A. Craggs. A Method of Continuous Coordinate Condensation. In *Proceedings of the Thirteenth Canadian Congress of Applied Mechanics*, pages 244–245, Winnipeg, Jun. 1991.

[30] A. Craggs and W.F. Eckert. A Reduction Procedure for Finite Element Models of Beams and Shafts. *Journal of Sound and Vibration*. 1993. To be published.

[31] G.M.L. Gladwell. Inverse Problems in Vibration. *Appl Mech Rev*, 39(7):1013–1018, Jul. 1986.

[32] K.A. Stetson and G.E. Palma. Inversion of First-Order Perturbation Theory and Its Application to Structural Design. *American Institute of Aeronautics and Astronautics Journal*, 14(4):454–460, Apr. 1976.

[33] G.B. Thomas and P. Littlewood. A Technique for Modelling Rotors from Measured Vibration Characteristics. *I Mech E*, pages 445–451, 1980.

[34] T.A. Vest and M.S. Darlow. The Use of Beam-Like Modal Data for Stiffness Profile Estimation By the EBS Method — Part I: Justification and Implementation. In *Rotating Machinery Dynamics, DE-Vol.18-1*, pages 51–56, Montreal, Sept. 1989. ASME Design Technical Conferences-12th Biennial Conference on Mechanical Vibration and Noise.

[35] W.F. Eckert and A. Craggs. A Method of Model Refinement for Beams and Shafts Using Rayleigh's Quotient. In *Tenth Machinery Dynamics Seminar*, pages 195–211, Calgary, Sept. 1988. National Research Council Canada - Machinery Dynamics Subcommittee.

[36] W.F. Eckert and A. Craggs. A Method of Model Refinement for Beams and Shafts Using Rayleigh's Quotient. In *Proceedings of the Twelfth Canadian Congress of Applied Mechanics*, pages 434–435, Ottawa, May 1989.

[37] W.H. Press, B.P. Flannery, S.A. Teukolsky, and W.T. Vetterling. *Numerical Recipes The Art of Scientific Computing*. Cambridge University Press, Cambridge, 1986.

[38] William I. Robertson. Finite Element Vibration Analysis of a Model Turbine Rotor. Master's thesis, University of Alberta, spring 1986. Department of Mechanical Engineering.

[39] J. Sidhu and D.J. Ewins. Correlation of Finite Element and Modal Test Studies of a Practical Structure. In *Proc. of the 2nd International Modal Analysis Conference*, pages 756–762, Orlando, Feb. 1984.

# APPENDIX A

# Derivations

*Double, double toil and trouble;*

*Fire, burn; and, cauldron, bubble. — Shakespeare*

## A.1  Timoshenko Differential Equation For Beams

The strain energy, $U$, kinetic energy, $T$, and the external work, $W_{ext}$, of a beam element undergoing flexural vibration, as shown in Fig. A.1, are:

$$U = \frac{1}{2} \int_0^\ell EI \, w_b''(x,t)^2 \, dx + + \frac{1}{2} \int_0^\ell KGA_x \, \psi(x,t)^2 \, dx$$

$$T = \frac{1}{2} \int_0^\ell \rho A_x \, \dot{u}^2(x,t) \, dx + \frac{1}{2} \int_0^\ell \rho I \, \dot{\theta}^2(x,t) \, dx \tag{A.1}$$

$$W_{ext} = \int_0^\ell q(x,t) w(x,t) \, dx.$$

where $E$ is the modulus of elasticity, $I$ is the second moment of area, $K$ is the shear correction coefficient, $G$ is the modulus of rigidity, and $A_x$ is the cross-sectional area of the element.

Hamilton's Principle is written as (with the variation taken inside the integral):

$$\int_{t_1}^{t_2} (\delta W_{ext} + \delta T - \delta U) \, dt = 0. \tag{A.2}$$

163
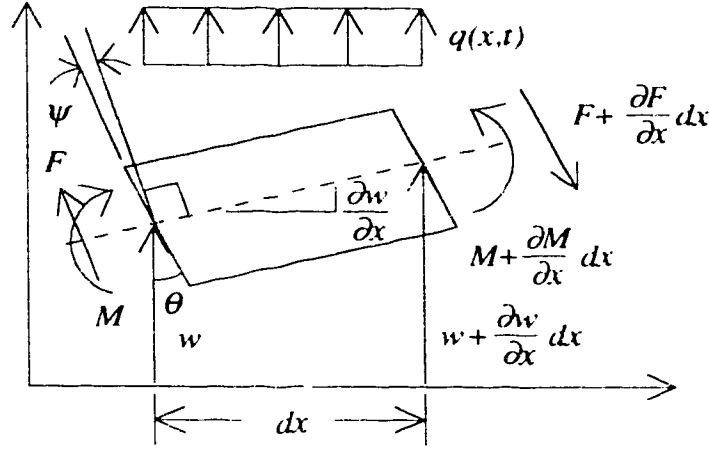
**FIGURE A.1**: Moments and Forces on an Infinitesimal Element

The first variation of the energies is found by varying the displacements by an arbitrary infinitesimal amount, for example $w + \delta w$. The difference between the varied energy expression and the normal expression is the variation of that energy (variations squared are considered negligible). The variations of Eq. (A.1) are given by:

$$\delta U = \int_0^l EI \, w_b'' \, \delta w_b'' \, dx + \int_0^l KGA_r \, \psi \, \delta \psi \, dx$$

$$\delta T = \int_0^l \rho A_r \, \ddot{w} \, \delta \dot{w} \, dx + \int_0^l \rho I \, \dot{\theta} \, \delta \dot{\theta} \tag{A.3}$$

$$\delta W_{ext} = \int_0^l q \, \delta w \, dx.$$

Substituting Eq. (A.3) into Eq. (A.2) gives:

$$\int_{t_1}^{t_2} \int_0^l (q \, \delta w + \rho A_r \, \ddot{w} \, \delta \dot{w} + \rho I \, \dot{\theta} \, \delta \dot{\theta} - EI \, w_b'' \, \delta w_b'' - KGA_r \, \psi \, \delta \psi) \, dx \, dt = 0. \tag{A.4}$$

Rewriting Eq. (A.4) by substituting $\theta = w_b'$ and $\psi = w_b' - w'$ results in:

$$\int_{t_1}^{t_2} \int_0^\ell (q\,\delta w + \rho A_r\, \ddot{w}\,\delta \ddot{w} + \rho I\, \dot{w_b}'\,\delta \dot{w_b}' - EI\, w_b''\,\delta w_b''$$

$$-KGA_r\,(w_b' - w')\,(\delta w_b' - \delta w'))\,dx\,dt = 0.$$

(A.5)

The function being integrated in Eq. (A.5) is an explicit function of $w$ and $w_b'$, and their time and spatial derivatives only. Integrating the $\delta \ddot{w}$ and $\delta \dot{w_b}'$ terms by parts with respect to time, and letting $\delta w = \delta w_b' = 0$ at $t = t_1$ and $t = t_2$ results in:

$$\int_{t_1}^{t_2} \int_0^\ell (q\,\delta w - \rho A_r\, \ddot{w}\,\delta w - \rho I\, \ddot{w_b}'\,\delta w_b' - EI\, w_b''\,\delta w_b''$$

$$-KGA_r\,(w_b' - w')\,(\delta w_b' - \delta w'))\,dx\,dt = 0.$$

(A.6)

Now integrating the $\delta w_b''$ terms w.r.t. $x$, and letting $\delta w_b' = 0$ at $x = 0$ and $x = \ell$ gives:

$$\int_{t_1}^{t_2} \int_0^\ell (q\,\delta w - \rho A_r\, \ddot{w}\,\delta w - \rho I\, \ddot{w_b}'\,\delta w_b' + EI\, w_b'''\,\delta w_b'$$

$$-KGA_r\,(w_b' - w')\,(\delta w_b' - \delta w'))\,dx\,dt = 0.$$

(A.7)

Integrating $\delta w'$ terms w.r.t. $x$, and letting $\delta w = 0$ at $x = 0$ and $x = \ell$ results in:

$$\int_{t_1}^{t_2} \int_0^\ell (q\,\delta w - \rho A_r\, \ddot{w}\,\delta w - \rho I\, \ddot{w_b}'\,\delta w_b' + EI\, w_b'''\,\delta w_b'$$

$$-KGA_r\,(w_b' - w')\,\delta w_b' - KGA_r\,(w_b'' - w'')\,\delta w)\,dx\,dt = 0.$$

(A.8)

The fundamental lemma of the calculus of variations states that where $\int_{x_1}^{x_2} \eta(x)\,G(x)\,dx = 0$, and $G(x)$ is a continuous function over the interval $x_1 \leq x \leq \ldots$ and $\eta(\cdot)$ is an arbitrary continuously differentiable function over the

same interval with $\eta(x_1) = \eta(x_2) = 0$, then $G(x) = 0$ over the interval. Rearranging Eq. (A.8) to group $\delta w_b'$ and $\delta w$ terms and remembering that these virtual displacements are arbitrary and independent, the fundamental lemma can be used to show that:

$$EI\frac{\partial^3 w_b}{\partial x^3} - \rho I\frac{\partial^3 w_b}{\partial x \partial t^2} - KGA_r\left(\frac{\partial w_b}{\partial x} - \frac{\partial w}{\partial x}\right) = 0 \tag{A.9}$$

$$q - \rho A_r\frac{\partial^2 \cdots}{\partial t^2} \qquad\qquad \frac{\partial^2 w_b}{\partial x^2} - \frac{\partial^2 w}{\partial x^2}) = 0. \tag{A.10}$$

Differentiating Eq. (A.9) with respect to $x$, and rearranging gives:

$$KGA_r\left(\frac{\partial^2 w_b}{\partial x^2} - \frac{\partial^2 w}{\partial x^2}\right) = EI\frac{\partial^4 w_b}{\partial x^4} - \rho I\frac{\partial^4 w_b}{\partial x^2 \partial t^2} \tag{A.11}$$

$$q = \rho A\frac{\partial^2 w}{\partial t^2} + KGA\left(\frac{\partial^2 w_b}{\partial x^2} - \frac{\partial^2 w}{\partial x^2}\right). \tag{A.12}$$

Substitute Eq. (A.11) into Eq. (A.12) to give:

$$q(x,t) = \rho A\frac{\partial^2 w}{\partial t^2} + EI\frac{\partial^4 w_b}{\partial x^4} - \rho I\frac{\partial^4 w_b}{\partial x^2 \partial t^2}. \tag{A.13}$$

Consider Eq. (A.12) under free vibration (i.e., $q = 0$), and rearranging gives:

$$\left(\frac{\partial^2 w_b}{\partial x^2} - \frac{\partial^2 w}{\partial x^2}\right) = -\frac{\rho}{KG}\frac{\partial^2 w}{\partial t^2}. \tag{A.14}$$

Rearranging Eq. (A.14) and differentiate with respect to $x$ twice:

$$\frac{\partial^4 w_b}{\partial x^4} = \frac{\partial^4 w}{\partial x^4} - \frac{\rho}{KG}\frac{\partial^4 w}{\partial x^2 \partial t^2}. \tag{A.15}$$

And differentiating Eq. (A.14) with respect to time twice:

$$\frac{\partial^4 w_b}{\partial x^2 \partial t^2} = \frac{\partial^4 w}{\partial x^2 \partial t^2} - \frac{\rho}{KG}\frac{\partial^4 w}{\partial t^4}.$$  (A.16)

Substituting Eq. (A.15) and Eq. (A.16) into Eq. (A.13) (where $q(x,t) = 0$) gives the Timoshenko governing partial differential equation for a beam undergoing lateral vibration:

$$\rho A_x \frac{\partial^2 w}{\partial t^2} + EI\frac{\partial^4 w}{\partial x^4} - \rho I \frac{\partial^4 w}{\partial x^2 \partial t^2} - \frac{\rho EI}{KG}\frac{\partial^4 w}{\partial x^2 \partial t^2} + \frac{\rho^2 I}{KG}\frac{\partial^4 w}{\partial t^4} = 0.$$  (A.17)

The first term of the left hand side of Eq. (A.17) is due to the inertia of the element, the second term is the restoring or elastic force; and these two terms together give the Euler-Bernoulli equation. The third term is the contribution of the rotatory inertia due to the bending of the element, and the fourth term is the rotatory inertia due to shear deformation of the element. The fifth and final term is a mixed term which is small and is usually considered negligible.

## A.2  Beam Equations

The forces and moments acting on an infinitesimal element are as shown in Fig. A.1. The element considered is under static equilibrium, and has a constant shear force and slope such that $q(x) = 0$. The shear stress-strain relationship is:

$$\frac{F}{A_x} = GK\psi$$  (A.18)

Summing the forces on the element:

$$F - (F + \frac{dF}{dx}dx) = \frac{dF}{dx} = 0$$  (A.19)

Summing the moments on the element:

$$M - (M + \frac{dM}{dx}dx) + (F + \frac{dF}{dx}dx)dx = 0$$

$$\Rightarrow \qquad -\frac{dM}{dx} + Fdx + \frac{dF}{dx}dx^2 = 0 \qquad (A.20)$$

$$\Rightarrow \qquad \frac{dM}{dx} = F.$$

Integrating Eq. (A.19):

$$F = \alpha_1 = GKA_r\psi$$
$$(A.21)$$
$$\Rightarrow \qquad \psi = \frac{\alpha_1}{GKA_r}.$$

Integrating Eq. (A.20):

$$\frac{dM}{dx} = \alpha_1$$
$$(A.22)$$
$$\Rightarrow \quad M = \alpha_1 x + \alpha_2.$$

The moment curvature relationship is:

$$\frac{d^2 w_b}{dx^2} = \frac{d^2 w}{dx^2} + \frac{d\psi}{dx} = \frac{M}{EI}. \qquad (A.23)$$

Combining Eq. (A.22) and Eq. (A.23) (but $\frac{d\psi}{dx} = 0$) and integrating gives:

$$w(x) = \frac{1}{EI}(\alpha_1\frac{x^3}{6} + \alpha_2\frac{x^2}{2} + \alpha_3 x + \alpha_4). \qquad (A.?)$$
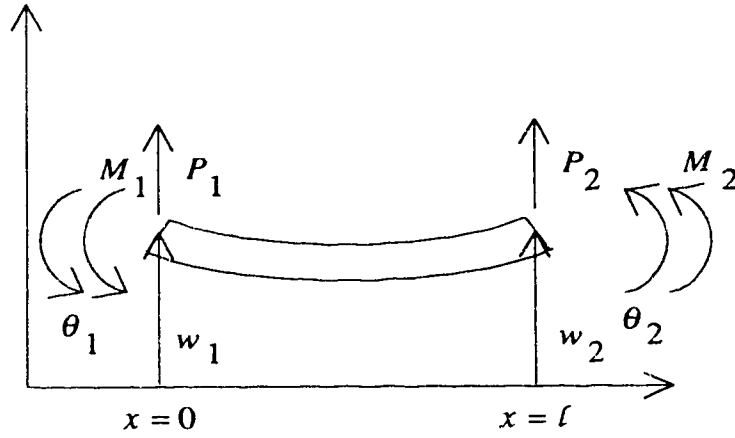
**FIGURE A.2**: Beam Eleme...

And the bending angle is the sum of the derivative of Eq. (A.24) and the shear slope, Eq. (A.21):

$$\theta(x) = \frac{1}{EI}(\alpha_1\frac{x^2}{2} + \alpha_2 x + \alpha_3 + \alpha_1\frac{EI}{GKA_x}). \tag{A.25}$$

Rewriting Eq. (A.25), where $\beta = \frac{EI}{GKA_x}$:

$$\theta(x) = \frac{1}{EI}(\alpha_1(\frac{x^2}{2} + \beta) + \alpha_2 x + \alpha_3). \tag{A.26}$$

Equating the displacement equations Eq. (A.24) and Eq. (A.26) with the element nodal unknowns at $x = 0$ and $x = \ell$ as shown in Fig. A.2 gives the following matrix equation:

$$\begin{Bmatrix} w_1 \\ \theta_1 \\ w_2 \\ \theta_2 \end{Bmatrix} = \frac{1}{EI}\begin{bmatrix} 0 & 0 & 0 & 1 \\ \beta & 0 & 1 & 0 \\ \frac{\ell^3}{6} & \frac{\ell^2}{2} & \ell & 1 \\ (\frac{\ell^2}{2} + \beta) & \ell & 1 & 0 \end{bmatrix}\begin{Bmatrix} \alpha_1 \\ \alpha_2 \\ \alpha_3 \\ \alpha_4 \end{Bmatrix}. \tag{A.27}$$

Solving Eq. (A.27) for the unknown alpha coefficient vector results in:

$$\{\alpha\} = [T]\{w_e\},$$ 

(A.28)

where:

$$[T] = \frac{EI}{\ell(\ell^2 + 12\beta)} \begin{bmatrix} 12 & 6\ell & -12 & 6\ell \\ -6\ell & (-4\ell^2 - 12\beta) & 6\ell & (-2\ell^2 + 12\beta) \\ -12\beta & (\ell^3 + 6\beta\ell) & 12\beta & -6\beta\ell \\ \ell(\ell^2 + 12\beta) & 0 & 0 & 0 \end{bmatrix}.$$ 

(A.29)

Combining Eq. (A.28), Eq. (A.29) into the displacement approximate equations gives:

$$
\begin{aligned}
w(x,t) &= \{B_o\}^T [T] \{w_e(t)\} \\
\psi(x,t) &= \{C\}^T [T] \{w_e(t)\} \\
\theta(x,t) &= \{D\}^T [T] \{w_e(t)\},
\end{aligned}
$$ 

(A.30)

where:

$$
\begin{aligned}
\{B_o\}^T &= \frac{1}{EI} \lfloor \quad \frac{x^3}{6} \quad \frac{x^2}{2} \quad x \quad 1 \quad \rfloor \\
\{C\}^T &= \frac{1}{EI} \lfloor \quad \beta \quad 0 \quad 0 \quad 0 \quad \rfloor \\
\{D\}^T &= \frac{1}{EI} \lfloor \quad \frac{x^2}{2} + \beta \quad x \quad 1 \quad 0 \quad \rfloor.
\end{aligned}
$$ 

(A.31)

# A.3 Hamilton's Principle In Matrix Form

Substituting Eq. (A.30) into Eq. (A.4) gives:

$$
\int_{t_1}^{t_2} \int_0^\ell \Big( \{\delta w_e\}^T [T]^T \{B_o\} q + \rho A \{\delta \ddot{w}_e\}^T [T]^T \{B_o\} \{B_o\}^T [T] \{\ddot{w}_e\}
$$
$$
+ \rho I \{\delta \ddot{w}_e\}^T [T]^T \{D\} \{D\}^T [T] \{\ddot{w}_e\}
$$
$$
- EI \{\delta w_e\}^T [T]^T \{B_o''\} \{B_o''\}^T [T] \{w_e\}
$$
$$
- KGA \{\delta w_e\}^T [T]^T \{C\} \{C\}^T [T] \{w_e\} \Big) \, dx \, dt = 0.
$$

(A.32)

Integrate $\{\delta \ddot{w}_e\}^T$ terms w.r.t. time, and letting $\{\delta w_e\}^T = \{0\}^T$ at $t = t_1$ and $t = t_2$ gives:

$$
\int_{t_1}^{t_2} \int_0^\ell \{\delta w_e\}^T [T]^T \Big( \{B_o\} q + (-\rho A \{B_o\} \{B_o\}^T - \rho I \{D\} \{D\}^T)[T] \{\ddot{w}_e\}
$$
$$
+ (-EI \{B_o''\} \{B_o''\}^T - KGA \{C\} \{C\}^T)[T] \{w_e\} \Big) \, dx \, dt = 0.
$$

(A.33)

Define:

$$
\{Q\} = \int_0^\ell q [T]^T \{B_o\} \, dx
$$

$$
[M_e] = \int_0^\ell (\rho A [T]^T \{B_o\} \{B_o\}^T [T] + \rho I [T]^T \{D\} \{D\}^T [T]) \, dx
$$

(A.34)

$$
[K_e] = \int_0^\ell (EI [T]^T \{B_o''\} \{B_o''\}^T [T] + KGA [T]^T \{C\} \{C\}^T [T]) \, dx.
$$

Then Eq. (A.33) becomes:

$$
\int_{t_1}^{t_2} \{\delta w_e\}^T (\{Q\} - [M_e] \{\ddot{w}_e\} - [K_e] \{w_e\}) \, dt = 0.
$$

(A.35)

Since $\{\delta w_e\}^T$ is arbitrary, the fundamental lemma of variational calculus states that the portion of Eq. (A.35) in parentheses must be equal to zero. That is:

$$[M_e]\{\ddot{w}_e\} + [K_e]\{w_e\} = \{Q\}.\qquad\text{(A.36)}$$

## A.4  Serendipity Functions

The serendipity functions are formed by using the simple polynomials. A general displacement $q$ anywhere in the element can be defined as the following polynomial equation:
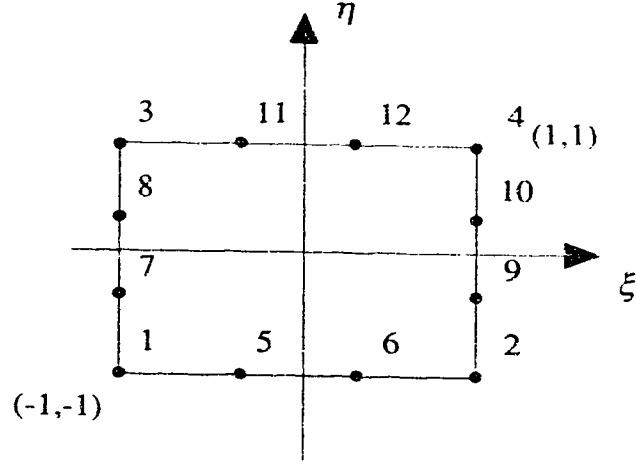
$$q = q_1 + q_2\xi + q_3\eta + \ldots + q_{11}\xi^3\eta + q_{12}\xi\eta^3 = \lfloor P\rfloor\{q_a\},\qquad\text{(A.37)}$$

where $\{q_a\}$ is the vector of the coefficients, and the simple polynomials are:

$$\lfloor P\rfloor = \lfloor\, 1 \quad \xi \quad \eta \quad \xi\eta \quad \xi^2 \quad \eta^2 \quad \xi^2\eta \quad \xi\eta^2 \quad \xi^3 \quad \eta^3 \quad \xi^3\eta \quad \xi\eta^3 \,\rfloor.\qquad\text{(A.38)}$$

The vector of the nodal displacements, $\{q_e\}$, is defined by evaluating Eq. (A.37) at the nodal locations shown in Fig. A.3. The matrix $[T]$, is 12 by 12.

$$\{q_e\} = \begin{bmatrix} \lfloor P(\xi_1, \eta_1)\rfloor \\ \lfloor P(\xi_2, \eta_2)\rfloor \\ \vdots \\ \lfloor P(\xi_{11}, \eta_{11})\rfloor \\ \lfloor P(\xi_{12}, \eta_{12})\rfloor \end{bmatrix} \{q_a\} = [T]\{q_a\}\qquad\text{(A.39)}$$

**FIGURE A.3**: Nodal Positions

Solve Eq. (A.39) for the vector of coefficients, $\{q_a\}$, and substitute back into Eq. (A.37) to give:

$$q = \lfloor P \rfloor [T^{-1}] \{q_r\} .$$

(A.40)

The serendipity functions are now given by:

$$\lfloor N \rfloor = \lfloor P \rfloor [T^{-1}].$$

(A.41)

The serendipity functions have been calculated explicitly and included in the element algorithm, thereby avoiding the need for a matrix inversion operation for every element formed.

Table A.1 gives the values of $\xi$ and $\eta$ at each node.

**TABLE A.1**: Local Variable Values

| Node | $\xi$ | $\eta$ |
|------|-------|--------|
| 1 | -1 | -1 |
| 2 | 1 | -1 |
| 3 | -1 | 1 |
| 4 | 1 | 1 |
| 5 | -1/3 | -1 |
| 6 | 1/3 | -1 |
| 7 | -1 | -1/3 |
| 8 | -1 | 1/3 |
| 9 | 1 | -1/3 |
| 10 | 1 | 1/3 |
| 11 | -1/3 | 1 |
| 12 | 1/3 | 1 |

The inverse of matrix $[T]$ is:

$$\frac{1}{32}\begin{bmatrix}
-1.0 & -1.0 & -1.0 & -1.0 & 0.9 & 0.9 & 0.9 & 0.9 & 0.9 & 0.9 & 0.9 & 0.9 \\
1.0 & -1.0 & 1.0 & -1.0 & -2.7 & 2.7 & -0.9 & -0.9 & 0.9 & 0.9 & -2.7 & 2.7 \\
1.0 & 1.0 & -1.0 & -1.0 & -0.9 & -0.9 & -2.7 & 2.7 & -2.7 & 2.7 & 0.9 & 0.9 \\
-1.0 & 1.0 & 1.0 & -1.0 & 2.7 & -2.7 & 2.7 & -2.7 & -2.7 & 2.7 & -2.7 & 2.7 \\
0.9 & 0.9 & 0.9 & 0.9 & -0.9 & -0.9 & 0.0 & 0.0 & 0.0 & 0.0 & -0.9 & -0.9 \\
0.9 & 0.9 & 0.9 & 0.9 & 0.0 & 0.0 & -0.9 & -0.9 & -0.9 & -0.9 & 0.0 & 0.0 \\
-0.9 & -0.9 & 0.9 & 0.9 & 0.9 & 0.9 & 0.0 & 0.0 & 0.0 & 0.0 & -0.9 & -0.9 \\
-0.9 & 0.9 & -0.9 & 0.9 & 0.0 & 0.0 & 0.9 & 0.9 & -0.9 & -0.9 & 0.0 & 0.0 \\
-0.9 & 0.9 & -0.9 & 0.9 & 2.7 & -2.7 & 0.0 & 0.0 & 0.0 & 0.0 & 2.7 & -2.7 \\
-0.9 & -0.9 & 0.9 & 0.9 & 0.0 & 0.0 & 2.7 & -2.7 & 2.7 & -2.7 & 0.0 & 0.0 \\
0.9 & -0.9 & -0.9 & 0.9 & -2.7 & 2.7 & 0.0 & 0.0 & 0.0 & 0.0 & 2.7 & -2.7 \\
0.9 & -0.9 & -0.9 & 0.9 & 0.0 & 0.0 & -2.7 & 2.7 & 2.7 & -2.7 & 0.0 & 0.0
\end{bmatrix} \quad (\text{A.42})$$